MAKING BETTER USE OF LIGHT: ADDRESSING OPTICAL CHALLENGES WITH METASURFACES

by

Di Wang

A Dissertation

Submitted to the Faculty of Purdue University

In Partial Fulfillment of the Requirements for the degree of

Doctor of Philosophy

School of Electrical & Computer Engineering

West Lafayette, Indiana

December 2019

THE PURDUE UNIVERSITY GRADUATE SCHOOL

STATEMENT OF COMMITTEE APPROVAL

Dr. Vladimir M. Shalaev, co-chair

Department of Electrical & Computer Engineering

Dr. Alexandra Boltasseva, co-chair

Department of Electrical & Computer Engineering

Dr. Alexander V. Kildishev

Department of Electrical & Computer Engineering

Dr. Zhihong Chen

Department of Electrical & Computer Engineering

Approved by:

Dr. Dimitrios Peroulis

Head of the Graduate Program

To my beautiful wife Xue Wang:

I am so proud of you. Now I have a PhD degree too.

ACKNOWLEDGMENTS

I would like to thank the following people for their guidance and help in my PhD program, without which I could not have reached the level I am at today:

- Dr. John “Jan” Lewis Hall, whose advice and recommendation served as the initial condition of my academic career;
- Prof. Vladimir M. Shalaev, Alexandra Boltasseva and Alexander V. Kildishev, who provided me with luxurious research freedom, paramount support, and insightful instructions;
- Dr. Naresh Kumar Emani, who mentored me through the beginning of my PhD program and tutored me on the fundamentals of graphene plasmonics;
- Dr. Yi Xuan, who always offered timely help in the cleanroom;
- Dr. Alexei Lagoutchev, who supervised all my activities in the optics lab;
- Dr. Mikhail Y. Shalaginov, who introduced me to SPIE Purdue Student Chapter to hone my interpersonal and leadership skills;
- Dr. Justus C. Ndukaife, who exemplified a great student chapter leader for me to follow;
- Dr. Meredith Henstridge and Dr. Carl Pfeiffer, who showed me how to establish healthy collaborative research relationship;
- Dr. Zhaxylyk A. Kudyshev, who gave me valuable advice on numerical simulations and revitalized my passion for (playing) basketball;
- Mr. Andres E. Llacsahuanga Allcca, who tremendously helped to rid my lab work of troubles and corrected my Spanish pronunciations;
- All my colleagues and staff members at Birck Nanotechnology Center, who assisted me in my lab work, student chapter activities, and presentation skills;
- Dr. Xue Wang, who already made my life so enjoyable, and continues to create endless wonderful things to hope for.

TABLE OF CONTENTS

LIST OF TABLES

LIST OF FIGURES

ABBREVIATIONS

IR: infrared
SP: surface plasmon
SPP: surface plasmon polariton
LSPR: localized surface plasmon
RPA: random phase approximation
EOT: extraordinary optical transmission
PD: photodetector
PV: photovoltaic
PTE: photothermoelectric
MGM-PD: metal-graphene-metal photodetector
HC: hot carrier
SLG: single layer graphene
CVD: chemical vapor deposition
PMMA: poly(methyl methacrylate)
GNR: graphene nanoribbon
CNP: charge neutral point
FTIR: Fourier transform infrared
SL-GNR: single layer GNR
DL-GNR: double layer GNR
TL-GNR: triple layer GNR
SEM: scanning electron microscopy/micrograph
FEFD: finite element frequency domain
FEM: finite element method
FDTD: finite-difference time-domain
NSOM: near-field scanning optical microscopy
FET: field effect transistor
EBL: electron beam lithography
STPV: solar thermophotovoltaics
OTI: optical thermoreflectance imaging
TDTR: time-domain thermoreflectance
NV: nitrogen vacancy

TGP: thermographic phosphor
SThM: scanning thermal microscopy
NDA: nanodisk array
CW: continuous wave
LED: light emitting diode
CCD: charge-coupled device
ZB: zettabyte
HDD: hard disc drive
IoT: internet of things
APM: anisotropic plasmonic metasurface
CIE: International Commission on Illumination
LP: linearly-polarized
CCW: counter-clockwise

ABSTRACT

Author: Wang, Di. PhD
Institution: Purdue University
Degree Received: December 2019
Title: Making Better Use of Light: Addressing Optical Challenges with Metasurfaces.
Committee Chair: Vladimir M. Shalaev, Alexandra Boltasseva

The capability of light goes well beyond illumination, yet it is so underused in our lives because the control of light still largely relies on clumsy bulk lenses. Less than 10 years ago, a type of revolutionary devices made of nanometer scale optical elements – metasurfaces – was invented to control the light propagation and its energy dissipation with arbitrary degree of freedom, at unprecedentedly small volumes (although some would argue that the advent of metasurfaces came in the 1990s). Vast diversity of new discoveries has since been made possible, and many more existing applications have seen significant performance enhancement with the aid of metasurfaces.

In the scope of this work, I explore the use of a variety of metasurfaces to address several existing real-world challenges: sensing, optical heating, and data storage. Among these, three metasurfaces involve the world's first two-dimensional material, graphene. I first investigate the graphene plasmonic resonator, which have been shown to be extremely sensitive single-molecule sensors. Graphene also has many intriguing properties in photodetection applications, such as lightweight, ultra-wide detection band, and ultrafast response speed. I have used two different metasurfaces to enhance the intrinsically low responsivity (sensitivity) of graphene photodetectors. Amidst the discussion of graphene photodetectors, I show the characterization result of plasmonic heating of metasurfaces, an essential process of the graphene photo-responsivity enhancement. Lastly, I present a multi-functional metasurface which can be used in optical steganography, encryption, and data storage. The proposed metasurface is compatible with large scale parallel readout, which outperforms current Blu-ray technology in both storage capacity and readout speed.

1. INTRODUCTION

Being the fastest information and energy carrier, light is extensively used in studying and engineering of nanoscale systems such as biochemistry[1]–[3], energy conversion[4]–[6], optical lithography[7], micro- and nano-particle manipulation[8], information processing[9], [10], quantum computing[11]–[14], etc. To date, the control of light is mostly realized via bulky optical lenses, which requires high-precision lens manufacturing, sophisticated lens systems for advanced light manipulation, and sets a lower boundary of the footprint of optical devices. In conventional optical systems, light cannot be used to study/engineer particles that are arbitrarily small, because once the size of the particle becomes comparable to or smaller than the wavelength of light, diffraction becomes significant due to the wave nature of light, and the performance (imaging, sensing , and lithography resolution) usually deteriorates[15]. Plasmonic nanostructures, which support free electron oscillations (known as surface plasmons, SPs) in response to light irradiation, have proven to be promising candidates for light manipulation in the deep subwavelength regime[16], [17]. Surface plasmons exhibit a resonant behavior at a particular wavelength when the electric restoring force in metallic nanoparticles equals the Lorentz force caused by an incident oscillating electric field[18]. Capable of confining electron oscillations to length scales one order of magnitude smaller than wavelength of incident light, plasmonic metasurfaces have been used to probe the presence of single-layer protein molecules which is only 5 nm thick[1].

Graphene, the world's first-ever discovered two-dimensional material, also supports surface plasmons because of its capability to accommodate free electrons. Graphene plasmonics exhibits a number of unique features such as ultra-high field confinement (one order of magnitude higher than the conventional plasmonic metals), dynamic tunability, and long SPP propagation length. In the following, an entire sub-section is dedicated to discuss graphene plasmonics and its applications.

The whole research field of metasurface and metamaterials[19]–[21] (the word "meta", or "μετα", means "beyond" in Greek), which are a group of functionalized surfaces and materials exhibiting artificially engineered optical properties that are unattainable in naturally occurring materials, initially roots from the soil of plasmonics[22], [23]. In general, metasurfaces can be categorized into two types based on their functionalities. The first type is used to create arbitrary

optical wavefront and beam propagation, via nanoscale metallic optical scatters that induce abrupt optical phase discontinuities at desired positions. As such, this type of metasurfaces is mostly designed to replace bulky optical lenses in advanced imaging[24]–[27], holography[28], [29], and beam control systems. The second type of metasurfaces is used to manipulate the energy dissipation of light, by selectively reflecting, transmitting, and absorbing certain portions of the incident light spectrum, and is widely implemented in applications ranging from sensing[30]–[32], energy[4], [33], [34], colors[35]–[37], and even data storage[38], [39].

Aside from plasmonics, graphene also exhibits a number of enticing signatures for photodetection applications, such as lightweight, ultimate thinness, ultra-wide detection band, and ultrafast response speed. However, the one feature that precludes graphene from practical application is its intrinsically low sensitivity, which originates from the low optical absorptance from the single layer of carbon atoms. Plasmonic structures, on the other hand, provide a viable means to augment the performance of graphene photodetectors. At the end of this section, a pedagogical presentation of the mechanism of graphene photodetection is shown, as an introduction to the two graphene photodetector works that will be discussed in more details later.

1.1 Surface plasmons

Surface plasmons (SPs) are coherent delocalized electron oscillations coupled with photons existing at the metal-dielectric interface[40]–[42]. The electric field evanescently decays in the direction perpendicular to the interface thus allows for deep subwavelength confinement of electromagnetic energy. On one hand, surface plasmons can propagate along the interface between materials with negative (metal) and positive (dielectric) permittivities, which are named surface plasmon polaritons (SPPs) as shown in Figure 1.1(a). By solving the Maxwell's equations for the electromagnetic waves at such an interface with proper boundary conditions, the dispersion of SPPs can be described by:

$$\beta = \frac{\omega}{c}\sqrt{\frac{\varepsilon_d \varepsilon_m}{\varepsilon_m + \varepsilon_d}} \tag{1.1}$$

where β is the propagating constant of the traveling wave and corresponds to the component of the wave vector in the direction of propagation, ω is the angular frequency, c is the speed of light in vacuum, ε_d and ε_m are the permittivities of dielectric and metal, respectively. This dispersion

relation indicates that SPPs can propagate with larger wave vectors along the interface than that of light in vacuum, and leads to evanescent decay into both the metal and the dielectric medium. Since wavevector is proportional to the inverse of wavelength, a larger wavevector means shorter propagating wavelength for SPPs at metal-dielectric interface than light in vacuum. Combined with the rapid field decay into surrounding media, this allows large electromagnetic field confinement at the metal-dielectric interface.

On the other hand, surface plasmons can also be found in isolated deep-subwavelength metallic nanoparticles. In this case, light interacts with particles much smaller than the incident light wavelength, which leads to a plasmon oscillating locally around the nanoparticle with a resonant frequency instead of propagating along a certain direction like in the case of SPP. Hence, this type of plasmon oscillation is named localized surface plasmon resonance (LSPR), as shown in Figure 1.1(b). The LSPR is sensitive to changes in the local dielectric environment, as well as the shape and material composition of the hosting metallic nanoparticle[40].

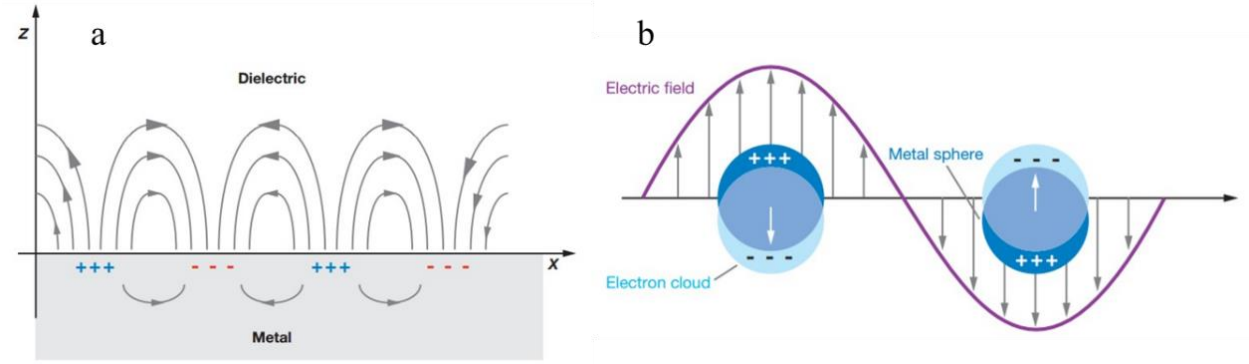

Figure 1.1 Schematic diagrams for surface plasmons

Schematic diagrams illustrating (a) surface plasmon polariton and (b) localized surface plasmon resonance. From [40]. Reprinted with permission from Willets and Van Duyne, Annu. Rev. Phys. Chem. 58 (1), 267–297, 2007. Copyright 2007 Annual Reviews.

1.2 Graphene plasmonics

Conventionally, the research community favors noble metals such as gold and silver as building blocks of plasmonic systems due to their large negative permittivity and relatively low optical loss in the visible frequencies, as well as their chemical inertness[43]. However, these

materials are costly, not suitable for IR plasmonics (due to plasma frequencies being in the visible), and lack dynamic tunability. Therefore, to extend plasmonics into IR frequencies with tunable performance, alternative plasmonic materials are in demand.

Since its successful cleavage from bulk graphite in 2004, graphene—a monolayer of carbon atoms arranged in a two-dimensional hexagonal lattice[44], [45]—has been intensively investigated as a plasmonic material. While the large optical loss, and lack of dynamic tunability and high cost hinder conventional noble metal plasmonics from practical applications[46], [47], the ultrahigh carrier mobility and dynamic tunability in the electrical/optical properties that graphene possesses make it the ideal candidate to overcome these hurdles. The photonic properties of graphene can be represented by its in-plane conductivity as a function of parallel wavevector $k_{\parallel}$ and frequency ω. Within the random phase approximation (RPA), graphene's in-plane conductivity is given by[48]:

$$\sigma(\omega) = \frac{e^2 T}{\pi\hbar}\frac{i}{\omega + i\tau^{-1}}\log[2\cosh(E_F/2k_BT)] + \frac{e^2}{4\hbar}\left[H\left(\frac{\omega}{2}\right) + \frac{4i\omega}{\pi}\int_0^{\infty} \mathrm{d}\varepsilon \frac{H(\varepsilon) - H(\omega/2)}{\omega^2 - 4\varepsilon^2}\right] \tag{1.2}$$

where

$$H(\varepsilon) = \frac{\sinh(\hbar\varepsilon/k_BT)}{\cosh(E_F/k_BT) + \cosh(\hbar\varepsilon/k_BT)}$$

e is the electron charge, $\hbar$ is reduced Planck constant, T is temperature, τ is electron relaxation time, k_B is Boltzmann constant, E_F is Fermi energy determined by dopant type and concentration in graphene. The first term in Equation 1.2 describes a Drude model response for *intraband* transitions, whereas the remaining terms arise from *interband* transitions, which lead to significant optical losses when at photon energies close to and above $2E_F$. Equation 1.2 is the core of both numerical and analytical calculations of graphene optical response. Consequently, the plasmon dispersion in *unpatterned* doped graphene is given by:

$$k_{sp} \approx i(\epsilon + 1)\omega/4\pi\sigma \approx (\hbar^2/4e^2E_F)(\epsilon + 1)\omega(\omega + i/\tau) \tag{1.3}$$

where ϵ is the permittivity of the substrate. Before experimental demonstrations of graphene plasmons were carried out, theoretical calculations by multiple groups based on Equations 1.2 and 1.3 (or their equivalent) suggested that graphene plasmons exhibit two enticing features: ultrahigh optical confinement on the order of several hundred ($\lambda_{air}/\lambda_{plasmon}$~100), and long SPP propagation

lengths (more than 100 SPP wavelengths in the mid-infrared frequencies)[48]–[50]. These two features, together with graphene's dynamic tunability in optical properties, form the basis of the unique graphene plasmon platform with merits unparalleled by conventional noble metal plasmons. However, the substantial difference between free space wavelength and plasmon wavelength imposes great challenge to launch surface plasmons in graphene, which requires sharp tips (with radius of a few tens of nanometers) to excite SPPs[51]–[53], or nano-patterning graphene into metasurfaces to excite localized surface plasmons (LSPs)[54]–[62]. Several early theoretical works on graphene metasurface applications have suggested that LSPs in graphene nanodisks can lead to complete optical absorption in mid-IR in a Salisbury screen configuration[63], and graphene ribbons can be made into electrically modifiable waveguides with longer propagation distances and higher edge field confinement than conventional bulk metallic waveguides[61], etc. Notably, a recent theoretical work pointed out that ultrafast (~200 fs) radiative heat transfer happens in two graphene nanodisks vertically separated by 1 nm via plasmon interaction, owing to the extraordinarily large plasmonic field concentration and low electronic heat capacity in graphene[64]. These theoretical works provided necessary tools to guide later experimental research on graphene metasurfaces.

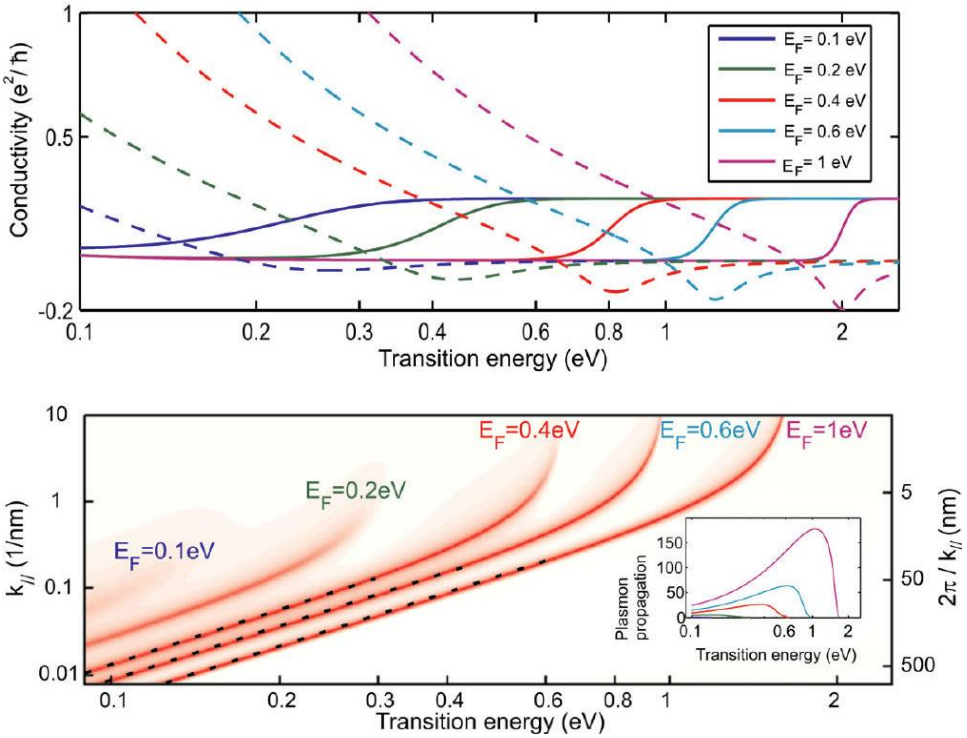

Figure 1.2 Graphene conductivity and plasmon dispersion

Graphene conductivity (top, sold curves: real part, dashed curves: imaginary part) and plasmon dispersion (bottom) at difference Fermi energies. In plasmon dispersion plot, the contour plot shows the Fresnel reflection coefficient $|r_p|$, the dashed lines correspond to the Drude model (Equation 1.3). From [48]. Reprinted with permission from Koppens, Chang, Garcia de Abajo, Nano Lett. 11 (8), 3370-3377, 2011. Copyright 2011 American Chemical Society.

Thanks to the development of nanofabrication technology, graphene metasurfaces with elements small enough to excite graphene plasmons were successfully fabricated, and experimental works[57]–[59] that followed explore in great detail the nature of graphene plasmons. The metasurfaces used include graphene nanoribbons, nanodisks and nanorings. As the theory predicts, optical confinement greater than 100, which is larger than that experimentally obtained with SPP in unpatterned graphene sheet ($\lambda_{air}/\lambda_{plasmon}$~40-60)[52], [53], as well as plasmon resonance tunability of 0.1 eV, has been achieved with LSP in graphene nanoribbons[57]. The damping mechanisms of LSP in graphene nanoribbons via interaction with graphene optical phonon and substrate phonon have also been investigated by several groups, revealing ~20 fs plasmon lifetime at energies above the optical phonon energy (~0.2 eV) of graphene[59]. Quite remarkably, resonance energies up to 335 meV (3.7 um free-space wavelength) has been achieved

in graphene nanorings[58], however, it remains a significant challenge to further push the intrinsic graphene plasmon resonance to near-IR and visible frequencies for telecom and detection applications. In order to accomplish this, nanostructures smaller than 5 nm and doping levels higher than 1 eV are required, and efforts are underway towards this goal. Theoretical calculations were also performed to support experimental results, where graphene was modeled as a material with finite thickness (~0.3 nm)[57], [60]. Both numerical methods and analytical calculation[58], [60], achieved excellent agreement with experiments.

Going on in parallel with investigating intrinsic plasmons in graphene were efforts towards using graphene as a plasmon resonance-tuning material for noble metal metasurfaces[18]. The idea is to make use of the tunable optical properties of graphene to dynamically change the environment dielectric function for the noble metal metasurfaces, therefore actively tune their plasmon resonances. It has been demonstrated that graphene can alter both the resonance linewidths[65] and frequencies[66]–[70] in the mid-IR in back-gated graphene devices. The dynamic tuning range achieved can be as large as 1.1 um with a modulation frequency of 30 MHz[68], and 100% modulation depth was also demonstrated in a tunable metasurface mid-IR perfect absorber[66]. Similar to plasmons in graphene, for graphene to tune plasmon resonances in near-IR and even visible frequencies, gating techniques other than dielectric back gating are required to supply adequate carrier densities. Emani et al demonstrated electrical tunability of Fano resonance with graphene at ~2.4 um with ionic gel top gating[71].

Based upon the developments in the aforementioned graphene plasmon researches, a number of applications utilizing dynamically tunable graphene plasmons with superior performance to conventional plasmonic material platforms have been realized. The following highlights some of the efforts. Biosensing: Rodrigo et al showed that graphene nanoribbons exhibit 6X enhancement in sensitivity compared to gold dipole antennas when used to detect protein monolayers, and that the resonance in graphene nanoribbons can be electrically tuned to sense difference vibrational bands[2]. Photodetection: Noble metal metasurfaces[30], [72]–[75] as well as graphene nanoribbons[76] have been used to enhance the sensitivity of graphene based photodetectors by many research groups, and typically the sensitivity can be enhanced by an order of magnitude, even as high as by 200 times[72]. Lasing: Chakraborty et al showed that graphene can be used to dynamically tune the emission spectrum of quantum cascade lasers when placed on a metallic waveguide with aperiodic slits[77]. Optical absorber/modulator: Jang et al demonstrated

tunable optical absorption (0~25%) with graphene nanoribbons in a Salisbury screen structure[78]; Kim et al experimentally demonstrated 28.6% transmission modulation efficiency by coupling graphene nanoribbons to metallic extraordinary optical transmission (EOT) structure, whereas 95.7% modulation efficiency was predicted by calculations[79].

1.3 Metasurfaces

Disclaimer: this subsection (1.3 Metasurfaces) of the dissertation is published in Nanophotonics. Reprinted with permission from Choudhury *et al.*, Nanophotonics 7 (6), 959-987, 2018. Copyright 2018 De Gruyter.

Metasurfaces are judiciously engineered electromagnetic interfaces which can manipulate many of light's quintessential properties, such as amplitude, phase, and polarization. These artificial surfaces are composed of subwavelength arrays of optical antennas that experience resonant light-matter interaction with incoming electromagnetic radiation. Their ability to arbitrarily engineer optical interactions has generated considerable excitement and interest in recent years and is a promising methodology for miniaturizing optical components for applications in optical communication systems, imaging, sensing, and optical manipulation. Based on the constituent materials, metasurfaces can largely be classified into plasmonic (metallic) metasurfaces and dielectric metasurfaces. Due to the distinct optical properties of metallic and dielectric materials, these two classes of metasurfaces are suitable for different applications, albeit some overlaps do exist. In general, plasmonic metasurfaces have tighter field confinement therefore better device miniaturization than dielectric metasurfaces, but at the cost of lower efficiencies due to the inevitable optical loss in metals. For the same reason, plasmonic metasurfaces find excellent uses in applications such as optical heating, cancer treatment, energy harvesting, sensing, where optical losses are desired. On the other hand, dielectric metasurfaces are especially suited for planar lens designs (so-called "metalenses"), and some metalenses have been demonstrated with better performance than commercial bulk lenses at sub-micron scale thicknesses.

1.3.1 Plasmonic metasurfaces

Tiny nanoparticles of noble metals are used to colorize glass since ancient times[80]. 4th Century Roman Lycurgus cup shows different colors when the light is shone through it and when the light is reflected off from it. Polychrome lustre decorations from Abbasid era[81], and Cassius purple and ruby glass from renaissance period[82] demonstrate colorful pottery by using the characteristic red color of spherical gold nanoparticles. Such coloration can be explained by the interaction between nanoparticles and light, which forms the fundamental principle of plasmonics and plasmonic metasurfaces. Plasmonics deals with the coupling between the electromagnetic field and the electronic oscillations of material. Plasmon is a quantum of free electron oscillation. Free electron clouds in a metal can couple to light at an interface between metal and dielectric media and create surface plasmons. With adequately designed nanostructures made from metals, the surface plasmons make it possible to control light at the sub-diffraction scale.

Not only the plasmonic nanostructures can guide light at the nanoscale, but they can also increase the local intensity of electromagnetic field by orders of magnitude. This enhancement is possible due to the strong local field confinement near the metal surface of a nanostructure. For metallic subwavelength structures or nanoparticles, the electric field of incoming radiation can polarize the conduction electrons. The resulting plasmon oscillations are distributed over the nanoparticle volume and are localized within the particle. These plasmon oscillations are termed localized surface plasmons (LSPs). The displacement of the electron clouds from the lattice generates a restoring force that tries to pull the electrons back into the lattice. The nanoparticle, therefore, acts as an oscillator driven by the incoming field together with restoring Coulomb force and behaves as a simple dipole in the direction of the electric field. When the frequency matches the resonance-frequency defined by the shape of the particle, LSP resonance occurs, enhancing local field amplitude. The nanostructures can also introduce a local phase shift to the incoming light beam and manipulate its wavefront.

The concept of local phase shift generation using plasmonic nanostructures can be employed by introducing abrupt phase jumps with metasurfaces. When light travels through a plane that can introduce abrupt phase change, it has been shown that the light propagation needs to be explained with a modification of Snell's law by introducing an artificially engineered phase-gradient term. The resulting phase-gradient from a sub-wavelength thick structure is shown to bend light in anomalous directions[22]. Since most of the conventional optical devices rely on amplitude

or phase modulation of the incoming light, the ability of plasmonic nanostructures to introduce the abrupt phase shift can be used to engineer ultra-compact optical devices. An early demonstration of photonic spin Hall effect, with polarization dependent splitting of light, is also achieved by plasmonic metasurface[83]. Seminal work on plasmonic antennas with aluminum[84] spearheaded the field of Al-based plasmonic metasurfaces. Many of the first applications of metasurfaces demonstrate imaging and sensing at the nanoscale, namely sub-diffraction lensing[24], [85]–[89] , spectroscopy[90], monochromatic holography[91]–[98], color holography[28], [99]–[101], polarization converters[102]–[107], vortex plates[108]–[110], invisibility cloaks[111], polarization-selective elements[112]–[115], etc.

Despite all the promising applications of plasmonic metasurfaces, optical losses in plasmonic devices severely limit their use in replacing conventional optical elements. As electron clouds in the metal oscillate while interacting with the incoming electromagnetic wave, they experience scattering in the material that causes heat generation. Although for the best plasmonic material, low loss (small imaginary part of permittivity) and high plasmonic property (large negative real part of permittivity) are essential, the losses cannot be avoided entirely. Even for an ideal plasmonic material with negligible loss, nano-structuring the metal causes the magnetic field of an incoming electromagnetic wave to be truncated as the wave interacts with the free electrons of the structure. Truncating the magnetic field, in turn, results in the conversion of stored magnetic energy into kinetic energy of electrons and causes a loss termed the Landau damping[46]. Compared to dielectric metasurfaces discussed in the next section, plasmonic metasurfaces will be therefore inherently less efficient but will have tighter field confinement, broader bandwidth, and smaller device footprint. For applications specific to plasmonic metasurface, the tradeoff between field confinement and loss must be made. Plasmonic metasurfaces are particularly useful, however, when optical losses are desired, such as in heating or absorber devices. Scattering loss minimization for plasmonic metasurface has been proposed through impedance matching[116], but the rest of the losses are inherent in plasmonic systems. Applications for plasmonic metasurfaces are emerging exploiting their ability to strongly confine field such as color filter and displays[117]–[119], enhanced harmonic generation[120]–[122], improved nonlinearity[123], [124], detection sensitivity improvement[73], [125], [126], absorbers[127]–[129], perfect absorber and efficient thermal emitters[130]–[132], photocatalysis[133], high temperature applications such as thermo-photovoltaics[134], heat-assisted magnetic recording[135] etc.

Conventional plasmonic materials such as gold and silver have been historically used for most of the early metasurface applications. Bulk silver has good plasmonic properties in the visible frequencies, but evaporated silver, which is most commonly used in metasurfaces due to the relatively easy fabrication, is prone to be lossier due to electron scattering at grain boundaries. Also, it is fundamentally challenging to grow ultrathin (on the order of few nanometers) gold and silver films, because these two materials tend to form nano-islands rather than continuous films at thicknesses below 10 nm. From the fabrication standpoint, gold and silver are also not compatible with the standard complementary metal-oxide-semiconductor (CMOS) technology, as silver has low chemical stability and gold is easily diffused into the substrate. Additionally, these noble metals have low melting temperatures. Therefore, the nanostructures made of noble metals easily deform at elevated temperatures. Consequently, noble metals are not suitable for high-temperature applications, which is a dilemma for plasmonics because the plasmon oscillations unavoidably heat up the metals significantly, at least within the spatial field confinement. Recently, it has been shown that thin dielectric coated nanostructured metal can be used for refractory plasmonics and nonlinear optics applications, by improving the temperature stability of the structured metal[136][137]. For stronger field confinement and high-temperature applications beyond noble metals' capabilities, new plasmonic materials are necessary. Study of alternative plasmonic materials has become a new field of itself and has found functional devices using the merger of metasurface with these materials' applications[138].

1.3.2 Dielectric metasurfaces

Since the onset of the successful demonstration of light bending at ultrathin scale[22], [23], the field of plasmonic metasurface has seen rapid growth due to the compactness, high optical confinement, and efficient hot electron generation found in such systems. As discussed in the previous section, plasmonic metasurfaces suffer from intrinsic optical losses because of strong electron-electron and electron-phonon scattering in metals, which limit the efficiency of functional optical devices such as lenses, holograms, wave plates, spectrometers, etc.[46]. The quest for highly-efficient planar optical manipulators has led to the development of all-dielectric metasurfaces. Unlike plasmonic metasurfaces which rely on LSP resonances to realize their features, dielectric metasurfaces are based on the collective light scattering (known as Mie

scattering) off the constituent high-index dielectric nanoparticles with dimensions comparable to the wavelength of light inside the particles[21], [139]–[141].

Optical loss can be minimized in all-dielectric metasurfaces as the large bandgap energies in dielectric materials limit optically induced interband transitions. Therefore, when light (with sub-bandgap energies) impinges upon dielectric nanoparticles, no free charge carriers are available, and only displacement currents instead of conduction currents are induced. This results in negligible optical losses and high electric field concentration *inside* the dielectric nanoparticles, in contrast to metallic nanoparticles where a significant portion of the incident optical energy converts to heat, and strong electric field concentration happens close to the surface outside the nanoparticles. Because of the low-loss feature, all-dielectric metasurfaces significantly surpass plasmonic metasurfaces in efficiency and resonance quality factor. Electromagnetically induced transparency (EIT) with a quality factor of ~600 has been demonstrated in all-dielectric metasurfaces[142], [143], representing an enormous advancement from plasmonic EIT metasurfaces with a quality factor on the order of 10. It has been recently pointed out that bounded states in the continuum (BICs) can be excited in all-dielectric metasurfaces with even higher quality factors (in theory infinite quality factor for metasurfaces with infinitely large lateral dimensions)[144], [145], efforts towards this direction are underway among several research groups. While it might not be surprising that all-dielectric metasurfaces outperform metallic metasurfaces in transmission applications since metals exhibit large optical reflection and absorption, even in reflectors where metals find most efficient applications, experimentally demonstrated all-dielectric near-perfect (99.7%) reflectors outperform metallic mirrors in efficiency which experience ~2% intrinsic loss[146], [147].

The optically induced magnetic response in metallic nanoparticles (other than split-ring structures) is negligible because the field vanishes inside the particle. In dielectric nanoparticles, however, both electric and magnetic responses of similar strengths can be observed. Strong magnetic dipole resonance arises in dielectric nanoparticle when the induced displacement current circulates inside the nanoparticle, and electric dipole resonance arises when induced displacement current oscillates linearly. The possibility to engineer both electric and magnetic resonances in dielectric nanoparticles endows all-dielectric metasurfaces with functionalities unattainable in their plasmonic counterparts. First, dielectric nanoparticles can be engineered for unidirectional light scattering. For dielectric nanoparticles of a certain size, at some well-defined frequency, the

electric and magnetic dipoles can be excited to oscillate in phase with equal strengths. Under such condition, Mie theory shows that the backscattering cross section diminishes due to the destructive inference from the two dipole oscillations[139], [148]. This principle has been used to engineer flat reflection-less all dielectric metasurfaces, manifesting itself as an advantage over conventional optics, as multiple optical layers or components are usually required to eliminate the back reflection. Second, the near-field enhancement of dielectric nanoparticles can be utilized to enhance nonlinear effects. In a recent work, Shcherbakov *et al.* showed that the third harmonic generation (THG) intensity could be improved by two orders of magnitude in silicon nano-disks compared to unstructured bulk silicon close to the magnetic dipole resonance[149]. THG enhancement has also been demonstrated with silicon metasurface exhibiting strong near-field enhancement from Fano-type resonance by Yang *et al.*, who achieved a THG enhancement factor of 1.5×10^5 on Si metasurface relative to unpatterned silicon[150]. Similar studies on nonlinear effects can be potentially carried out on metasurfaces made of diamond, a material that exhibits relatively high refractive index and can handle high optical powers[151]. Additionally, with the recent progress towards integrated diamond photonics and color centers[152]–[157], diamond metalens has been made to image single quantum emitters in situ[158].

In addition to unidirectional scattering and nonlinear effect enhancement, engineering of both electric and magnetic resonances in dielectric nanoparticles also enables redirecting light with more control than plasmonic metasurfaces. Similar to plasmonic metasurfaces, light manipulation (focusing, diffraction, beam steering, holography, etc.) with dielectric metasurfaces is achieved via phase control by individual subwavelength optical scatterers or pixels. Early in the 1990s, a very similar technique has been developed based on mimicking gradient index material with pixelated dielectric pillars whose local effective index is controlled by the filling ratio of dielectric to air in each pixel[159]–[161]. As the research field developed, the technique shifted to controlling the phase of the scattered light by varying the dimensions (and sometimes the shape) of dielectric scatterers, so that the scattered light from individual scatterers interfere and form a desired wavefront in the far field. The presence of both electric and magnetic resonances in the same frequency range enables full 2π phase control in a single dielectric structure layer by varying only the size of the dielectric nanoparticle, whereas only π phase control can be achieved using single layer plasmonic structures. Because the phase tuning happens close to the electric and magnetic dipole resonances, such phase control technique is named *resonant tuning*[162]–[167].

The scattered light from resonant tuning metasurfaces has the same polarization as the incident light. Phase control with dielectric metasurface can also be achieved in a non-resonant manner, which requires birefringent elements hence is termed *geometric tuning*[168]–[172]. The birefringent element imparts phase shifts ϕ_x and ϕ_y on light linearly polarized along its fast and slow axes. For half-wave plate birefringent elements ($|\phi_x - \phi_y| = \pi$), the imparted phase profile is equal to $\phi(x, y) = 2\theta(x, y)$, where $\theta(x, y)$ is the angular orientation of the birefringent element, and x, y are the spatial coordinates of the birefringent element. Such tuning mechanism requires circularly polarized light, and imposes two restrictions on the manipulated light: the phase profile imparted on left circularly polarized (LCP) light and on right circularly polarized (RCP) light are equal and opposite in sign (that is, $\phi_{LCP}(x, y) = -\phi_{RCP}(x, y)$); and the handedness of polarization reverses upon reflecting off or transmitting through the metasurface.

Dielectric metasurfaces are normally constructed by a periodic or another deterministic arrangement of high index subwavelength dielectric scatterers (or its inverse). However, they should not be confused with photonic crystals which are also made as periodic arrays of scatterers. Dielectric metasurfaces' function relies on the collective optical response of individual constituent building blocks to form the desired wavefront in the far field. Therefore, dielectric metasurfaces are radiative in nature, whereas photonic crystals are built on constructive and destructive inference from periodic dielectric elements and solely rely on diffraction. Because of this difference, dielectric metasurfaces and photonic crystals can be distinguished by their Mie resonance wavelength (λ_{Mie}, controlled by dielectric constant of nanoparticles) and Bragg resonance wavelength (λ_{Br}, controlled by lattice periodicity): when $\lambda_{\mathrm{Mie}} > \lambda_{\mathrm{Br}}$, Mie scattering dominates in dielectric nanoparticles and the periodic collection of dielectric nanoparticles form a metasurface; when the period is increased such that $\lambda_{\mathrm{Mie}} < \lambda_{\mathrm{Br}}$, the structure enters photonic crystal regime[21]. From an experimental perspective, 2-dimensional (2D) metasurfaces are usually irradiated at angles normal to the plane of the metasurfaces (or at reasonably small angles with respect to the normal axis) and operate in reflection or transmission modes. In contrast, the in-plane guided modes in 2D photonic crystals are usually launched in the plane of the periodic arrays by optical couplers, and cannot be miniaturized[140].

1.4 Graphene photodetectors

Photodetectors (PDs) are important components in modern sensing systems, they function by converting photon energies to electrical current or voltage. Currently, a major portion of PDs are made of conventional bulk semiconductor materials such as silicon[173], germanium[174], indium gallium arsenide[175], etc., due to their excellent optoelectronic properties and the well-established fabrication/manufacturing technology. However, these materials are limited by their detection bandwidths. Since they have finite bandgaps, photons with sub-bandgap energies cannot excite interband transitions hence cannot be detected. Additionally, the moderate electron and hole mobilities in these materials limit the operating speed of the optoelectronic devices. Graphene provides excellent solutions to the problems stated above. First, it is a gapless material, meaning that it is not limited by detection bandwidth when used as a photodetection material. Second, graphene has remarkably high room temperature electron mobility of 15000 $cm^2V^{-1}s^{-1}$, compared to crystalline silicon's 1400 $cm^2V^{-1}s^{-1}$, graphene PDs are promising for ultrahigh speed operations. Third, graphene has uniform optical absorption at energies greater than $2E_F$, which results in uniform photoresponse in PDs where intrinsic graphene sheet is used as the photo-absorbing material, in contrast to bulk semiconductor PDs where a strong photoresponse is usually observed at photon energy equal to the bandgap energy. Fourth, graphene is a flexible 2D material, thus can be used to make flexible and lightweight devices.

The two major mechanisms that enable photocurrent or photovoltage in graphene are the photovoltaic (PV) effect and photothermoelectric (PTE) effect. The PV effect in graphene is similar to that in other semiconductor materials, where incoming photons (with energies greater than $2E_F$) excite electrons from valence band to conduction band, which are then harvested by built-in electric field at graphene-metal interface or external electric field to give rise to photocurrent/voltage[176]–[178]. The ultrahigh carrier mobilities in graphene lead to ultrafast time response in graphene PV detectors[179], [180]. PTE effect in graphene arises when optically-induced heating happens at a junction where the doping level differs on two sides (n-p, p-p^+, n-n^+, etc.). Because the Seebeck coefficient in graphene depends on its doping type and level, when a non-uniform temperature distribution is introduced at a junction, net flow of electric charge carriers will be induced due to the difference in Seebeck coefficients at two sides of the junction, giving rise to photocurrent/voltage[181]–[183]. Because these two effects happen under similar condition (light impinging on junction with different doping types/levels on two sides, e.g. metal-

graphene interface), they coexist in the most studied metal-graphene-metal photodetectors (MGM-PDs). The governing equation for photocurrent/voltage generation in graphene of size $L \times W$ is given by[182]:

$$I = \int_0^W \int_{-L/2}^{L/2} (s(y)\nabla T_{el} - \sigma^{-1}(y) e\eta n_x \nabla U_g) \frac{\mathrm{d}y\mathrm{d}x}{RW} \tag{1.4}$$

where $s(\mu) = -\frac{\pi^2 k_B^2 T}{3e} \frac{1}{\sigma} \frac{\mathrm{d}\sigma}{\mathrm{d}\mu}$ is the Seebeck coefficient in graphene, T_{el} is the electron temperature, σ is graphene electrical conductivity, e is electron charge, η is the mobility at energy $\varepsilon \sim (1/2)hf$, n_x is the steady state density of photo-excited carriers, and $-\nabla U_g$ is the gate-induced electric field. The first term in Equation 1.4 denotes the PTE and the second term represents the PV contribution to graphene photocurrent/voltage generation. It can be shown that the ratio of PTE/PV contributions in graphene is:

$$\frac{I_{(HC)}}{I_{(PV)}} \approx \frac{e\alpha\varepsilon_0 l_0 L}{4\eta\tau_0 \Delta^2} \approx 2.6[\mu m] \sim 15 - 25 \tag{1.5}$$

where $I_{(HC)}$ denotes the photocurrent from PTE effect. It can be concluded from Equation 1.5 that in devices longer than 5~10 μm, the PTE effect dominates photocurrent/voltage generation in graphene. For the meanings of each quantity in the Equation 1.5, please refer to [182].

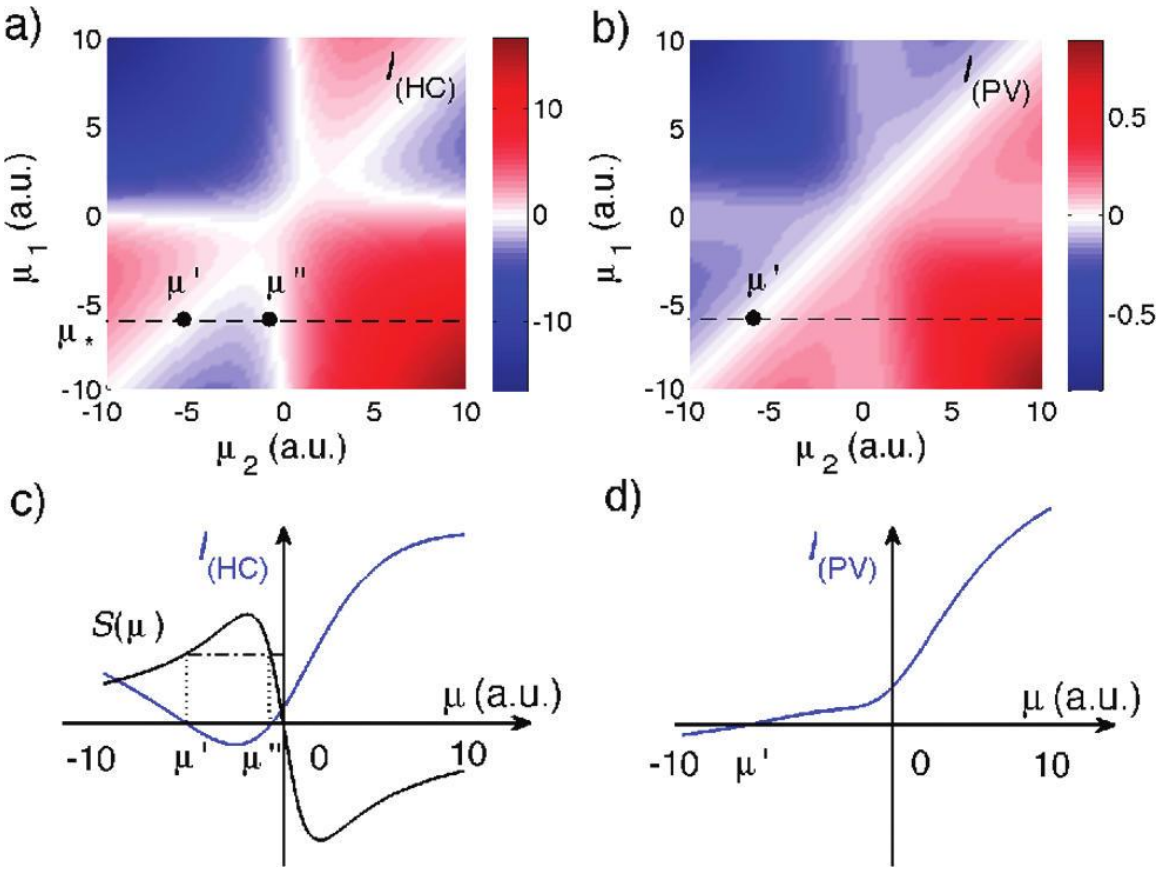

Figure 1.3 Theoretical calculation of graphene photocurrent

Photocurrent map as a function of chemical potentials μ_1 and μ_2 in a MGM-PD. Separately shown are the hot carrier (HC, photothermoelectric) contribution (a) and the PV contribution (b). Note multiple polarity changes for the HC contribution as opposed to a single polarity change for the PV contribution. The scales of $I_{(HC)}$ and $I_{(PV)}$ have been calibrated to agree with the ratio calculated with L = 6 μm. Current slices along the dotted lines $\mu_1 = \mu_*$ shown for the HC contribution (c) and the PV contribution (d). The Seebeck coefficient s(μ) is shown in (c).
From [182]. Reprinted with permission from Song *et al.*, Nano Lett. 11 (11), 4688-4692, 2011. Copyright 2011 American Chemical Society.

In this work, I discuss my efforts in using metasurfaces to study graphene plasmon resonance[184], enhance the performance of graphene photodetectors[73], characterize optical heating[185], and realize advanced optical data storage.

2. PLASMON RESONANCE IN MULTILAYER GRAPHENE NANORIBBONS

2.1 Introduction

Graphene is an extraordinary plasmonic material in IR frequencies due to its relatively small optical loss hence long SPP propagation length, ultrahigh confinement and dynamic tunability. These features are unparalleled by conventional noble metal plasmonic materials. Like extremely sharp tips (with tip radius of few tens of nanometers) are required to launch SPPs in graphene[52], [53], ultra-small resonators are needed to excite LSPs in graphene in the IR. Several reports have shown that tunable graphene plasmons exist in graphene nanoribbons with widths less than 100 nm[57], [59], and nanodisks with diameters ranging from 50 to 200 nm[58]. Although the tunability of graphene plasmon resonance makes graphene very promising for sensing applications in the biology-important IR frequencies, the relatively small resonance intensity of graphene fairly impairs its potential in practical use. Optical studies of AB-stacked bilayer graphene using a synchrotron light source reveal that the optical conductivity of multilayer graphene is higher than single layer graphene (SLG)[186]. While the optical conductivity of SLG is consistent with the prediction of the random phase approximation (RPA) theory[48], [187], the spectrum of AB-stacked bilayer graphene shows an additional sharp resonance at 0.37 eV due to strong interlayer coupling[186]. Theoretical studies also predict such an enhanced optical conductivity in bilayer graphene due to strong interlayer coupling[188]. If the number of graphene layers is further increased the optical conductivity spectrum becomes progressively more complex, but the general trend of increasing optical conductivity is maintained[186]. Additionally, multiple layer graphene devices have been shown to support stronger plasmon resonance at higher resonance frequencies than single layer graphene devices[189], suggesting that graphene multilayer stack is analogous to single layer graphene with higher effective doping level. Extending from these concepts and aiming to enhance the LSPR strength in graphene nanoribbons,

we experimentally investigate the plasmon resonance behaviors in double- and triple-layer graphene nanoribbons, and compare with that in single layer graphene nanoribbons.

2.2 Experiment

2.2.1 Fabrication and Raman characterization

We transfer and stack chemical vapor deposition (CVD) grown SLG sheets to form multilayer graphene samples due to difficulties in obtaining large area samples with controlled number of layers by mechanical exfoliation. SLG was first grown on 25 μm-thick copper (Cu) foils using an atmospheric pressure CVD process[190]–[192]. It was then sequentially transferred assisted by poly(methyl methacrylate) (PMMA)[190], [193] on three separate silicon substrates (1-10 Ohm-cm) with 300 nm thermal oxide (Si/SiO_2) to form single layer, double layer, and triple layer devices. Subsequently, a 500 μm × 500 μm active area was defined by photolithography and oxygen plasma etching. The source-drain contacts were defined by photolithography and subsequent Ti and Au metallization (5 nm and 55 nm respectively) on each sample.

It is well known that the layer stacking order in multilayer graphene plays a crucial role in determining its optical properties[194]. In our samples the domain orientation is not uniform across the graphene layer and there is also no definite stacking order between adjacent layers. Hence the optical response will be averaged over many domains with random orientations in a large area. We performed Raman spectroscopy (532 nm, circularly polarized laser with ~1 μm spot size and 1 mW incident power on the sample) to probe local layer orientations in our samples, since it has been shown to be a sensitive probe of the unique electronic and phonon band structures in graphene layers[195]. From the Raman spectra (shown in Figure 2.1 (a-c)) we clearly observe that the I_{2D}/I_G ratio is dependent on the measurement location in double layer and triple layer graphene samples in contrast to the single layer sample. This is due to changes in local lattice stacking order, which is consistent with previous studies in misoriented graphene[194], [196]. Hence, we should note that there is significant inter-layer stacking misalignment in addition to the well-known intra-layer domain misalignment in CVD graphene samples. Electrical testing of the devices was also carried out to verify the gate modulation of the source drain sheet resistance in multilayer graphene sheets. We found that SLG exhibits the highest dynamic range of variation of electrical resistance as shown in Figure 2.1(d), followed by double layer graphene and triple layer graphene respectively.

The gate induced carrier density modulation will allow multilayer graphene nanoribbons (GNRs) to support tunable plasmonic resonances. The strength of such resonances would be strongly dependent on the optical conductivity and carrier mobility.

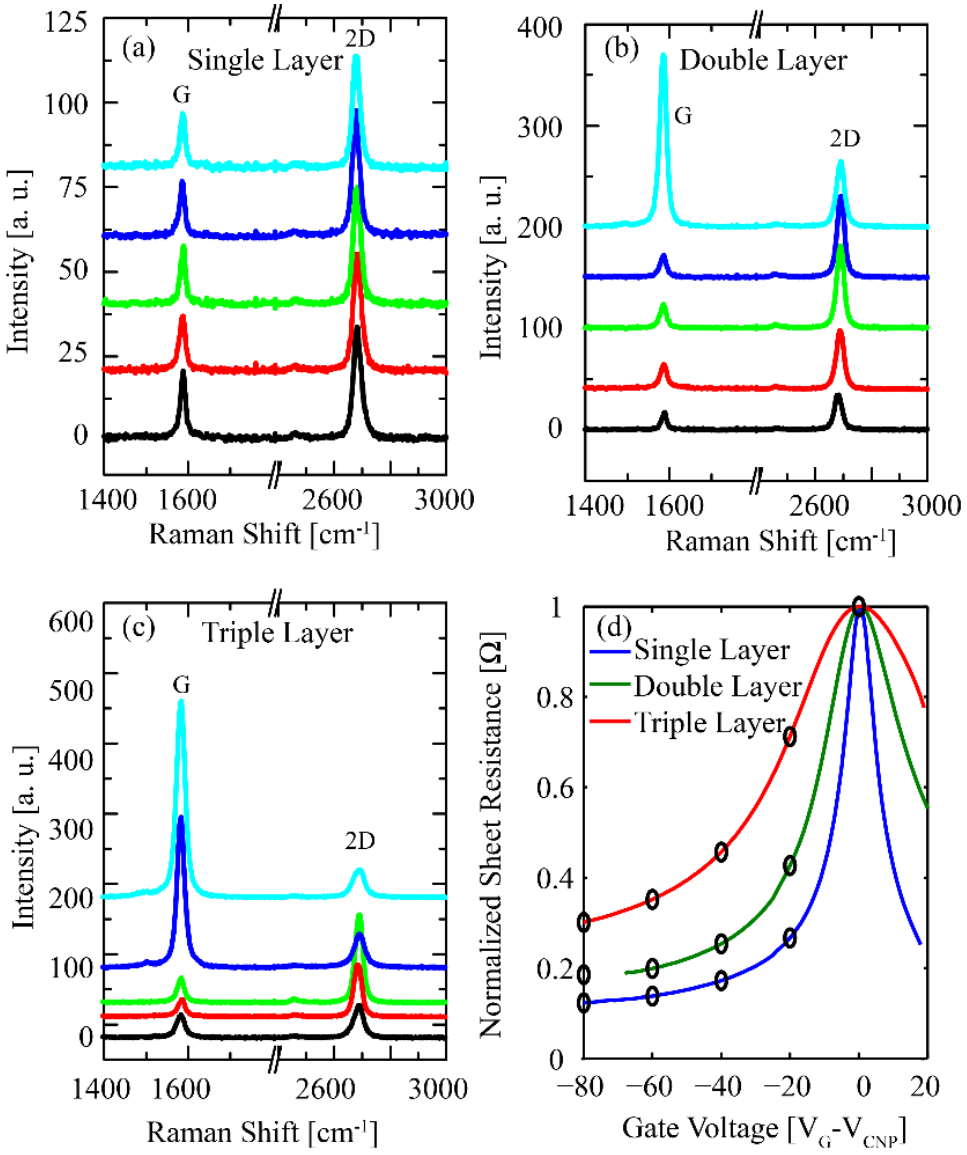

Figure 2.1 Raman characterization of multilayer graphene samples

(a-c) Raman spectra collected from five random locations on single layer, double layer and triple layer graphene respectively. All the measurements were performed using a 532 nm, circularly polarized laser source with a 100X objective (spot size ~1 μm) and 1 mW incident power. Individual spectra are offset for clarity. (d) The gate modulation of source drain resistance (normalized using sheet resistance at the charge neutral point (CNP) voltage) in different samples. SLG exhibits highest dynamic range of variation of electrical resistance followed by double layer and triple layer graphene respectively. The open circles represent the gate voltages at which IR reflection data shown later is collected.

The active area was patterned into GNRs (50-nm width and 150-nm period) using electron beam lithography on a positive electron beam resist (ZEP 520A, Zeon Chemicals, Inc). Figure 2.2 shows a simplified schematic illustration of our experimental setup as well as a scanning electron micrograph showing the patterned graphene ribbons. The number of broken C-C bonds increases significantly in nanopatterned graphene in comparison to unpatterned large area graphene, which leads to an additional peak (~ 1350 cm^{-1}) in the Raman spectra. However, we should note that even after patterning the I_{2D}/I_G ratio of SLG is greater than 2, indicating that the physical properties of graphene are intact. To investigate the plasmonic resonance in GNRs we measure the IR reflectance which we normalize to the reflectance at charge neutral point (CNP). The optical measurements were performed using a Fourier Transform Infrared (FTIR) spectrometer (Nicolet Magna-IR 850) with a microscope accessory (Nicplan IR Scope, 15X, NA 0.58 Reflectochromat objective). The incoming beam was polarized with electric field perpendicular to ribbons using a wire grid polarizer to excite transverse magnetic modes in GNRs.

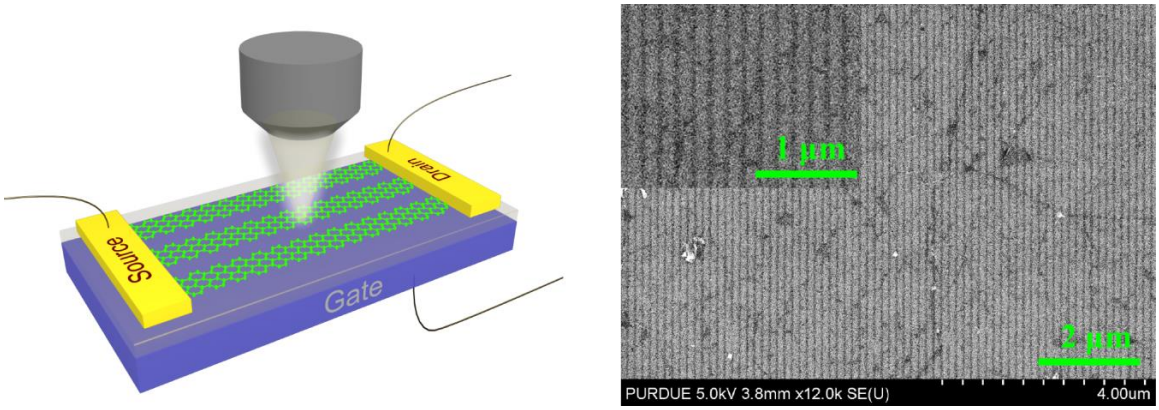

Figure 2.2 Schematic and SEM of graphene nanoribbons

(a) Simplified schematic of the experimental setup used for studying plasmon resonance in GNRs. The lattice orientation of GNRs in the figure is for illustration only and dimensions are not to scale; (b) Scanning electron micrograph of the fabricated GNRs on SLG sample with the inset showing a zoomed-in view of GNRs.

2.2.2 Fourier transform infrared spectroscopy characterization

When graphene is patterned into nanoribbons it can support surface plasmon standing waves when the condition $\mathrm{Re}(\beta)W = m\pi + \phi$ is satisfied, where β is the surface plasmon propagation constant, W is the width of the GNR, and ϕ is an arbitrary phase shift introduced by the reflection at the GNR edge and m is an integer[50], [57], [59]. Plasmon resonances in 50-nm-

wide GNRs occur in the wavelength range of 7 μm – 10 μm when graphene is doped to 1×10^{12} – 7×10^{12} cm^{-2} carrier densities. The experimental measurements of normalized reflectance on single layer- (SL-GNRs), double layer- (DL-GNRs) and triple layer graphene nanoribbons (TL-GNRs) as a function of Fermi energy E_F (which is related to carrier density) are shown in Figure 2.3. As the carrier density in GNRs is increased, the plasmon resonance becomes stronger and moves to lower wavelengths. There are two main peaks observed in the measured data – one above and another below the optical phonon wavelength of SiO2. These peaks result from hybridization of the graphene plasmon with the optical phonon in the SiO_2 layer[57], [59], [197]. The resonance strength increases from SL-GNRs to DL-GNRs, but the increase is slightly less for TL-GNRs. This could be due to higher losses resulting from the increase in the number of defects arising out of stacking multiple layers.

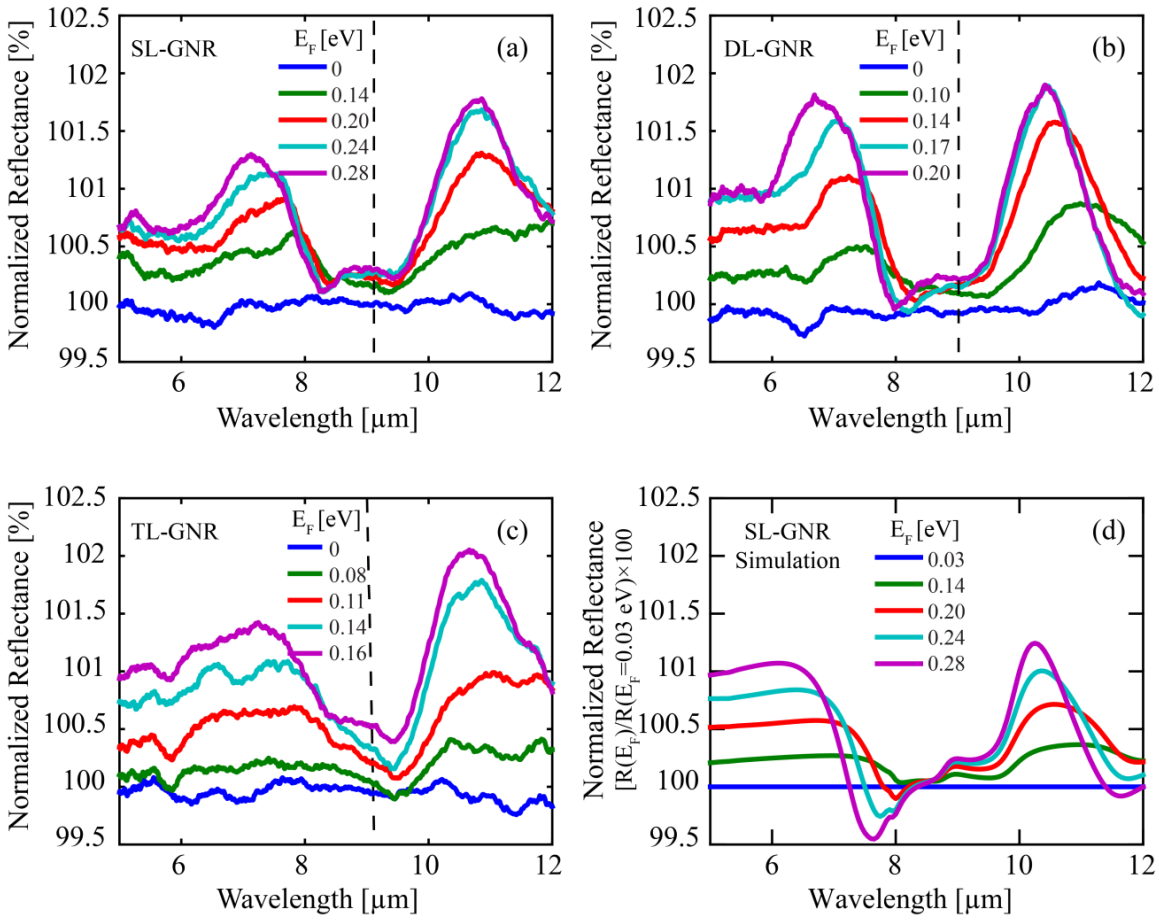

Figure 2.3 Reflectance from multilayer graphene nanoribbons

Modulation of IR reflectivity of GNRs fabricated on Si/SiO_2 substrate as a function of Fermi energy (E_F) of graphene; the vertical dashed line indicates the peak of SiO_2 optical phonon. Panels (a) - (c) show measured data on SL-GNRs, DL-GNRs and TL-GNRs, respectively. The reflection measurements were normalized to the reflection at the charge neutral point in our experiments. The width and period of GNRs were fixed at 50 nm and 150 nm respectively. (d) 2D full wave FEFD simulations of SL-GNRs with COMSOL Multiphysics using a surface current model for graphene; simulations performed at 0° to 35° angles of incidence (φ) with 5° spacing were averaged to obtain the curves shown here. The Fermi energy for each sample was calculated using a uniform charge approximation which does not take into account the screening and interlayer coupling effects.

In Figure 2.4 we plot the peak intensities of the resonance peaks shown in Figure 2.3 as a function of Fermi energy. We find that the peak resonance intensities in DL-GNRs are significantly stronger than SL-GNRs at a fixed E_F. When E_F is held constant the total carrier concentration of the stack is simply the carrier concentration in SL-GNRs times the number of graphene layers. We should note that a similar strong increase in peak intensity of TL-GNRs is not seen when compared to DL-GNRs. We believe that this could be due to the fact that the PMMA assisted transfer of

CVD graphene invariably creates some holes, folds and unavoidable residue. In fact, as we increase the number of layers, the non-uniformities become quite apparent in scanning electron microscopy (SEM) images (see Figure 2.2(b) for a representative image of SL-GNRs) even under an optical microscope. Therefore, we believe that this increase in number of defects per unit area leads to progressively higher losses, and weaker response which manifests as broadening of the plasmon peak in Figure 2.3(a-c). While the quality of our samples is comparable to the current state-of-the-art in CVD graphene, we can expect that further improvements in graphene growth/transfer processes will help in further enhancing the plasmon resonance strength.

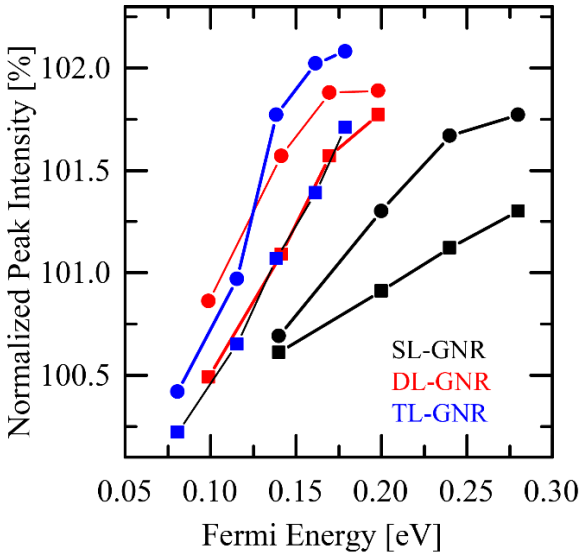

Figure 2.4 Peak intensity of the resonance peaks shown in Figure 2.3 as a function of E_F

The graphene plasmon hybridizes with the SiO_2 optical phonon to give two peaks shown in square and circle markers, respectively. Square markers indicate resonance peaks at shorter wavelengths, while circles indicate resonance peaks at longer wavelengths.

2.3 Numerical simulations

To gain further insight into the experiments we performed full wave finite element frequency domain (FEFD) simulations using a commercial software package (COMSOL Multiphysics, Wave Optics Module). We first accurately determined the dielectric function of SiO_2, which has a strong optical phonon overlapping with the graphene plasmon[57], [197], using IR spectroscopic ellipsometry. The retrieved optical constants for Si and SiO_2 layers are used in subsequent simulations and are shown in Figure 2.5. The optical properties of graphene were

calculated using the local limit of the Random Phase Approximation (RPA) and were modeled as a surface current in FEFD simulations.

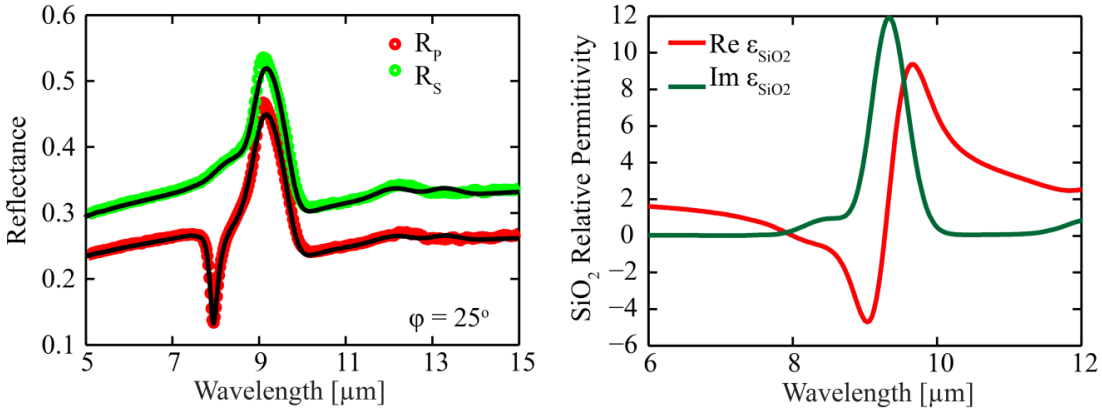

Figure 2.5 Reflectance and relative permittivity of SiO_2 substrate

Spectroscopic ellipsometry measurements of lightly doped Si with 300 nm thermal oxide at angle of incidence $\varphi = 25°$. The red and green markers show the measured reflectance from the sample in p and s polarizations, respectively. The black solid lines show the numerical fit of measured data using 9 Gaussian oscillators. The refractive index of Silicon was extracted to be a constant value of 3.42 in this wavelength range; (b) The real (red) and imaginary (green) parts of extracted permittivity of SiO_2 around the optical phonon wavelength.

The surface current model in COMSOL was first validated for an unpatterned single graphene sheet on SiO_2/Si substrate by modifying the classical Drude equation for the complex reflection coefficient[198] now rewritten as $r = (r_{01}^{\pm} + r_{01}^{m} r_{12} e^{i2k_1 d})/(1 + r_{01}^{\mp} r_{12} e^{i2k_1 d})$. The classical Fresnel coefficient for p-polarized light, $r_{12} = (e_2 k_1 - e_1 k_2)/(e_2 k_1 + e_1 k_2)$, was still applicable at the second interface with no graphene sheet, with $k_i = \frac{\omega}{c}\sqrt{\varepsilon_i - \varepsilon_0 \sin^2 \varphi}\,, i \in \overline{0,2}$ for a given frequency of light ω and angle of incidence φ. While using $\xi = \sigma k_0 k_1/(\omega \varepsilon_0)$ three different permutations of a modified Fresnel coefficient at the first interface, $r_{01}^{\pm} = (\varepsilon_1 k_0 + \xi - \varepsilon_0 k_1)/(\varepsilon_1 k_0 + \xi + \varepsilon_0 k_1)$, $r_{01}^{\mp} = (\varepsilon_1 k_0 - \xi + \varepsilon_0 k_1)/(\varepsilon_1 k_0 + \xi + \varepsilon_0 k_1)$, and $r_{01}^{=} = (\varepsilon_1 k_0 - \xi - \varepsilon_0 k_1)/(\varepsilon_1 k_0 + \xi + \varepsilon_0 k_1)$, were required to account for the effect of the graphene layer. Here, ε_0, ε_1, ε_2 are the dielectric constants of air, SiO_2 and Si substrate, and σ, δ, and c are the conductivity of the graphene layer, the thickness of silicon dioxide and the free-space speed of light respectively.

We found that simulations at only normal incidence do not fully account for all the experimental features (see Figure 2.6). Therefore we developed a weighted averaging procedure

where contribution of each simulation performed with 0° to 35° angles of incidence was weighted with a Gaussian factor. The upper limit of 35° was chosen to account for the finite acceptance angle of the objective used in our experiment. The final results thus obtained capture the experimental data remarkably well as compared to just normal reflectance as shown in Figure 2.6. From this analysis we retrieved a carrier scattering time of ~10 fs for the unpatterned graphene sample which is 5 times lower than the value estimated using DC Drude model[56]. We also recently became aware of another work which reports an experimentally extracted scattering time of 18 fs, which is in the same range as our results[70]. In numerical simulations SL-GNRs were modeled as a patterned surface current. The results obtained with the averaging procedure described above are shown in Figure 2.3(d), where we see a qualitative agreement with the experimental results. A key difference is the considerably narrower plasmon peaks below the SiO_2 optical phonon wavelength in experiments when compared to simulations. When graphene is patterned into nanoribbons, the carriers are confined to a 1D strip leading to opening of an energy bandgap. At the same time there is also significant edge disorder leading to charge localization and a smaller effective width of the GNR[199]. The bandgap (E_{gap}) is found to be empirically related to GNR width (W) and disorder parameter (W^*) as $E_{gap} = \alpha/(W - W^*)$ based on electrical transport studies on epitaxial graphene[199]. According to these studies a rather large bandgap of 0.2 eV can be obtained for GNR widths of ~15 nm. It seems plausible that such a bandgap could reduce the optical loss at IR wavelengths, and consequently lead to narrower plasmon resonance peaks. Based on our numerical studies, we conclude that the experimental features cannot be attributed to variations in the width of the ribbons or carrier scattering time alone. Therefore, we believe that the optical conductivity for graphene ribbons should be re-derived taking into account the energy bandgap which is beyond the scope of this work.

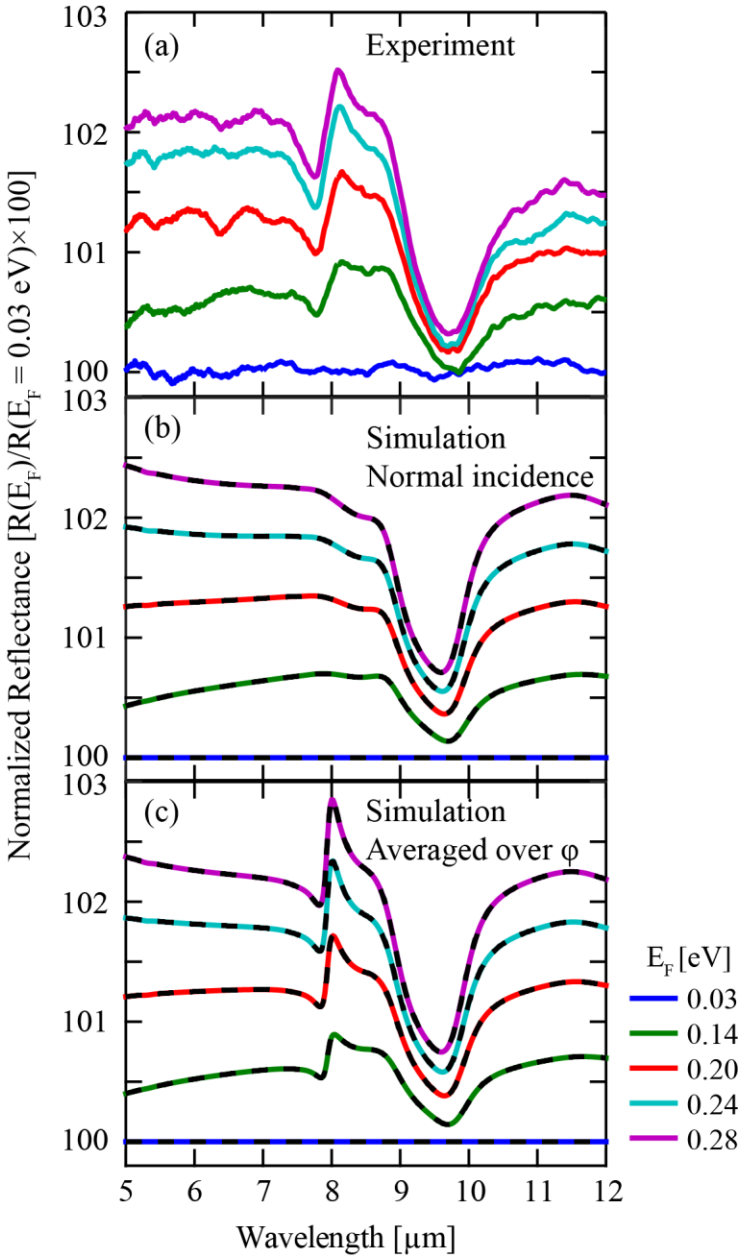

Figure 2.6 Measured and calculated reflectance spectra from graphene nanoribbons

(a) Modulation of IR reflectivity of CVD SLG on Si/SiO_2 substrate as a function of wavelength for different values of Fermi energy E_F. Measurements were performed using a Fourier Transform Infrared (FTIR) Spectrometer using unpolarized light and a microscope accessory (Objective: 15X, N.A. 0.58 Reflectochromat); measurements are normalized to reflection at the charge neutral point; (b)-(c) Analytical simulation results obtained at normal incidence and by averaging multiple simulations over a range of incidence angles (φ) respectively. We extracted a carrier scattering time of 10 fs from our numerical analysis. The dashed black curves show the matching results of the FEFD calculations that were used to validate the surface current approach with SLG models.

2.4 Conclusions and outlook

A major current challenge in the area of graphene plasmonics is to improve the strength of the plasmonic resonance. CVD grown graphene, which yields large sample area, has been predominantly used in graphene plasmon studies due to ease of optical characterization. However, growth kinetics and the transfer method of CVD graphene lead to disorder and hence poorer physical properties compared to epitaxial graphene films on silicon carbide. We investigated the behavior of plasmon resonance in GNR in single layer and multi-layer 'realistic' CVD graphene. Our experimental results indicate that plasmons are indeed supported by multilayer graphene nanostructures. When the carrier concentration of the graphene sheet is fixed, we find that DL-GNRs show stronger plasmon peaks when compared to SL-GNRs. It is worth noting that a later work also drew the same conclusion[200]. However, the increase is weak from DL-GNRs to TL-GNRs most likely due to inhomogeneities in local stacking order as well as random orientation of domains within CVD graphene. Systematic numerical simulations were performed in order to obtain a very good fit with experimental results for unpatterned graphene. Thus, we retrieved a carrier scattering time of ~10 fs from our graphene sample and developed an accurate numerical model which takes into account contributions from 0° to 35° incidence angles. The developed simulation model was applied for GNRs, and the results agree qualitatively with the experiment, but show broader plasmonic resonances. We believe that this could be due to opening of the bandgap close to the Dirac point due to nano-patterning. While incorporating a bandgap into the numerical model could theoretically lead to a better fit, we believe that such advanced modeling would first require better quality graphene samples and accurate measurements.

2.5 Appendix: robustness test for surface current based graphene numerical model

The ultrathin nature of graphene imposes great challenge on numerical simulations involving graphene and other bulk materials. In the past, multiple research groups have carried out finite element method (FEM) to model graphene as an entity with ultra-small fictitious thicknesses. This usually causes substantial meshing problems due to the large discrepancy in dimensions of graphene and other materials. On one hand, the graphene layer needs extremely fine mesh because graphene plasmons have much shorter wavelengths than free space light; on the other hand, generating large numbers of fine mesh in an ultra-small volume like graphene tends to reduce

overall meshing quality, since the volumes of graphene meshes are substantially different from those of other bulk materials. To overcome this problem, we proposed a surface current-based graphene FEM model in the aforementioned work, where graphene is set as a volume-less boundary condition instead of an entity with finite thickness/volume. It has already been shown in Figure 2.3(d) and 2.6(c) that this model can reproduce experimental results with satisfactory accuracy. In order to further test the robustness and accuracy of this model, we attempted to reproduce the experimental results from [78] using our proposed model. In [78], authors proposed a Salisbury screen configuration consisting of graphene nanoribbons and gold reflector spaced by a layer of silicon nitride (SiN), to enhance optical absorption by graphene nanoribbons. The resonance frequency and intensity can be varied by gating voltage. In Figure 2.7(a), we plot the simulated spectra of 40 nm wide graphene nanoribbon on 1 μm SiN and 100 nm Au, at various carrier densities, and compare them with the measured spectra from [78]. As is evident from Figure 2.7(a-b) and (c-d), a good match is achieved between the two, reinforcing the robustness and accuracy of our proposed numerical model.

In general, our proposed surface current based graphene model has the following advantages over conventional finite thickness model:

1. It is faster. In the two-dimensional simulation of Figure 2.7(a), each absorption spectrum takes about 1 minute to finish. The finite thickness model, however, requires tremendously larger number of meshes thus takes much longer time to solve.
2. It takes less memory. Each simulation in Figure 2.7(a) requires about 1 Gb memory. For the same reason as in 1, the large number of meshes necessary in finite thickness model requires more computational power.
3. It is more robust. Usually the accuracy of finite thickness model is very sensitive to the designated thickness of graphene layer, which is often set as a fitting parameter in simulations to find the best match with experiment. As a result, the optimal graphene thickness varies from 0.3 to 3 nm in reported literatures. In our proposed surface current model, the graphene thickness is not a freedom, thus eliminating the need to tune this parameter. The simulated results converge very well with experiments, as are shown in Figure 2.3(d), 2.6(c) and 2.7(a).

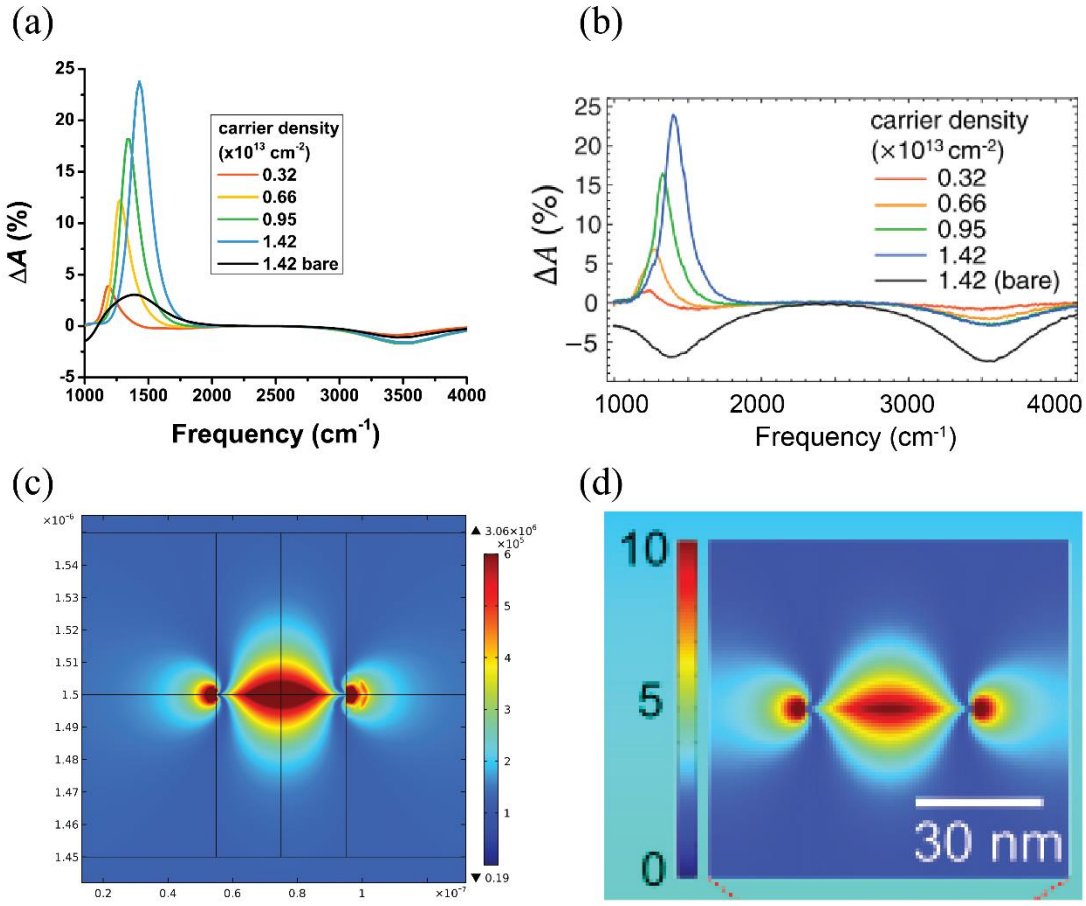

Figure 2.7 Robustness test for graphene numerical model against published work

(a) Simulated change in absorption spectra for 40 nm wide graphene nanoribbons on 1 μm SiN and 100 nm Au, with varying carrier densities, with respect to the absorption at CNP. The simulations are performed with surface current based graphene FEM model described in Chapter 2.3. Bare denotes the spectrum collected on unpatterned graphene (b) Measured absorption spectra under the same condition as in (a), from [78]. Reprinted with permission from Jang *et al.*, Phys. Rev. B 90 (16), 165409, 2014. Copyright 2014 American Physical Society. (c) Simulated electric field distribution on graphene nanoribbon at resonance, using the FEM method in (a). (d) Simulated field distribution on graphene nanoribbon at resonance, from [78]. Reprinted with permission from Jang *et al.*, Phys. Rev. B 90 (16), 165409, 2014. Copyright 2014 American Physical Society.

3. ENHANCED GRAPHENE PHOTODETECTOR WITH FRACTAL METASURFACE

3.1 Introduction

Graphene has been demonstrated as an appealing material for photodetection due to its unique properties such as wide optical absorption spectrum, wavelength-independent absorption, high room-temperature electron and hole mobilities, mechanical flexibility, and dynamic tunability in optical and electrical properties[18], [58], [65], [184], [201]–[205]. So far there are primarily five known physical mechanisms that enable photodetection in graphene: the photovoltaic effect[179], [180], [206], the photo-thermoelectric effect[182], [183], [207], [208], the bolometric effect[209], the photogating effect[210]–[212], and the surface plasmon-assisted mechanism[213], [214]. Among these, the photovoltaic (PV) effect makes use of the built-in electric field that is induced by the differently doped regions in graphene to separate the optically excited electron hole pairs in graphene and give rise to photovoltage, whereas the photothermoelectric (PTE) effect is associated with the photovoltage produced by the optically generated hot electrons in regions with different thermoelectric powers (Seebeck coefficients) in graphene: $V_{PTE} = (S_1 - S_2)\Delta T$, where S_1 and S_2 are the Seebeck coefficients of two regions in graphene with different doping levels, and ΔT is the electron temperature difference across the two regions. Both effects are thought to contribute in photovoltage generation in metal-graphene-metal photodetectors (MGM-PDs)[215], and make MGM-PDs the prioritized candidates for ultrafast graphene photodetector, owing to the high carrier transport velocity[179], [216] and extremely short carrier heating and cooling times[217]–[219] in graphene. Moreover, MGM-PDs are ideal for applications where zero power consumption and zero dark current are desired, because source drain bias and gate voltage, although useful for dynamically tuning the photogain, are not necessary for such detectors to be operative. Despite all the advantages of MGM-PDs (broadband operation, uniform sensitivity against wavelength, fast response speed, zero power consumption), the responsivity (sensitivity)

in MGM-PDs is notoriously low because graphene, which absorbs merely 2.3% of incident light[201], is used as the photo absorption material. On the other hand, plasmon oscillations have been known and widely utilized to enhance optical absorption and generate hot electrons in various optical systems. Unsurprisingly, efforts have also been made to enhance the responsivity in MGM-PDs using plasmonic nanostructures. However, the previously proposed plasmonic enhancement methods are mostly narrowband and polarization-dependent[30], [72], [74], [76]. Optical waveguides have also been demonstrated to enhance the optical absorption by almost 100% in graphene photodetectors[206], [219], but this method requires coupling light into waveguides which could result in a bulky experimental setup. Indeed, narrowband and polarization sensitive enhanced photodetectors are desirable in spectrally resolved and polarization specific photodetection scenarios, there is definitely a strong need for broadband and polarization insensitive enhanced photodetectors. In this work we propose a gold fractal metasurface design which has a relatively flat optical absorption in the visible part of the spectrum to realize broadband and polarization insensitive plasmonic enhanced graphene photodetector.

3.2 Fractal metasurface design and characterization

We begin by introducing a new fractal metasurface design. The metasurface is realized through a fractal tree to mimic the snowflake geometry. As demonstrated in previous works, the fractal metasurface has been shown to exhibit broadband absorption and multiple resonances with increased levels[220]–[222], where the practical examples include plasmonic elements[221] that follow the Cayley tree topology[223] or the nanostructured aluminum electrodes[222] following the classical space-filling curves of Hilbert and Peano[224], [225]. Here we choose the six-point asterisk shape as our seed geometry (the first-level fractal, Figure 3.1(a)). Construction of the branching is generated by recursive iterations that is different from the classical approaches to n-flake generation[223]. In our case, upon each iteration six new branches are only spread from each new root point. The angle between each branch is kept at 60°. The branch width and thickness are set to be 40 nm for all levels of iterations, while branch lengths at each level are decreased by the scaling ratio of 1/3 as the level increases, with a total level of 4, denoted by the red color in Figure 3.1(a). For the sake of fabrication and measurement conveniences, we designed the fractal metasurface with a diameter of ~10 μm to cover the whole area of illumination by the laser spot in our system. Nonetheless, due to the simple and inward scalability of fractal metasurfaces, it is

convenient to design metasurfaces that are fitted for other spot sizes and for enhancement at other desired wavelength ranges, while keeping the overall coverage area of the metasurface unchanged with increasing fractal levels. In order to increase the density of the branches within the illumination spot and to compensate for the intrinsic polarization anisotropy, we add another 3-level fractal structure concentrically with a 30° mismatch to the 4-level fractal structure, denoted in red color in Figure 3.1(b). All the arm lengths for the whole fractal metasurface are listed in Table 3.1.

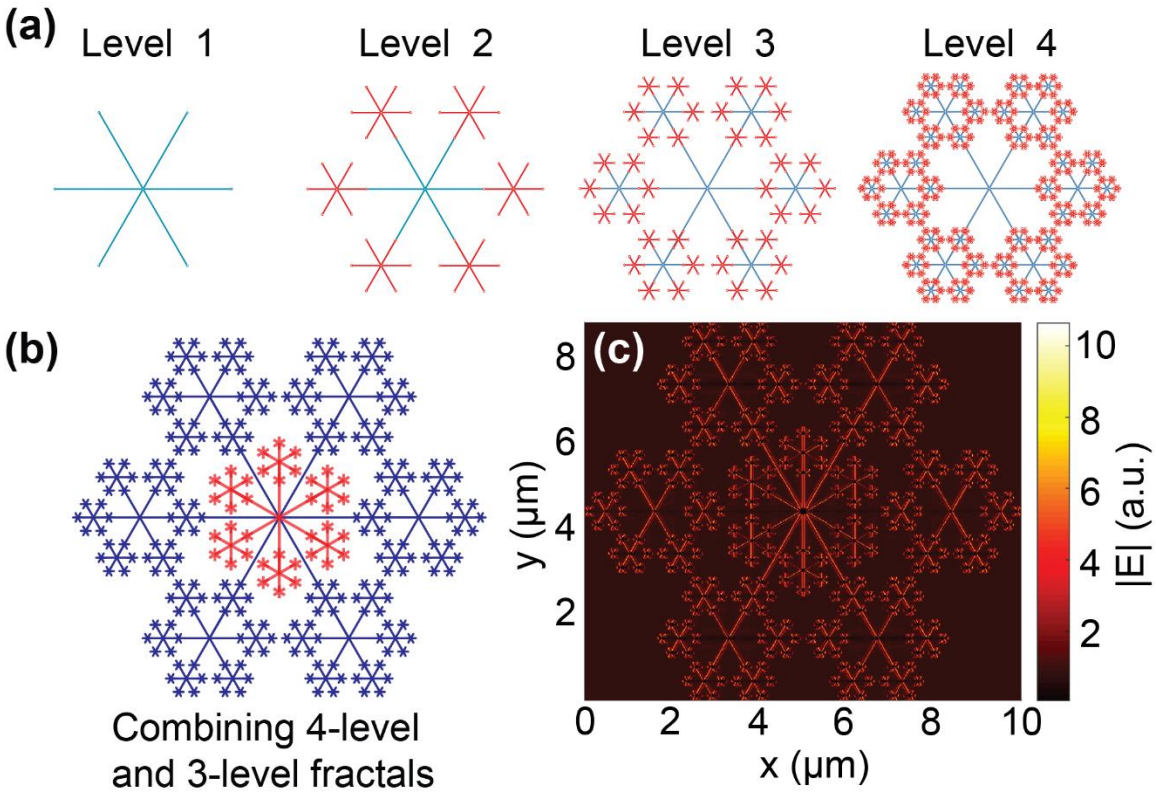

Figure 3.1 Fractal metasurface design

(a) Construction of the fractal design with "snowflake" geometry, from level 1 to level 4. (b) Total structure comprising of a 4-level (blue part) and a 3-level (red part) fractals utilized in the study. (c) FDTD simulated in-plane electric field (of the incident electromagnetic wave) distribution just underneath the gold fractal metasurface on a glass substrate under the excitation wavelength of 530 nm. The electric field is linearly polarized along y direction.

Table 3.1 Arm lengths for the whole fractal metasurface

Level number, *N*	1	2	3	4
4-level fractal arm lengths (μm, blue segments in Fig. 1(b))	3.47	1.15	0.38	0.13
3-level fractal arm lengths (μm, red segments in Fig. 1(b))	1.39	0.46	0.15	NA

Next, we investigate the optical characteristics of such gold fractal metasurface numerically through the finite-difference time-domain (FDTD) method[226]. We employ a dispersive model for gold, which is defined as the sum of a Drude term and two critical point terms and is implemented through a Generalized Dispersion Material model[227]. The parameters of the model are adopted from an online database[228]. We show one full-wave simulated in-plane electric field distribution just underneath the gold fractal metasurface when it is illuminated at the wavelength of 530 nm (Figure. 3.1(c)). The high intensity regions (hot spots) are tightly localized around the branches and edges of the fractal structures.

To further validate the performance of our metasurface, we performed near-field scanning optical microscopy (NSOM, MultiView 2000, Nanonics Imaging Ltd.) to elucidate the near-field characteristics of the plasmonic fractal. For near-field measurements, we fabricated gold fractal patterns of exactly the same dimensions on top of a bare glass substrate; this was necessary due to the strong absorption that would have otherwise occurred using a silicon substrate. The metasurface sample is illuminated from the far-field using a weakly focused 532 nm diode laser incident on the bottom of the metasurface i.e. the glass substrate side. The near-field signal is obtained by scanning a metal-coated (chromium and gold) tapered fiber with a 50-nm aperture above the surface of the sample. The scan is performed at a fixed distance of ~100 nm in order to mitigate damage to the tip and/or sample and to eliminate topographic artifacts in the signal[229]. Figure 3.2(a) shows the experimental near-field extinction map of the metasurface. To compare with experiments, we simulated—using an FDTD method—the electromagnetic fields in a plane 100 nm above the plasmonic metasurface assuming a 532 nm plane wave incident from the substrate side and applied a moving average weighted with a 50-nm disk to account for the

convolution of the tip[230]. Our results are well matched with experiment as illustrated in Figure 3.2(b) and indicate strong plasmonic extinction near the branches and edges of the fractal structure.

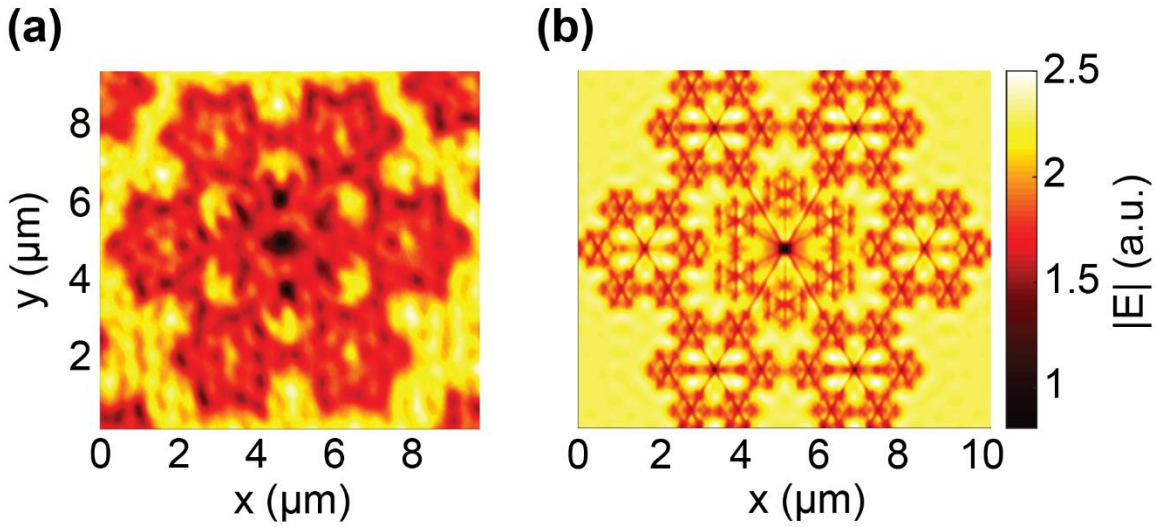

Figure 3.2 Measured and calculated near-field distribution for fractal metasurface

(a) Experimental near-field extinction map of the fractal metasurface, obtained using near-field scanning optical microscopy (NSOM). The measurement is done in collection mode at a wavelength of 532 nm. (b) The simulated electric field distribution at the wavelength of 532 nm. A floating window average is applied to mimic the 50 nm diameter aperture that is used in the NSOM experiment in (a).

3.3 Photoresponse characterization

When visible light is incident upon the fractal metasurface, it excites plasmon oscillation in the gold fractal structure, which in turn confines and enhances the electric field of the incident electromagnetic wave within nanometers of the structure, contributing to an extensive electron-hole pair generation and elevating the electron temperature through electron-electron interactions in graphene[231]. The generated carriers are then spatially separated/driven via the aforementioned built-in electric field (PV) and thermoelectric power differential (PTE) at gold-graphene interface, giving rise to a detectable photovoltage. Additionally, due to a combination of two orthogonally-oriented concentric hexagonal fractal geometries in an integrated metasurface design (see Figure 3.1(b), red and blue structures respectively), the enhancement in photovoltage detection is independent of the polarization angle of the incident electromagnetic wave, providing yet another feature unprecedented by the previously reported plasmonic enhanced MGM-PDs.

3.3.1 Device fabrication

In our experiment, we integrated the fractal metasurface with the drain contact of the graphene field effect transistor (FET) device, so that the metasurface is at the same electrical potential as the bulk drain contact, to facilitate the electron (hole) collection and also the theoretical analyzis. The device fabrication starts with the transfer of a monolayer graphene sheet[190] grown by chemical vapor deposition (CVD) onto a highly p-doped silicon substrate (0.001-0.005 Ω-cm) with a 300 nm thick dry thermal dioxide on top. The fractal metasurface with gold rod for electrical connection with the drain contact, and a ring encircling the fractal metasurface to maximize electron (hole) harvesting at the source contact, were defined by electron beam lithography (EBL), Ti (3 nm)/Au (40 nm) metallization and liftoff. The large sheet of graphene was then etched into smaller rectangles using photolithography and O_2 plasma etch. The bulk source and drain contact pads (3 nm Ti, 80 nm Au) were fabricated to directly cover the gold rods and partially the graphene sheet. Finally wire bonding the fabricated chip to printed circuit board was performed for electrical measurements.

3.3.2 Photovoltage measurement setup

The photovoltage response of our device was measured by the setup illustrated in Figure 3.3(a). A continuous wave laser (Ar-Kr) chopped at 1.1 kHz by an optical chopper was coupled to a 10× microscope and was then focused on the photodetector with a spot diameter of ~7 μm. The generated photovoltage was then measured via the source-drain contacts by a lock-in amplifier synchronized with the optical chopper. We first investigated the enhancement in photovoltage generation from the ring encircling the fractal metasurface. To do this, on sample 1 we fabricated a tip-and-ring structure without fractal metasurface, and placed it in parallel with the structure with fractal metasurface (see Figure 3.3(b)). By measuring the photovoltage generated on the tip ("spot B" in Figure 3.3(b)) and on the plain gold-graphene edge ("spot C" in Figure 3.3(b)), we observed an average of ~5× photovoltage enhancement on the tip. We then measured the photovoltage generated when the laser spot was incident upon the fractal metasurface ("spot A" in Figure 3.3(b)), denoted as $V_{fractal}$, and when the laser spot was incident upon the plain gold-graphene edge ("spot C" in Figure 3.3(b)), denoted as V_{edge}, and defined $V_{fractal}/V_{edge}$ as the enhancement factor of photovoltage generated on fractal metasurface to plain edge. The study of fractal metasurface photovoltage generation was carried out at six experimentally available wavelengths—476 nm,

488 nm, 514 nm, 530 nm, 568 nm, and 647 nm—to investigate the broadband enhancement effect in the visible spectrum. In this work, all measurements were done with zero gate voltage ($V_G = 0$) and source-drain bias ($V_{SD} = 0$), unless otherwise indicated. As an illustration, we show the photovoltage generated as a function of incident power at the wavelength of 568 nm in Figure 3.3(c) and (d), from which a linear relationship between the two can be seen, indicating that we were operating the device before absorption saturation[72].

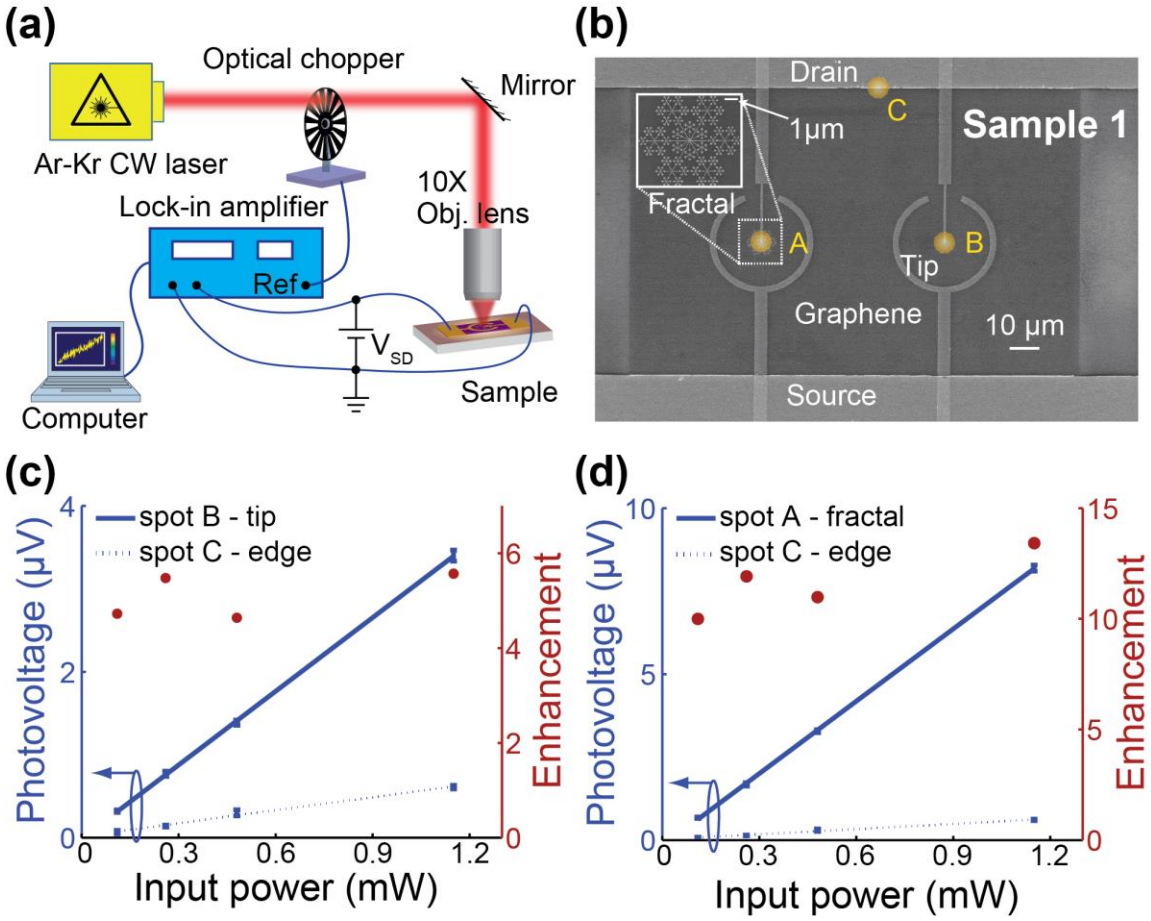

Figure 3.3 Characterization of graphene photodetector, Sample 1

(a) Experimental setup for photovoltage measurement; (b) Scanning electron micrograph (SEM) of sample 1 the graphene photodetector with the fractal metasurface and tip-and-ring structure (the white scale bar is 10 μm); inset image shows the zoomed-in view of gold fractal metasurface (the white scale bar is 1 μm). (c) Blue lines with error bars: measured photovoltage when laser is incident on tip without fractal metasurface (spot B in (b), solid line) and on plain edge (spot C in (b), dotted line) as a function of incident power, the error bars are experimentally measured data points and blue lines are linear fits to the experimental data; red circles: enhancement factors from tip to edge at individual tested incident powers. (d) Similar to (c), the measured photovoltage generated on fractal metasurface (spot A in (b), solid blue line) and on plain metal/graphene edge (spot C in (b), dashed blue line) as a function of incident power, and enhancement factors (red dots, right vertical axis) at each tested power. The measurements in (c) and (d) were carried out at the wavelength of 568 nm.

3.3.3 Spectral enhancement

To show the broadband nature of the photovoltage enhancement, we plot the enhancement factors $V_{fractal}/V_{edge}$ at the six tested wavelengths in Figure 3.4(a). The error bars come from the fact that the enhancement factors vary with varying incident optical powers. As is evident in Figure 3.4(a), enhancement factors ranging from 10 to 16 are achieved at the tested visible-spectrum wavelengths. We notice that although the simulated optical absorption of the fractal metasurface is rather flat in the investigated spectral range (shown by the cyan solid line in Figure 3.4(a)), the enhancement factors in photovoltage generation exhibit slight wavelength dependence – the enhancement factors increase with increasing wavelength. We believe that the reason for such behavior is two-fold. On one hand, it is caused by the greater photovoltage generated on the plain gold-graphene edge at shorter wavelengths due to stronger heating of gold pad, accounted for by the PTE effect in photovoltage generation. On the fractal metasurface, the entire metasurface area contributes to generating photovoltage ($V_{fractal}$), independent of incident light wavelength. On the plain gold-graphene edge (V_{edge}), however, larger/smaller area extending into the gold pad within the laser spot contributes to generating photovoltage at respectively shorter/longer wavelengths[215], [218]. As a result, the enhancement factors decrease at shorter wavelengths simply because the area of graphene that contributes to V_{edge} increases compared to that at longer wavelength, while it remains identical across the entire tested wavelength range for $V_{fractal}$. On the other hand, the Ti doping and intrinsic p-doping in bulk graphene induces p-p junction at the metal/graphene interface, where PV and PTE effects counteract with each other[182], [183]. The competition between the two effects could also be a reason of the increasing trend of enhancement factors with wavelength.

It is also known that the source-drain bias in graphene photodetectors can alter the band bending across the graphene FET device, making it a handy mechanism to tune the photovoltage responsivity. We show in Figure 3.4(b) that the amplitude of the photovoltage increases monotonically with increasing source-drain bias and the photovoltage can be tuned up to 24 μV, three times of that at zero bias. We did not observe reduced responsivity up to V_{SD} = 0.25 V, indicating that the breakdown field of the graphene channel, which is the limit of the bias that can be applied to the device, has not been reached. In Figure 3.4(c) we show that the photoresponse is insensitive to the polarization angle of incident light, as is expected from the aforementioned hexagonally symmetric geometry of the fractal metasurface design. The two panels in Figure 3.4(d)

indicate that the fractal metasurface provides more polarization robustness over the tip-and-ring structure which exhibits 50% drop in responsivity when light is polarized in the y direction. We simulated the absorption spectrum of the metasurface under 0° (E-field along x-axis in Figure 3.1(c)) and 90° (E-field along y-axis in Figure 3.1(c)) polarizations, and observe only negligible difference between the two. The experimental and simulation results demonstrate the robustness of the photovoltage enhancement by the proposed fractal metasurface with respect to polarization of incident light.

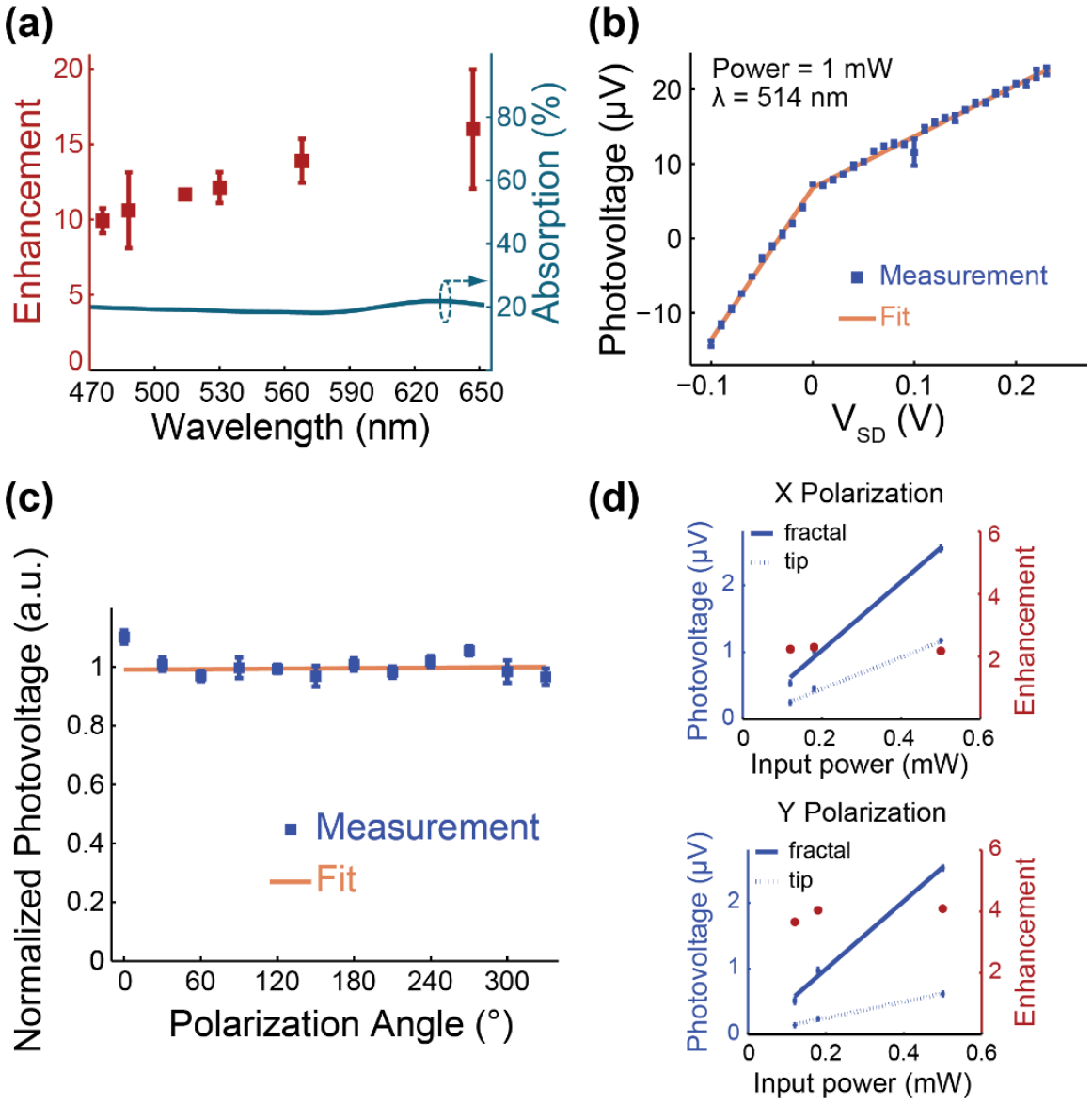

Figure 3.4 Performance of fractal metasurface enhancement

(a) Red markers with error bars: measured enhancement of photovoltage generation ($V_{fractal}/V_{edge}$, spot A to spot C in Figure 3.3(b)) over a wavelength range from 476 nm to 647 nm; cyan curve: the simulated absorption spectrum of the fractal metasurface. (b) Measured photovoltage as a function of source drain bias V_{SD}. Measurement was done at the wavelength of 514 nm with an input power of 1 mW. Blue markers are measured data points and orange curve is linear fit to the data points. (c) Normalized photovoltage as a function of incident light polarization angles. Blue markers are measured data points and orange curve is linear fit to the data points. (d) Blue lines: measured photovoltage generated on fractal metasurface (spot A in Figure 3.3(b), solid lines) and on tip (spot B in Figure 3.3(b), dashed lines) with x-polarized light (upper panel) and y-polarized light (lower panel). See Figure 3.1(c) for x and y directions.

In order to compensate for the partial enhancement due to the reduced source-drain distance for spot A in sample 1, we fabricated sample 2 where we placed a fractal metasurface encircled by a 30 μm ring in parallel with a plain source-drain structure with 30 μm separation on the same graphene sheet, and studied the enhancement of photovoltage between the two structures. Similar to sample 1, in sample 2 we study the ratio of photovoltage generated when laser is incident on fractal metasurface (spot A in Figure 3.5(a)) to that generated when laser is incident on one of the 30 μm separated source drain contacts (spot B in Figure 3.5(a)), where the maximum photovoltage happens in pristine MGM-PDs[176], [178]. In Figure 3.5(b) we plot the enhancement factors at five tested wavelengths for sample 2. It can be seen that although the enhancement factors are reduced compared to those of sample 1, they are still close to 10 and can be as large as 13 at longer wavelengths.

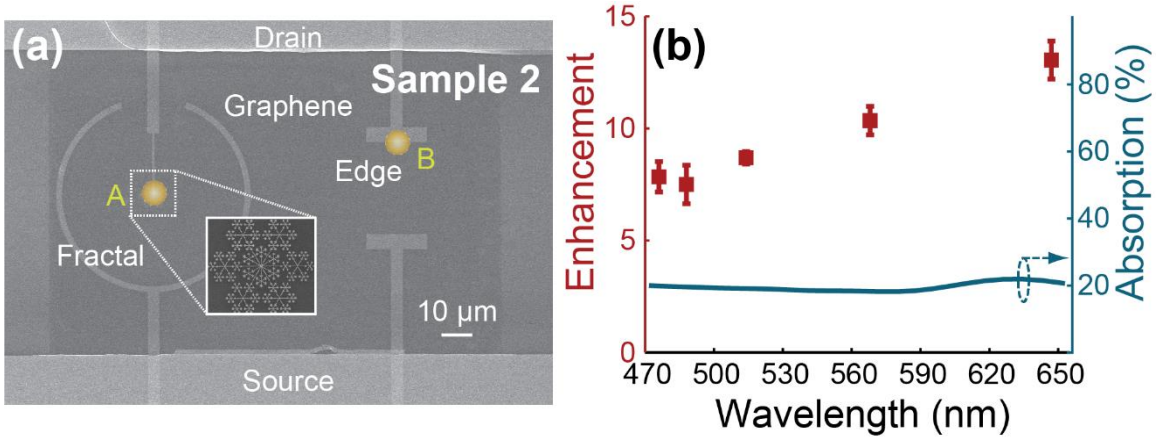

Figure 3.5 Characterization of graphene photodetector, Sample 2

(a) SEM of the graphene photodetector sample 2 with the fractal metasurface (the white scale bar is 10 μm) encircled by 30 μm radius ring and source-drain contacts separated by 30 μm; inset image shows the zoomed-in view of gold fractal metasurface. Similar to sample 1, the ratio of the photovoltage generated on spot A to that generated on spot B is defined as the enhancement factor. (b) Similar to Figure 3.4(a), the measured enhancement of photovoltage generation (red markers with error bars, left vertical axis) from 476 nm to 647 nm and the simulated absorption spectrum of the fractal metasurface (cyan curve, right vertical axis) on sample 2.

3.3.4 Enhanced graphene photodetector on glass substrate

Although the designed metasurface enhances photovoltage by an order of magnitude compared to unpatterned gold contact, it only absorbs ~20% light while allowing ~80% light to pass through. One way to further enhance the photoresponse is to fabricate multiple such fractal metasurface enhanced graphene photodetectors on transparent substrates, then stack them along

the optical beam path and connect them electrically in parallel. The resulting photovoltage enhancement is expected to scale with the number of photodetectors in the stack (at the cost of losing gate voltage tunability because of lack of back gate electrode). As a preliminary examination to this possibility, we carried out similar studies on fractal metasurface enhanced graphene photodetector on transparent glass substrate (sample 3). A step of chrome (Cr) deposition on hard-baked PMMA is required prior to EBL writing in addition to the fabrication technique used for SiO_2/Si substrates, to lessen the electron charge accumulation in PMMA on non-conducting substrate. The fabricated sample is shown in Figure 3.6(a). Here we designed another geometry for comparison, where the fractal metasurface encircled by a 30 μm radius ring is replaced by unpatterned gold disk of similar size. The measured photovoltage enhancement from fractal metasurface to unpatterned gold disk is plotted in Figure 3.6(b), where strong wavelength dependence can be observed. Note that the large error bars at longer wavelengths are largely due to the heavily near-zero fluctuating photovoltage signals on unpatterned gold. Plotted in the same figure is also the ratio of measured optical absorption from fractal metasurface to that from plain gold film, the trend of which follows well that of photovoltage enhancement factor. This indicates that the PTE effect dominates photovoltage generation in sample 3, because the laser induced temperature rise – which drives the free electrons between regions with different thermoelectric powers – is directly proportional to the optical absorption of the structure. To better illustrate the uniformity of the fractal metasurface enhanced photodetector, we plot in Figure 3.6(c) the measured responsivity on fractal metasurface and unpatterned gold. As a result of significant wavelength-dependent optical absorption from gold, the responsivity of unpatterned gold photodetector displays widely variant responsivity across the visible spectrum – with responsivity at 476 nm nearly two *orders* of magnitude greater than that at 700 nm. However, with fractal metasurface, we achieved a rather flat responsivity spectrum, with the difference between highest and lowest responsivities less than a *factor* of two. With this observation, we claim to have realized uniform graphene photodetector using especially designed fractal metasurface.

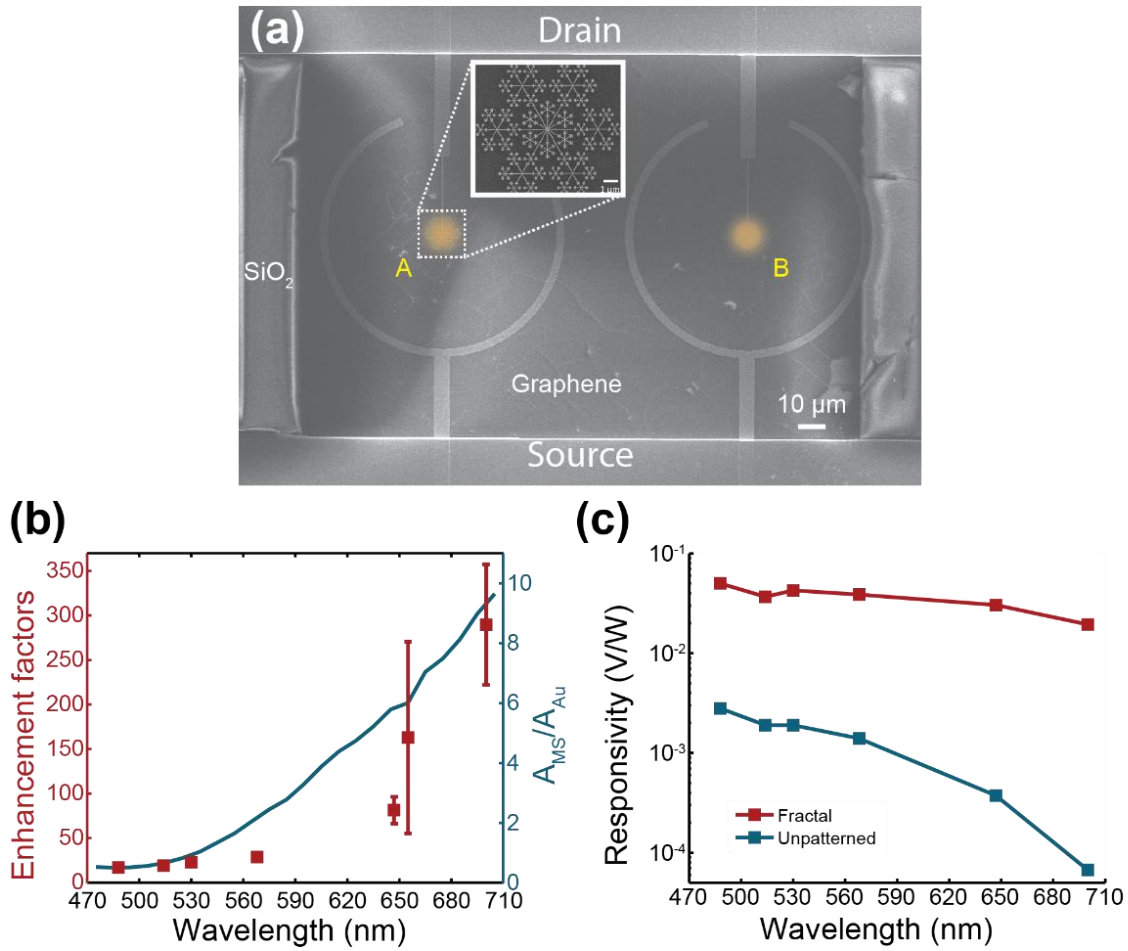

Figure 3.6 Fractal metasurface enhanced graphene photodetector on glass substrate

(a) SEM of the graphene photodetector sample 3 with the fractal metasurface (the white scale bar is 10 μm) encircled by 30 μm radius ring, and a compare device on the right where the fractal metasurface is replaced by a gold disk of similar size; inset image shows the zoomed-in view of gold fractal metasurface. Similar to sample 1 and 2, the ratio of the photovoltage generated on spot A to that generated on spot B is defined as the enhancement factor. (b) Measured photovoltage enhancement (red markers with error bars, left axis), and ratio of measured optical absorption from fractal metasurface to plain gold film (blue curve, right axis), from 476 nm to 700 nm. (c) Measured responsivity on fractal metasurface (spot A in (a), red markers) and on unpatterned gold disk (spot B in (a), blue markers), from at 6 tested wavelengths from 476 to 700 nm.

3.4 Conclusion

In conclusion, by reforming the source and drain contacts into a fractal metasurface and a ring encircling it, we demonstrated a broadband graphene photodetector exhibiting spectrally-uniform responsivity across the visible spectrum. The application of the fractal metasurface is not bound to graphene photodetectors but can also be integrated with PV/PTE photodetectors made of other photodetection materials[232]–[235]. The great flexibility of our fractal metasurface design

enables broadband enhancement at other portions of the electromagnetic spectrum[236] and for various spot sizes. Additionally, the photoresponse enhancement is insensitive to the incident light polarization, a quintessential feature of a practical photodetecting/photoharvesting system. These attributes, combined with dynamic tunability through source drain bias, make our fractal metasurface an advancement toward the incorporation of graphene into modern photodetecting and photoharvesting applications.

4. SPATIAL AND TEMPORAL NANOSCALE PLASMONIC HEATING QUANTIFIED BY THERMOREFLECTANCE

4.1 Introduction

Plasmonic systems open up the route to nanophotonics due to their unique abilities to confine electromagnetic energy down to ultra-small volumes[17], [19], [20] that enable nanometer-scale light manipulation[22], [237]–[239]. However, the intrinsic ohmic losses in plasmonic systems hinder their performance because a portion of the incident radiation energy is inevitably converted to heat[5], [46], [240]. On the other hand, such lossy nature of plasmonic systems makes them promising candidates for optical heaters, a key component in many modern-day technologies where optical-to-thermal energy conversion is needed, for instance photothermal therapy[241], [242], solar energy harvesting[4], [33], [243], [244], photocatalysis[3], [245], [246], nanoparticle manipulation[8], [247], [248], photodetectors[30], [73], [207], [249], etc. To date, the most commonly used techniques to characterize plasmonic heaters study the optically pumped plasmonic system via (i) thermal camera[250], (ii) temperature-dependent photoluminescence of thermographic phosphor (TGP) or nitrogen-vacancy (NV) center[251]–[253], (iii) temperature-dependent refractive index change of a surrounding medium[254], (iv) Raman scattering[255], [256], and (v) scanning thermal microscopy (SThM)[257], [258]. Those pioneering techniques have originally laid out the path for the visualization of plasmonic heating. However, each of them has its limitations. Thermal cameras cannot achieve spatial resolution smaller than ~2 μm due to the wavelength range used in imaging; TGP-, NV center-, and surrounding medium-based techniques generally have high temperature sensitivity, but require special sample treatment such as tagging the sample with TGP thin film, nanodiamonds, and immersing sample in a liquid, and depend heavily on phospor stablity that also limits the measurement temperature range. While the Raman scattering- and SThM-based techniques can resolve the heating of individual nanoparticles, they require slow scanning to produce a thermal image. Moreover, most of these approaches focus only on the (quasi) steady-state plasmonic heating, while the ultrafast heating dynamics remains

unresolved. Although the hot electron dynamics of plasmonic systems in the picosecond (ps) regime has been well investigated using pump-probe technique[259]–[261], a systematic study is lacking in the phonon-dominated nanosecond (ns) heat transfer regime for plasmonic heating. In this work, we characterize both the steady-state and transient plasmonic heating of nanodisk gap plasmon structures using two thermoreflectance techniques, optical thermoreflectance imaging (OTI) and time-domain thermoreflectance (TDTR), aiming to understand the heat generation and flow in a multilayer plasmonic structure. A brief summary of the two techniques and their functionalities is shown in Table 4.1. With OTI, we obtain the steady-state thermal image of a laser-irradiated plasmonic structure and its millisecond (ms)-scale plasmonic heating dynamics, without special treatment to the sample. Furthermore, the TDTR measurement and a detailed numerical model enable us to detect the ns-scale temperature decay dynamics (with ps resolution) of a multilayer plasmonic structure upon optical impulse excitation, and then extract the thermal interface conductance between the different layers of the structure with a specialized mathematical apparatus.

We organize the presentation of this work in the following manner. We begin with the Plasmonic Structure Design section that deals with the optical design, fabrication, and characterization of the gap plasmon nanostructures implemented as gold nanodisk arrays (NDAs). Then in the Optical Thermoreflectance Imaging section, we present our results on the steady-state thermal imaging of the optically-pumped NDA samples and show that the non-contact OTI method is capable of detecting 100 nm features in the thermal image. Full-field OTI is also used to study thermal temporal response in ms range taking into account the substrate and the heat sink. The Time-Domain Thermoreflectance Measurement section presents the results of the impulse responses of the NDAs studied both experimentally and numerically with ps resolution. In this section, we propose an augmented TDTR computational model with expanded applicability to plasmonic structures and quantify the relationship between temperature decay time constant and the disk radius in the NDA. The Conclusions section summarizes the overall results of the study. Finally, the Methods section provides more detailed technical information on the fabrication and thermoreflectance measurement techniques.

Table 4.1 Summary of the optical thermoreflectance imaging (OTI) and time-domain thermoreflectance (TDTR) techniques

Technique	*Thermal Imaging*	*Temporal Scale*	*Pump Source*	*Functionality and Applications*
OTI	☑	Up to 5 ms	825 nm CW laser	Visualize steady-state optical heating, resolve ms-scale transient heating
TDTR	☐	Up to 4 ns	780 nm pulsed laser	Characterize materials' thermal properties, resolve ns-scale transient heating

4.2 Plasmonic structure design

In this study, we choose gap-plasmon design of the plasmonic structure, for its relatively narrowband resonance and large on-resonance optical absorptance among all plasmonic structures[262]–[264], to facilitate the investigation of the optical resonance-dependent plasmonic heating. The designed structure consists of a 22-nm-thick gold (Au) nanodisk residing on a 20-nm-thick aluminium oxide (alumina, Al_2O_3) spacer layer and a 100-nm-thick Au reflector, as illustrated in Figure 4.1(a). The radii of the top Au nanodisk vary from 30 to 90 nm with a step of 10 nm across seven different NDAs, with each square array containing identical nanodisks, and all NDAs share a fixed periodicity (i.e., the distance between neighbouring nanodisk centres, $P_x = P_y$ = 300 nm in Figure 4.1(a)). All parameters except the disk radius are optimized via simulation to achieve the strongest optical absorptance on resonance, and are kept invariant across all NDAs to ensure only one variable (the disk radius) in the study. The difference in the disk radii across the individual arrays results in different optical absorptance spectra, as will be discussed in more details later in this section. Finally, the substrate supporting the gap plasmon structure is chosen to be 0.7-mm-thick float glass for its low thermal conductivity to minimize the heat sink effect, thus a high temperature profile can be achieved on the top surface of the gap plasmon structure. Figure 4.1(b) shows the scanning electron micrograph (SEM) of the fabricated Au nanodisks on Al_2O_3 and Au reflector layers. All seven NDAs of different radii were fabricated on the same substrate to facilitate measurements and diminish cross-sample variations in material properties and thicknesses. See Methods for more details on sample fabrication.

Optical measurement using a variable angle spectroscopic ellipsometer (J.A. Woollam, WVASE) with linearly polarized incident light is first carried out on the seven NDAs to characterize their reflectance (R) spectra. Since transmittance is prohibited by the optically thick

Au back reflector and scattering is negligible (reflectance is less than 0.07% for all non-specular angles at all wavelengths, verified independently with ellipsometer scatterometry measurement), we calculate the absorptance spectra as A = 1 – R and show them in Figure 4.1(c). For comparison, in the same figure, we plot the optical absorptance spectra calculated using the finite element method in the frequency domain with a commercial software solver (COMSOL Multiphysics, Wave Optics Module). In the simulation, each spectrum is obtained via averaging the spectra of radii within ±3 nm of a given disk radius, to account for the nanodisk size fluctuation in the fabricated NDAs. Since the smaller nanodisks demonstrate poorer shape- and dimension-uniformity, we attribute the more pronounced simulation-experiment discrepancies for smaller nanodisks to the imperfections of the fabricated sample. Moreover, due to stronger free electron scattering off the edges, the optical properties of smaller gold nanodisks experiences greater deviation from that of continuous film that is used in the simulations, which also leads to a greater discrepancy between simulation and measurement. Figure 4.1(d) clearly shows that on optical resonance, the electric field is tightly confined to the corners of the Au nanodisk at the Au/Al_2O_3 interface along the incident electric field direction, indicating that the free electrons in the Au nanodisk of certain radius are forced by the electromagnetic wave of a matched wavelength to oscillate across the nanodisk. The free electron movement (ohmic current) in the nanodisk then induces antiparallel free electron movement in the back reflector. In the Al_2O_3 dielectric spacer layer, two displacement currents arise due to the ohmic currents in the two metal layers, which together form a complete current loop between the nanodisk and back reflector (upper panel of Figure 4.1(d)), giving rise to a strongly localized magnetic field in the Al_2O_3 dielectric gap (lower panel of Figure 4.1(d)). Finally, the electron movement in the Au layers causes the electron temperature and subsequently lattice temperature to rise, manifesting itself as plasmonic heating on a macroscopic scale. The dielectric gap thickness is a critical parameter for the gap plasmon structure – when it is too thick, the induction of the displacement current loop becomes weak; when it is too thin, the dielectric gap does not provide adequate optical phase accumulation to induce anti-symmetric currents in the nanodisk and back reflector. Light at off-resonance wavelengths (i.e., when the radius-wavelength matching condition is not met) “feels” the presence of the top Au nanodisk to a lesser degree, and a relatively higher portion of the incident power is reflected back to the free space, instead of causing free electron oscillations in the metal layers.

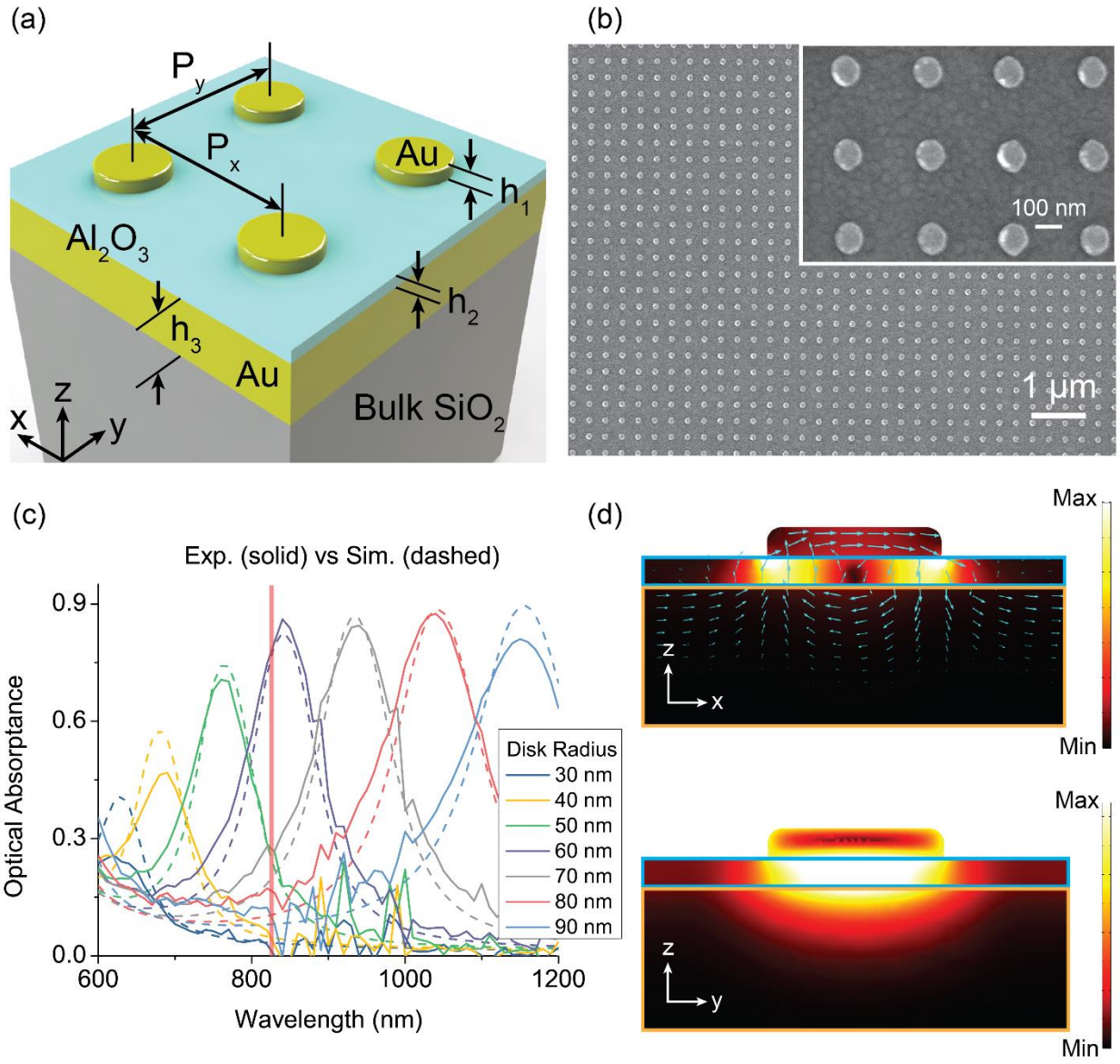

Figure 4.1 Plasmonic system design for thermoreflectance characterization

(a) Schematic of the gap plasmon structure – the gold (Au) nanodisk array (NDA). The Au nanodisks have a thickness h_1 = 22 nm, arranged with periodicity $P_x = P_y$ = 300 nm, residing on an Al_2O_3 layer with thickness h_2 = 20 nm atop an Au back reflector layer with thickness h_3 = 100 nm. The disk radius varies across NDAs, and all the arrays are deposited on a 0.7-mm-thick bulk SiO_2 substrate. (b) Scanning electron micrograph (SEM) of the fabricated NDA on Al_2O_3 and Au layers. Scale bar: 1 μm. Inset: zoomed-in view of the NDA showing a few nanodisks. Scale bar: 100 nm. The nanodisks in both images have a designated radius of 60 nm. (c) Measured (solid lines) and simulated (dashed lines) optical absorptance spectra of the NDAs with disk radii ranging from 30 to 90 nm. The red vertical line indicates the wavelength of the continuous-wave (CW) pump laser used in optical thermoreflectance imaging. (d) Simulated electric (upper panel) and magnetic (lower panel) field amplitudes at two orthogonal planes when the NDA is under resonant excitation (60 nm radius nanodisk under 840 nm incident light). The incident light is linearly polarized along the *x*-direction. Blue arrows in the upper panel denote the amplitude of displacement current density. The blue- and yellow-outlined regions indicate the 20-nm-thick Al_2O_3 and 100-nm-thick Au reflector layers, respectively, the bulk SiO_2 substrate is not shown.

4.3 Optical thermoreflectance imaging

The conventional thermoreflectance imaging technique relies on the temperature-dependent surface reflectivity of materials to obtain temperature information of the heated sample, and has been initially employed to inspect electrical self-heating in microelectronics[265], [266]. Specially modified thermoreflectance imaging setups incorporate a pump light source to replace the conventional electrical source for sample heating (hence the name optical thermoreflectance imaging, OTI) and have been used to characterize the optical heating of active photonic crystals[267], heat diffusion in anisotropic materials[268], and light-induced dewetting of thin metal films[269]. In our OTI setup (see Figure 4.2(a)), an 825 nm continuous-wave (CW) pump laser is temporally modulated into 2.5 ms square pulses with 10% duty cycle, then focused by a 100× objective lens to a diameter of ~1 μm and incident on the sample under investigation. A portion of this pump laser power is absorbed by the plasmonic structure and dissipates as heat, causing the local temperature to change at a rate determined by the modulation frequency. The probe light is a loosely-focused 530 nm light emitting diode (LED) pulse that covers an area larger than the NDAs, with a duration of 250 μs and a computer-controlled arrival delay τ with respect to the pump pulse start time. Each OTI cycle is completed with one pump pulse and one probe pulse, and the cycles are categorized into active and passive image cycles. As shown in Figure 4.2(b), in an active (passive) image cycle, the probe pulse arrives when the sample is sufficiently heated (cooled). A charge-coupled device (CCD) camera detects the change in the reflected probe light intensity ΔR between the two cycles on each image pixel. The measured ΔR, combined with the pre-calibrated thermoreflectance coefficient (see Supplementary Information), can be used to calculate the temperature rise caused by the pump laser on each pixel, hence allows one to map the temperature distribution of the optically pumped plasmonic structure. Since the probe LED has an intensity much smaller than the tightly focused pump laser, its plasmonic heating effect can be neglected. Figure 4.2(c) presents a thermal image obtained with OTI on an NDA with 60 nm disk radius. In order to examine the correlation between plasmonic heating and optical absorptance, we carry out OTI measurement with 825 nm pump laser on all seven NDAs with different disk radii thus varying optical absorptance at 825 nm (see intersection points of the red vertical line with different curves in Figure 4.1(c)). In Figure 4.2(d) we plot the measured peak temperature rise and the measured optical absorptance versus disk radius, which shows an excellent correlation between the two.

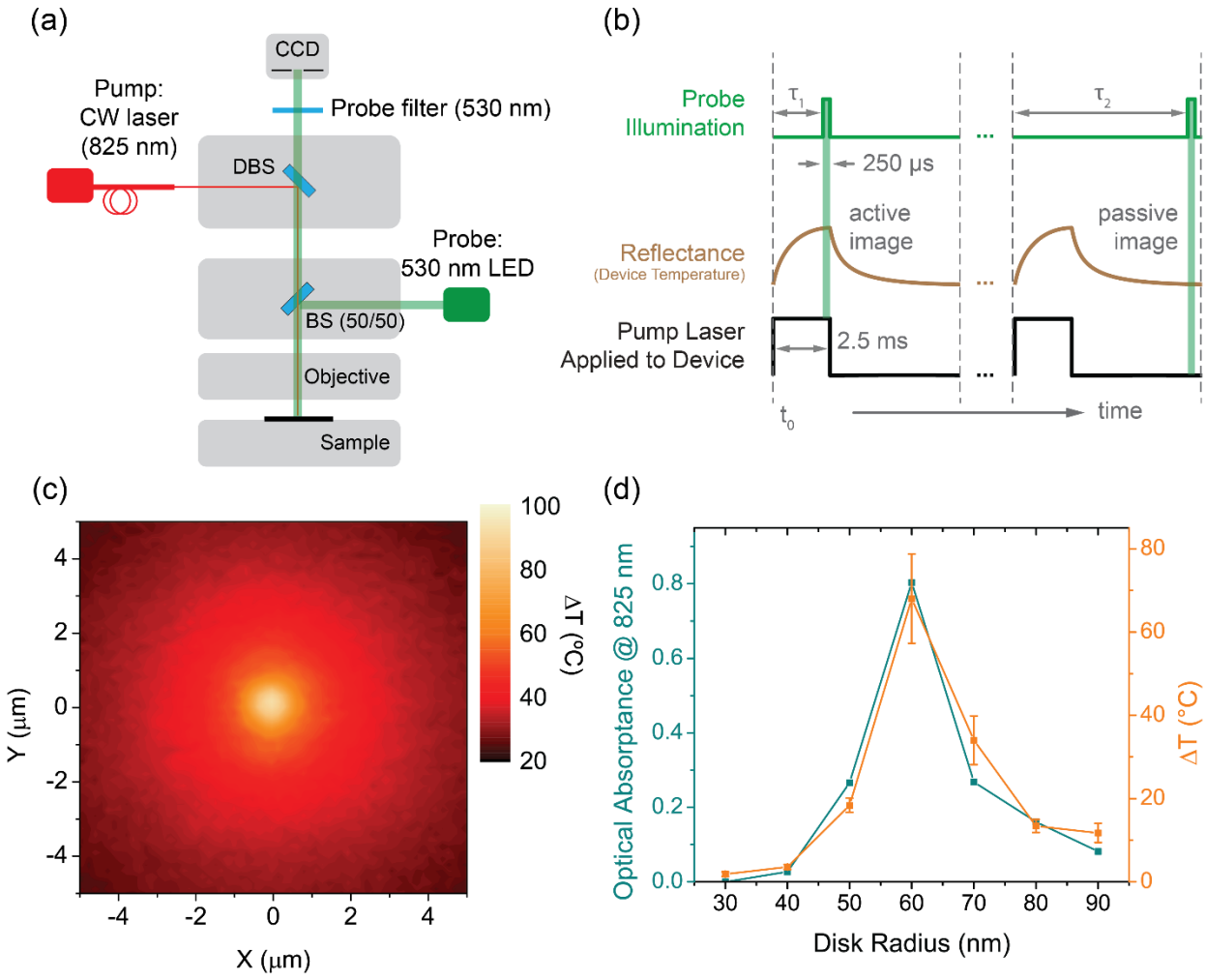

Figure 4.2 Optical thermoreflectance imaging measurement

(a) Schematic of the optical thermoreflectance imaging (OTI) setup. A tightly focused 825 nm continuous-wave (CW) laser is used as the pump laser, and a loosely-focused 530 nm light emitting diode (LED) is used as the probe light. A charge-coupled device (CCD) camera detects the intensity of the reflected 530 nm light. DBS: dichroic beam splitter, which reflects the 825 nm laser and allows the 530 nm LED light to transmit. BS: beam splitter.(b) The OTI cycles are divided into active image cycles and passive image cycles. During each cycle, the CW pump laser is modulated into 2.5 ms square pulses with a duty cycle of 10% (lower row), to induce surface reflectivity change on the sample (middle row). A 250 μs probe pulse is sent to the sample at a delay of τ_1 (τ_2) with respect to the start of pump pulse in active (passive) image cycle (upper row), and the CCD camera detects the difference between the reflected intensity of the two cycles to obtain ΔR. (c) Thermal image obtained via OTI on an NDA with disk radius of 60 nm. The pump laser has a wavelength of 825 nm, an incident power of 10 mW, and a focused spot diameter of 1 μm. (d) Measured optical absorptance at 825 nm (left vertical axis, green curve) and measured peak temperature rise (right vertical axis, orange curve) versus disk radius. The green curve is obtained by reading the intersecting points between the red vertical line and the absorptance curves in Figure 1(c). The yellow curve is obtained from the OTI measurements, where the square markers represent the average temperature rise of 100 thermal image pixels in an area centered on the pump laser, and the error bars represent the standard deviation of temperature rise on the same thermal image pixels.

By manipulating the arrival time delay of the active image probe pulse with respect to the pump laser start time (τ_1 in Figure 4.2(b)), while keeping the passive image pulse arrival at sufficiently long delay (i.e. when sample cools to equilibrium), we obtain the dynamic temperature evolution of three optically pumped NDAs and present the results in Figure 4.3(a). It can be concluded that the temperature rise largely varies across NDAs and can be significantly higher than the bare substrate (i.e., areas containing no nanodisks but only Al_2O_3 and Au reflector layers). Also, the surface temperature reaches equilibrium within 2.5 ms after the pump pulse starts heating the sample, and the temperature accumulation between pump pulses is negligible at the chosen pump pulse duration and duty cycle. We note that although not shown in this work, the OTI setup is capable of achieving 50 ns temporal resolution with proper modification to the electronics[270]. The OTI is an optical imaging method and is bounded by the diffraction limit. Therefore the temperature rise on individual nanodisks cannot be resolved (see Supplementary Figure 4.7). Instead, the OTI-produced thermal map represents the temperature rise averaged between neighboring nanodisks and their surroundings, in other words, the measured temperature rise profile smears out the actual temperature rise on individual nanodisks because of the collective effect. Moreover, the continuous Au layer underneath the Al_2O_3 layer also contributes to the homogenization of thermal distribution. In order to test the OTI's performance on *isolated* features with sizes on the order of 100 nm, we fabricate a separate nanodisk gap plasmon sample where a 100-nm-wide gap is intentionally created in the back reflector (inset of Figure 4.3(b)), and align the center of pump laser to the center of the gap in OTI measurement (see Supplementary Information for fabrication and OTI characterization methods for this sample). As shown in Figure 4.3(b), a line at the position of the gap is clearly visible in the thermal image, indicating that isolated features as small as 100 nm can be well detected by the OTI method. It is to be noted, however, that the line's clear contrast with its surroundings represents not a temperature discontinuity, but rather a difference in the thermoreflectance coefficient on these pixels from their surroundings (the thermal image is obtained using a uniform thermoreflectance coefficient for all image pixels). In reality, the temperature is continuous and heat can be spread across the gap via the substrate. We also note that the 100-nm-wide line appears to be blurred and wider in the thermal image because of the diffraction limit.

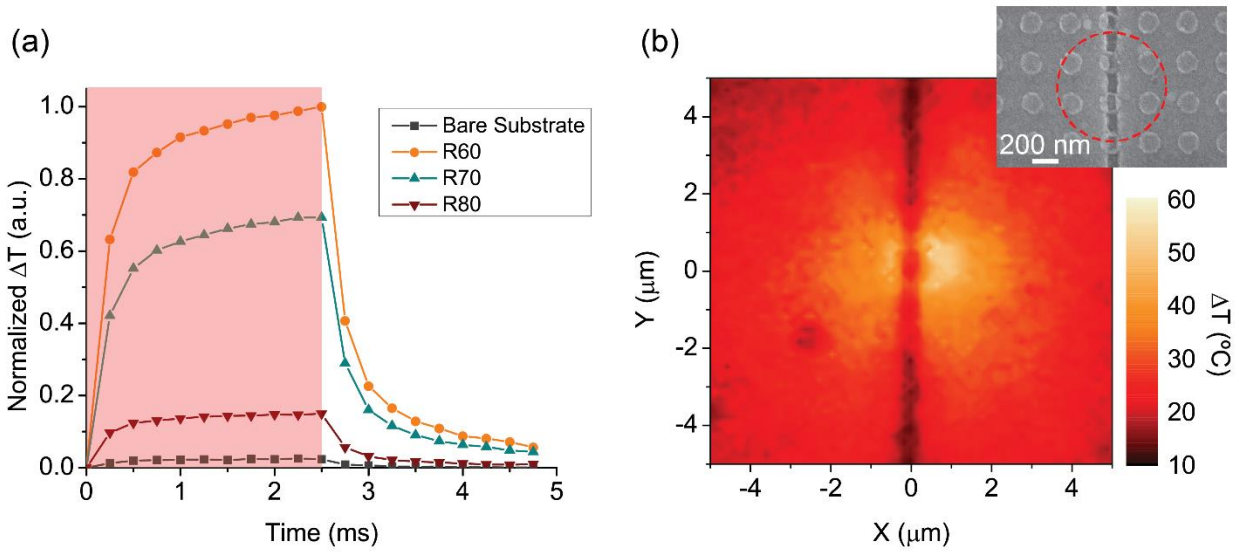

Figure 4.3 Detecting temporal and spatial variances with OTI

(a) Normalized temperature evolution measured on three different NDAs (with radii of 60, 70, and 80 nm, respectively) and a bare substrate. The red-shaded region indicates the time when the pump laser is turned on, and non-shaded region when it is off. (b) Thermal image of an NDA sample with an intentionally-created 100 nm-wide gap. Inset: SEM of the sample. The thermal image is obtained with the pump laser illuminating the center of the gap, as indicated by the red dashed circle in the SEM.

4.4 Time-domain thermoreflectance measurement

As a member of the thermoreflectance family, TDTR measurement is widely used to characterize the thin film thermal conductivity and the thermal interface conductance between layers of different materials[271]–[275]. In TDTR measurement, a temporally modulated pump pulse creates transient heating on the sample surface, and a probe pulse that has high spatial overlap with the pump pulse characterizes the change of the thermoreflectance reflectivity. A mechanical delay stage can control the time delay between pump and probe pulse arrivals, granting one with the ability to obtain the dynamics of temperature evolution up to a few ns with ps resolution. TDTR differs from OTI in that no CCD camera is used for the probe beam, therefore it is not a spatially-resolved thermal imaging technique. We carry out TDTR measurement on the same NDAs described previously, using a pulsed laser of 780 nm central wavelength, a repetition rate of f_{rep} = 76 MHz, and a pump modulation frequency f = 0.8 MHz. Details of our TDTR measurement can be found in the Supplementary Information.

The result of the TDTR measurement is usually presented as the ratio between the in-phase and out-of-phase components of the lock-in voltage ($-V_{in}/V_{out}$) versus pump-probe delay time, due to its robustness against fluctuations (change in pump and probe beam power, focus, and overlap, etc.) in the measurement[275]. Our measured $-V_{in}/V_{out}$ from 0.1 to 4 ns on the seven NDAs is presented in Figure 4.4(a). Evidently, the ratio curves for different NDAs do not coincide. One's intuition might attribute this to the different optical absorptances of the pump laser thus different heating powers for different disk radii. However, as pointed earlier in this section, the measured $-V_{in}/V_{out}$ curves are immune to incident power variation (i.e., when only the pump power is changed, the $-V_{in}/V_{out}$ curve remains unchanged because both V_{in} and V_{out} are affected by the incident power by the same factor). Hence, the deviation of the curves implies more subtle information about the temperature decay dynamics owing to the plasmonic effect, which is investigated next.

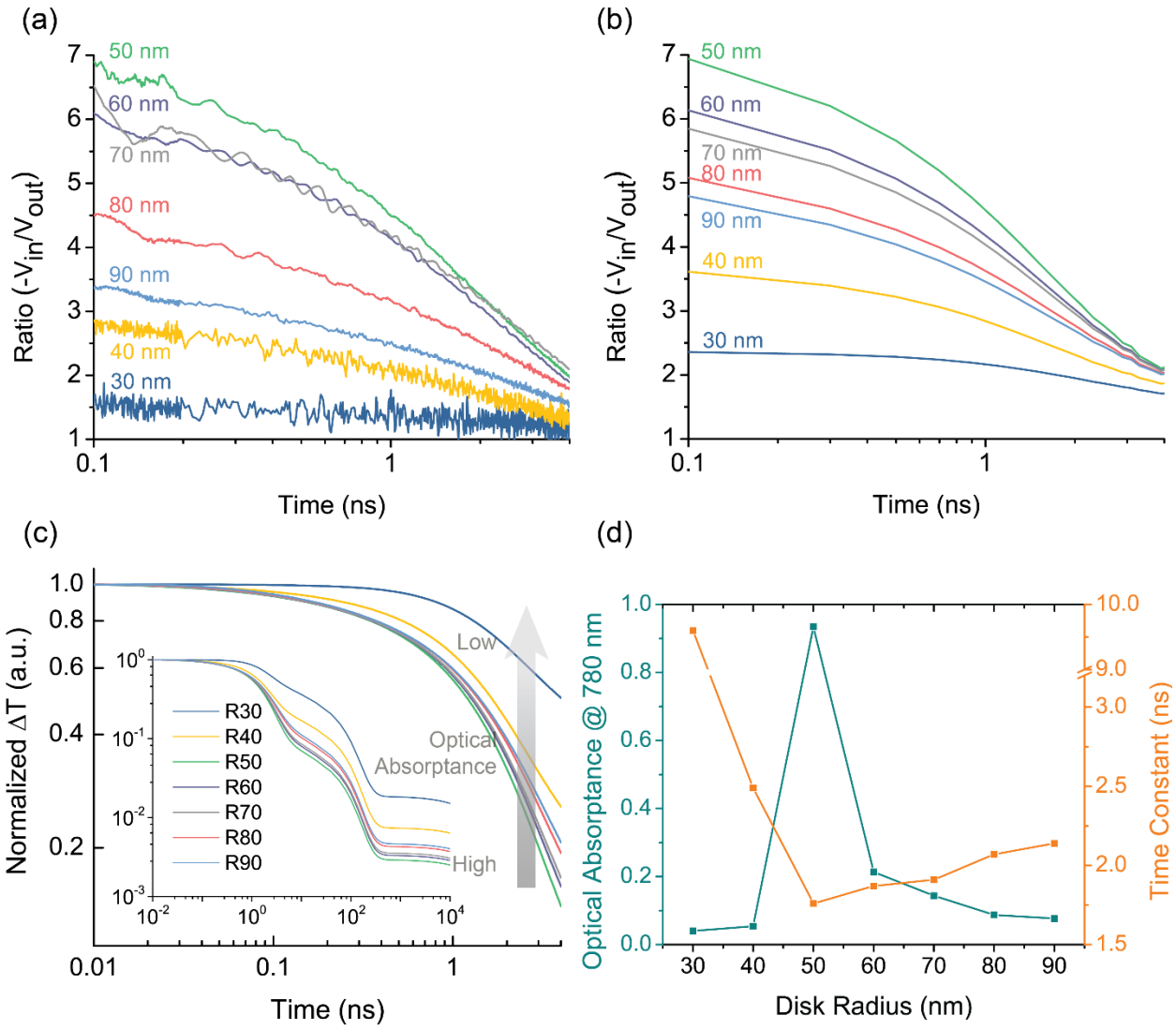

Figure 4.4 Time-domain thermoreflectance measurement and simulation

Semi-log plot of measured (a) and simulated (b) ratio between in-phase and out-of-phase components of lock-in detected time-domain thermoreflectance (TDTR) voltage as a function of pump-probe delay time, on the same NDAs as presented in Figures. 1(c) and 2(d). (c), Impulse responses of seven different disk radii extracted from numerical simulations, normalized to their *respective* maximum temperature rise values. Inset, same data presented in a much broader time window, with the time values on the horizontal axis displayed in ns. The translucent grey arrow indicates that the optical absorptance decreases from lowest to highest curve. (d), The simulated optical absorptance of 780 nm light (green curve, left vertical axis), and the simulated impulse response time constant (yellow curve, right vertical axis) versus disk radius. The time constant is retrieved from c as the time at which the temperature decays to 1/*e* of its initial value for each disk radius. For clarity of display, the time constant axis is broken between 3.2 and 9 ns.

Because of the pulse cumulative effect, the measured ratio $-V_{in}/V_{out}$ is related to the impulse response of the system in a rather convoluted way[274], [276]. However, the conventional TDTR analytical models are inadequate to predict the experiment and guide the device design for

plasmonic systems because they assume no optical resonance effect. In order to unveil the reason for the measured ratio curve deviation, we perform three-dimensional numerical simulation using the finite-element method (FEM) with a commercial software solver (COMSOL Multiphysics, Wave Optics and Heat Transfer Modules) to retrieve the temporal responses of the NDAs under 780 nm light impulse excitation (i.e. their impulse responses) and apply them to the expression proposed in ref[277] to reproduce the experimental ratio data.

Since the TDTR laser spot size (~10 μm in diameter) is much smaller than the ellipsometer beam size (~500 μm in diameter), the nanodisk sizes are more uniform in the TDTR measurement. Hence, in contrast to the OTI simulations depicted in Figure 4.1(c), the simulations for TDTR use no spectral averaging, but each simulation is done with a single radius within ±3 nm of the designated radius to achieve best fitting with experiment. It is to be noted that in both our experiment and simulation, the presented data illustrate the dynamics of the temperature averaged between the outer surface of the Au nanodisks and the exposed Al_2O_3 surface. In our simulations, the Au/Al_2O_3 interface conductance and bulk SiO_2 substrate thermal conductivity are used as fitting parameters, and all other thermal parameters are taken from the literature, no disk radius-dependent effective thermal parameter is used. As pointed out in ref[278], unlike materials with a fine crystalline structure, float glass (amorphous SiO_2) does not exhibit heater size-dependent thermal conductivity, therefore in our simulations, the substrate SiO_2 thermal conductivity is kept constant across all disk radii. We achieve the best fitting with Au/Al_2O_3 interface conductance of 60 MW/m^2·K. When all the thermal parameters are fixed (see Supplementary Figure 4.11(b)), and only the disk radius (thereby heat source intensity and distribution) is varied in the simulations, good agreements with experiments can be achieved as shown in Figures 4.4(a) and 4.4(b). The fitting is exceptionally good for the 3 highest absorbing disk radii (50, 60, and 70 nm, see Supplementary Figure 4.11(c)), and we attribute the difference between simulation and experiment for other radii to their relatively weak optical absorptance, so that any small deviation from ideality in experiments will cause amplified simulation-experiment discrepancy for these radii. The excellent fitting grants us confidence about our numerical model. We then extract the impulse responses from our numerical models and show them in Supplementary Figure 4.11(d). Expectedly, the maximum temperature rise across different disk radii follows the trend of optical absorptance at the laser pulses' central wavelength. In Figure 4.4(c), we normalize the impulse responses of all seven disk radii to their respective maximum values, from which it can be concluded that the more

optically absorptive a gap plasmon structure is, the faster its surface temperature decays when it is subject to a laser impulse. From Figure 4.4(c), we extract the temperature decay time constants of the seven disk radii and plot them in Figure 4.4(d) together with their optical absorptance at the pulsed laser's central wavelength. Interestingly, the temperature decay time constants are inversely correlated with the structures' optical absorptance, a result stemming from the interplay between the plasmonic and thermal diffusion effects – when the disk radius is changing, not only the heat source (i.e. absorbed electromagnetic power) area but also the heat source spatial distribution varies (see Supplementary Figure 4.10). Both effects influence the outer surface temperature decay dynamics, and their co-existence leads to the non-monotonic time constant evolution versus disk radius. Such information is crucial for designing ultrafast plasmonic modulators, bolometers, and thermoelectric detectors.

Previously, similar work has been carried out on hot electron dynamics up to a few ps in gap plasmons structures[259], [260]. In our work, we study the heating transient behavior within a longer time scale which allows deeper heat penetration, therefore enabling us to retrieve both the impulse response and the thermal interface conductance between layers. It is worth pointing out that the significant discrepancy in temperature decay time constants presented in Figure 4.3(a) and Figure 4.4(c) results from the heating of bulk substrate: in Figure 4.3(a), the pump laser heats the sample long enough for the heat to penetrate the bulk substrate, so that when heating stops, the surface temperature decay shows the thermal time constant to the heat sink; whereas in Figure 4.4(c), the laser impulse does not have enough time to heat the bulk substrate, and one characterizes the ultrafast heat dissipation in a region on the order of a few microns near the heat source.

4.5 Conclusions

Using two distinct thermoreflectance techniques – optical thermoreflectance imaging (OTI) and time-domain thermoreflectance (TDTR) – we carry out a comprehensive study of plasmonic heating in both spatial and temporal domains. The OTI method empowers us to characterize the steady-state, and transient plasmonic heating on *millisecond* scales. With OTI, we map the absolute temperature distribution of an optically pumped plasmonic system, and successfully reveal the correlation between optical absorptance and peak temperature rise in plasmonic structures. Additionally, the developed OTI setup is capable of detecting 100 nm features, outperforming most existing thermal imaging techniques. With proper manipulation of probe pulses, the OTI can

be used to study the dynamic temperature evolution with 50 ns temporal resolution. The resonance-dependent *nanosecond*-scale impulse response of the plasmonic system is studied for the first time by the TDTR measurement with picosecond resolution and a newly-developed computational model. Backed by the robust TDTR experiment, the model enables us to retrieve the interface conductance between Au and Al_2O_3 layers to be 60 $MW/m^2 \cdot K$, and it uncovers the quantitative details of how the temperature decay time constant varies when the disk radius is changing. The inverse correlation between optical absorptance and temperature decay time constant is a result of the heat flow affected by both the spatial distribution of the absorbed energy and the heat source (i.e. nanodisk) area. This correlation highlights the crucial role of thin film and the thermal resistance of material interfaces in nanoscale heat transfer. Our findings provide a thorough understanding of plasmonic heating and have profound implications in thermoplasmonic and photonic devices and systems requiring ultrafast plasmonic modulation or enhancement.

4.6 Supplementary information

4.6.1 Ellipsometry characterization of Au dispersion

During fabrication, we grew Au and Al_2O_3 thin films on dummy samples under the same conditions as the nanodisk gap plasmon sample, and used the dummy samples to characterize the refractive indices of the thin films using an optical ellipsometer (J.A. Woollam, WVASE). The measured refractive indices for Au and Al_2O_3 are presented in Figure 4.5. We use these data for our Wave Optics simulation with COMSOL Multiphysics. The simulation results are presented in Figure 4.1(c) of the main text, Figure 4.10 and Figure 4.11(a) of the Supplementary Information.

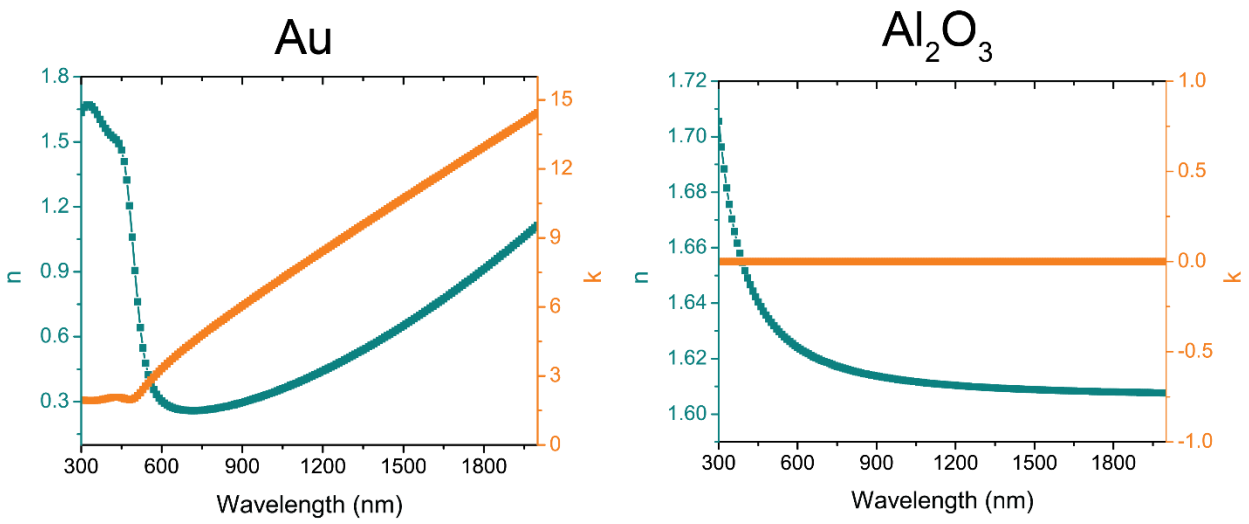

Figure 4.5 Measured real (n) and imaginary (k) parts of Au (left) and Al_2O_3 (right) refractive indices

4.6.2 C_{th} calibration

The thermoreflectance coefficient C_{th} is defined as the ratio of change in material reflectivity to the change in temperature that causes the former: C_{th} (K^{-1}) = $\Delta R/\Delta T$, and is used to determine the absolute value of temperature change due to plasmonic heating in the optical thermoreflectance imaging (OTI) step. The C_{th} value is calibrated using a setup separate from the OTI setup, which consists of a heating stage, a thermocouple, a motorized xyz stage, a 530 nm probe light emitting diode (LED) light, and a customized software to automate the process (see Figure 4.6(a)). To begin the calibration process, the user places the device under test (DUT) on the heating stage and under an optical microscope. The system then triggers the probe LED light and a charge-coupled device (CCD) camera records the reflectivity of all image pixels before sample is heated. Subsequently, the DUT is heated by the thermoelectric stage, with the thermocouple in contact with the DUT measuring the actual temperature on the DUT surface. Meanwhile the autoalignment software controls the xyz stage to compensate for the movement caused by thermal expansion to keep the reference point (a defect in Figure 4.6(b)) in focus, which is an item selected by the user on the DUT with preferably large optical contrast with its surroundings. Once temperature stabilizes at the preset value and vibration requirement is met, the probe LED light is triggered again for the CCD camera to record the reflectivity of all image pixels at elevated temperature. The ΔR obtained by probe LED and CCD camera, and the ΔT obtained by

thermocouple, are used to calculate C_{th} on each image pixel using C_{th} (K^{-1}) = $\Delta R/\Delta T$. The C_{th} calibration is a much slower process than the OTI, and multiple runs are usually carried out to obtain C_{th} with higher accuracy. C_{th} values at different regions of the DUT surface can be determined simultaneously (see Figure 4.6(c)). In our experiment, the C_{th} values for different disk radii are individually calibrated to obtain the temperature rise presented in Figure 4.2(d) in the main text.

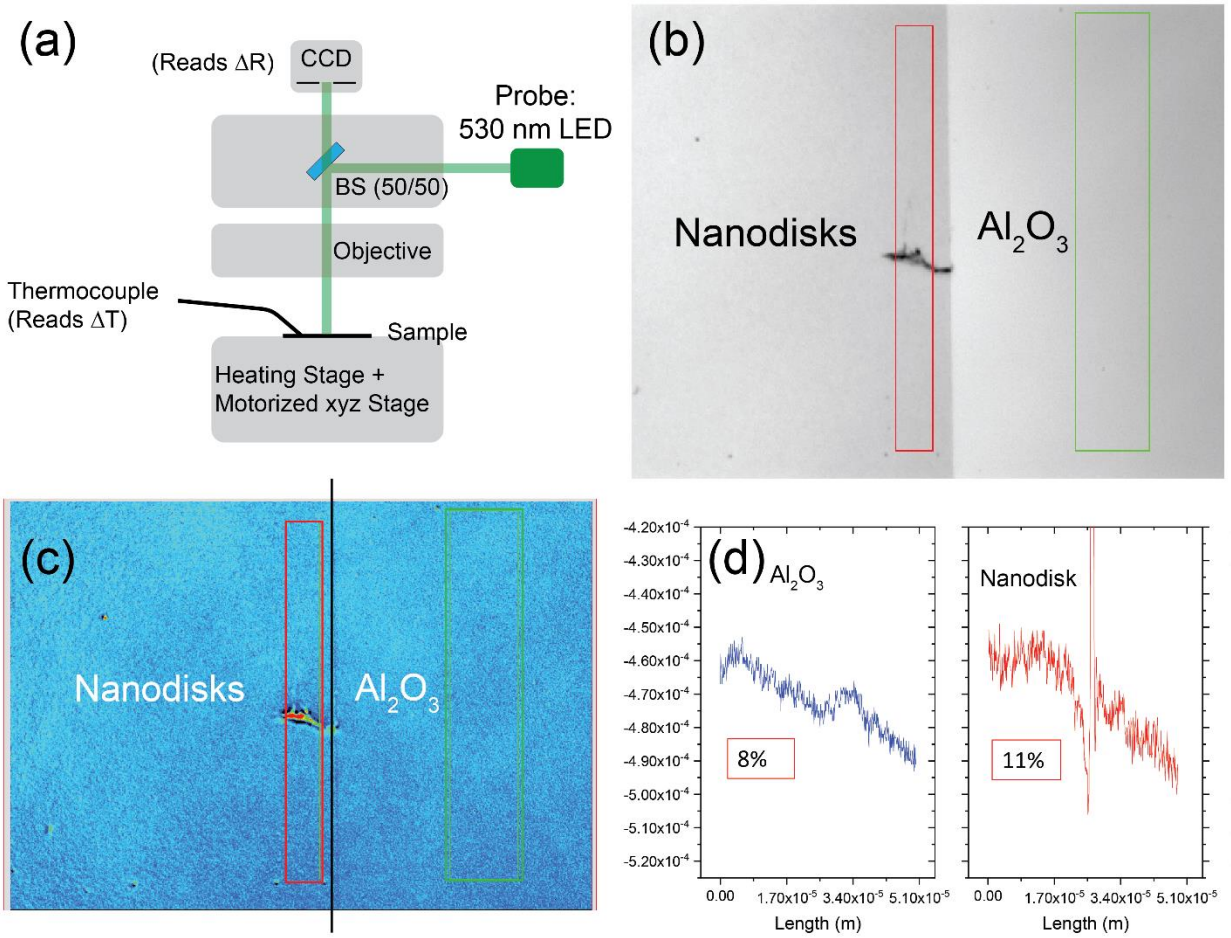

Figure 4.6 C_{th} calibration

(a) Schematic of C_{th} calibration setup. BS: beam splitter. (b) Optical image captured by the charge-coupled device (CCD) camera of an area of the nanodisk on Al_2O_3/Au used for C_{th} calibration. The black particle in the center of the image is a defect from fabrication, and is used in the C_{th} calibration setup as the focusing reference due to its large optical contrast with surroundings. (c) C_{th} calibration result, red colors denote high values and blue colors denote low values of C_{th}. The vertical black line marks the boundary between nanodisk array and exposed Al_2O_3 region. (d) C_{th} values taken from the green (left, Al_2O_3 region) and red (right, nanodisk region) boxes in (b) and (c). The 8% and 11% indicate the differences between left-most and right-most values within this range, which result from the slight tilt of sample during calibration, and the large fluctuation in the nanodisk data is from the defect.

Table 4.2 The calibrated C_{th} values for each disk radius

Radius/nm	30	40	50	60	70	80	90
C_{th}/K^{-1}	-3.33±0.10 × 1E-4	-4.07±0.16 × 1E-4	-3.85±0.09 × 1E-4	-4.12±0.28 × 1E-4	-3.67±0.31 × 1E-4	-3.89±0.29 × 1E-4	-3.71±0.25 × 1E-4

4.6.3 Temperature rise on individual nanodisks

During our OTI measurement on the nanodisks with strongest optical absorptance, we observe with scanning electron microscopy (SEM) that the nanodisks at the center of the pump laser beam can be dewetted, as shown in Figure 4.7. The pump laser has an output power of ~10 mW and focused to a spot of ~1 μm diameter, and the sample is subject to 120 s heating (considering the pump laser is modulated into 10% duty cycle pulses, the actual heating time is 120 s × 10% = 12 s). The two images shown at the left of Figure 4.7 are the thermal images overlaid on optical images taken from OTI measurement, they show the two different locations where the OTI measurements were taken. The bright spots indicate the center of the pump laser beam. We note that the negative temperatures shown on the color bar are measurement artefacts caused by defocusing of the probe beam, which usually happen at regions with non-uniform surface height. The middle SEM image shows the zoomed-in view of the measurement region. It is worth pointing out that the dark rectangles in this SEM image are not due to laser heating, they result from the carbon deposition by the SEM filament after a high magnification SEM image is taken. When we zoom in further at the marked locations, we observe the dewetting of the nanodisk as shown in the two right images. The fact that Au nanodisks are dewetted indicates that the local temperature around the nanodisks has reached several hundred degrees[269], [279], however, the OTI could not capture such high temperatures because the dewetted areas are smaller than the diffraction limit of our OTI setup, so only the average temperature rise is measured in a region on the order of diffraction limit (250-300nm). These images on the other hand illustrate the capability of our nanodisk gap plasmon structure to absorb light and convert it to heat.

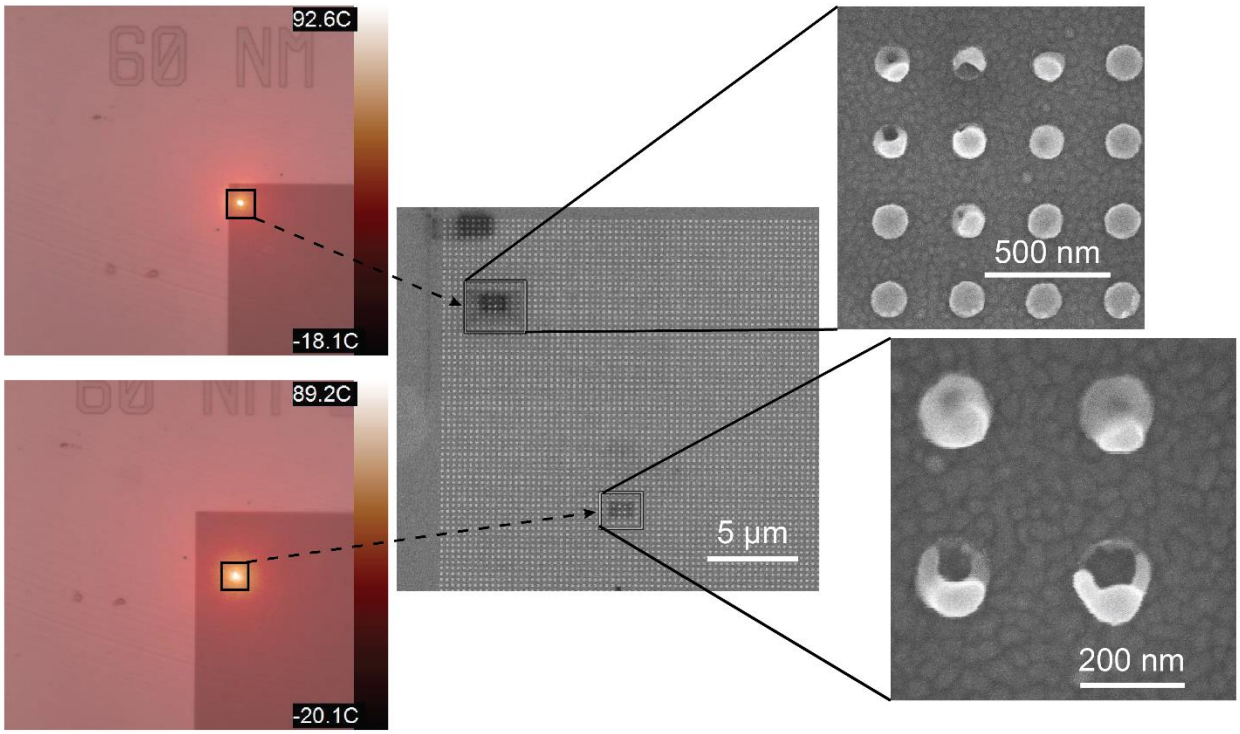

Figure 4.7 Nanodisks dewetted by pump laser

The nanodisks have a radius of 60 nm, and are subject to 825 nm pump laser illumination for 120 s. Nanodisk detwetting is observed at the center of the pump laser beam.

4.6.4 Fabrication and characterization of NDA with 100 nm-wide gap in back reflector

Other than having a 100 nm-wide gap in the back reflector, the sample presented in Figure 4.3(b) of the main text differs from other NDAs in that the Au reflector and nanodisks are replaced by aluminum (Al) counterparts, and the dielectric gap and supporting substrate are still Al_2O_3 and float glass, respectively. Note that *only* the results shown in Figure 4.3(b) of the main text are obtained from the Al NDAs; all other results are from Au NDAs. Besides showcasing the OTI's performance in imaging sub-diffraction limited features (e.g. a 100 nm-wide gap), this sample also allows us to present the OTI's capability to characterize gap plasmon structures composed of a material other than Au.

Two 30 µm × 30 µm × 100 nm (length × width × thickness) Al pads with a separation gap of 100 nm were first fabricated on the bulk float glass substrate via electron beam lithography (EBL), metallization and lift-off. 20 nm Al_2O_3 was subsequently grown on the Al pads using atomic layer deposition (ALD), and finally, the Al nanodisks with a radius of 80 nm were placed

on top of the Al_2O_3 via EBL, metallization, and lift-off. Since the float glass substrate is electrically insulating, during the two EBL steps, a 5 nm chromium (Cr) layer was deposited on top of the EBL resist as a charge dissipation layer and was removed with Cr etchant before the resist development stage. This step somewhat compromised the quality of the fabricated sample and resulted in increased edge roughness on the Al nanodisks compared to Au NDAs (in fabricating the Au NDA sample, the Cr layer was not necessary because the universal Au back reflector layer served the role of charge dissipation layer, whereas it was necessary for the Al NDA because the Al reflector was defined into isolated pads and not universal across the entire sample).

Since Al film and Al NDAs have stronger optical absorption and temperature-dependence of reflectivity in the near-IR, in both OTI and C_{th} calibration of the Al NDA, the probing LED wavelength was changed from 530 nm to 780 nm. The C_{th} value of this Al NDA sample was calibrated to be -3.42±0.18E-4 K^{-1} and was used to obtain the thermal image with absolute ΔT in Figure 4.3(b) of the main text.

4.6.5 Time-domain thermoreflectance measurement setup

Our time-domain thermoreflectance (TDTR) setup uses a 780 nm central wavelength Ti:Sapphire pulsed laser with 150 fs pulse duration and 76 MHz repetition rate, which is split into pump and probe pulses. The pump pulse is modulated at 0.8 MHz by an electro-optic modulator (EOM) and loosely focused by a 10× objective lens to ~10 μm diameter on the sample, with the time delay between pump and probe pulses controlled by a motorized stage. The modulated ΔR information is extracted by the probe pulse via a lock-in amplifier synchronized to the 0.8 MHz modulation frequency. The TDTR setup is depicted in Figure 4.8, and the measured in-phase and out-of-phase voltage signals are presented in Figure 4.9.

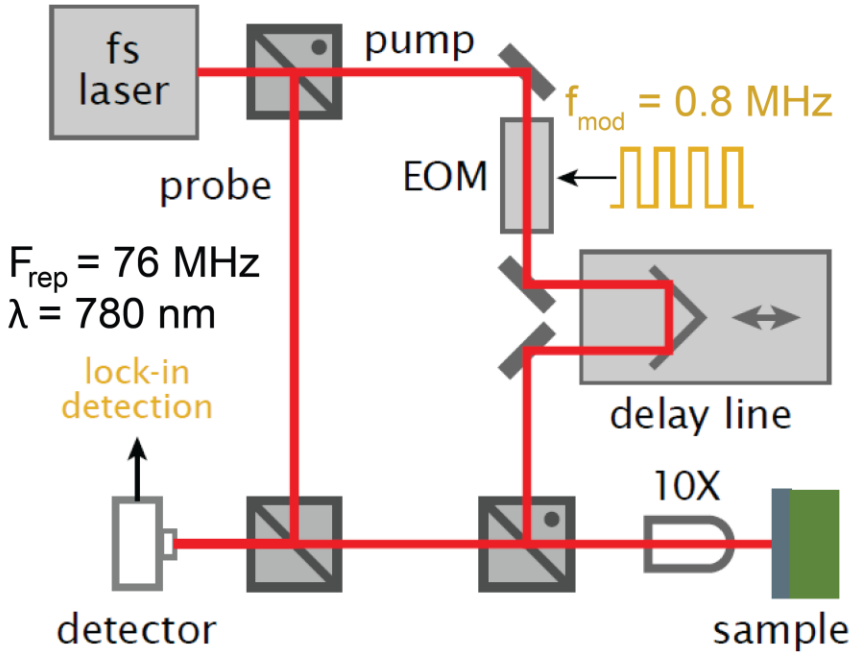

Figure 4.8 Schematic of time-domain thermoreflectance measurement

EOM: electro-optic modulator.

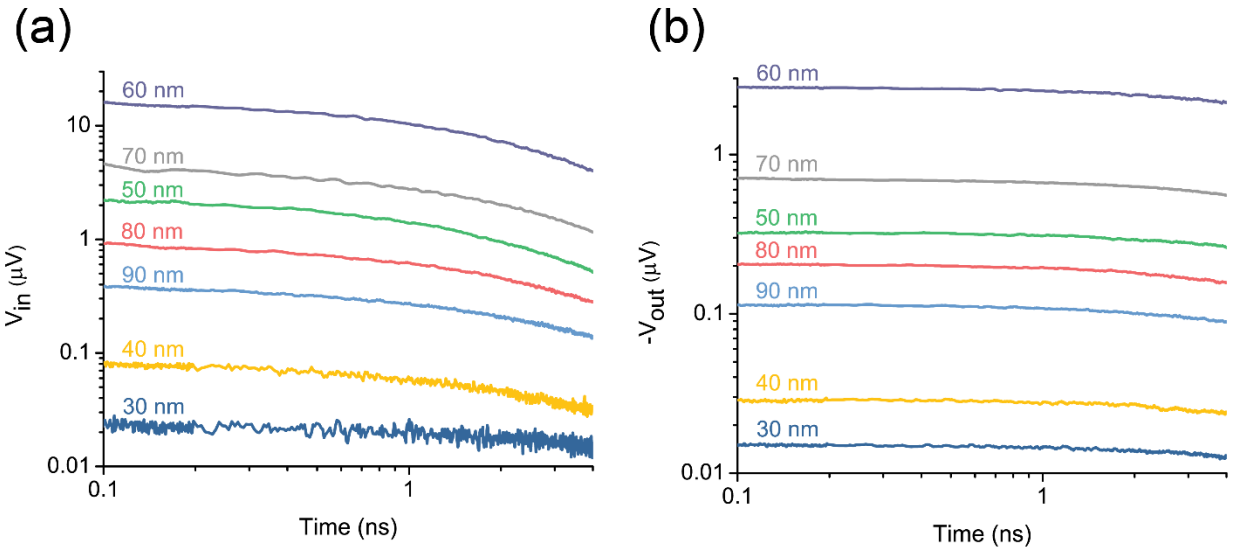

Figure 4.9 Measured in-phase (a) and out-of-phase (b) TDTR signals on Au NDAs with different disk radii.

4.6.6 Calculation of $-V_{in}/V_{out}$

We first use a finite element method (FEM) Wave Optics model to calculate the 3-dimensional distribution of dissipated power under 780 nm linearly polarized light illumination, and show the results in Figure 4.10. The dissipated power stems from the free electron oscillation in metals, therefore it is zero in the dielectric Al_2O_3 layer. This calculation is done in one unit cell, with periodic boundary conditions used on vertical sidewalls. In the Wave Optics simulation, the disk radii are slightly modified according to the radii measured from the SEM, and the modifications are all within ±3 nm of the designated values.

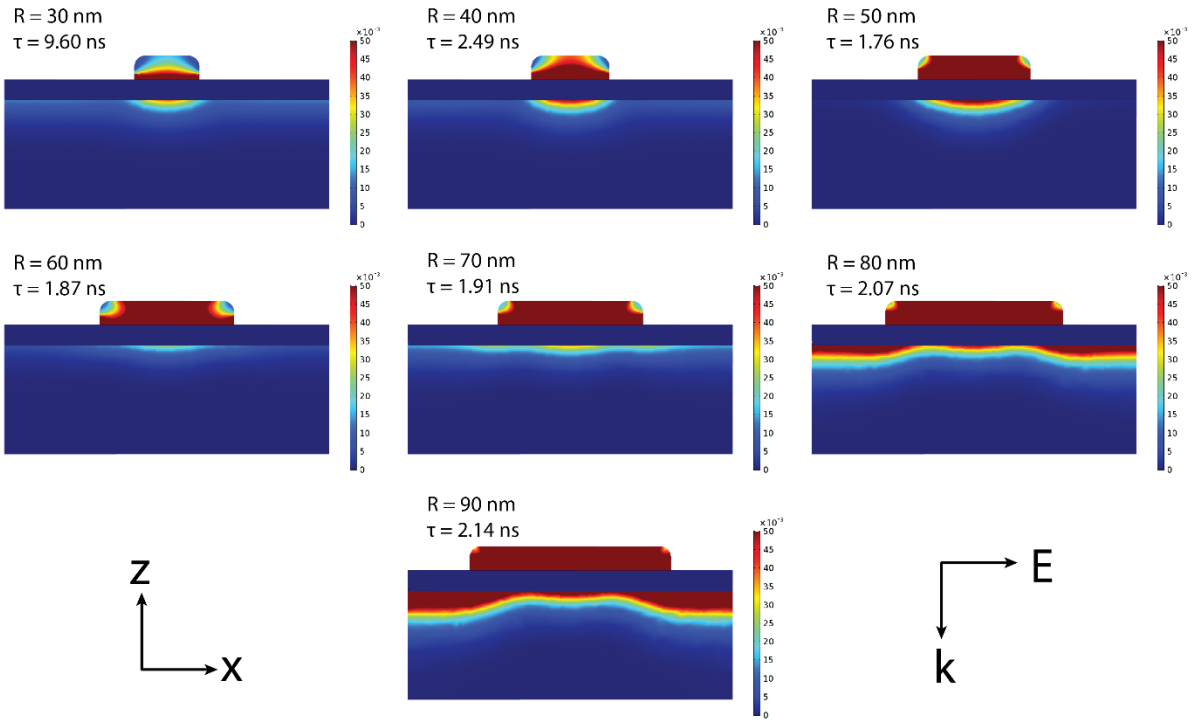

Figure 4.10 Normalized dissipated power distribution at the seven disk radii

For each disk radius, the dissipated power distribution is normalized to its maximum value, and the color range is optimized to highlight the dissipated power distribution in the disk and reflector. The inset in each plot indicates the disk radius and temperature decay time constant obtained from Figure. 4.4(d) in the main text. E and k represent the incident electric field and wavevector directions, respectively.

We then multiply the dissipated power distribution by a Dirac-Delta function in time to mimic an optical impulse, and use it as heat source for a separate Fourier heat-transfer COMSOL FEM model for further analysis. The thermal parameters used in the heat-transfer model are shown in Figure 4.11(b). In the heat-transfer FEM model, we simulate only one unit cell with the vertical

walls set as insulating boundary conditions. This greatly reduces the computational cost and accurately represents the fact that at times shortly after the pulse excitation, heat flowing into the unit cell from neighboring unit cells cancels out the heat flowing out. However, at longer times after pulse excitation, lateral heat spreading becomes significant because of the finite laser beam size and the Gaussian distribution of laser power. Such lateral heat spreading at longer time scale is not captured in our FEM model with insulating boundary conditions, therefore we need to use a higher-than-actual thermal conductivity value (4.33 W/m·K, Figure 4.11(b)) for the bulk SiO_2 substrate to compensate for it. The use of dissipated power from only the central frequency of the laser pulse is justified because the contributions from other frequency components are much smaller. Also the Gaussian (in time-domain) pulse can be simplified to an impulse excitation because the pulse duration used in experiment (~150 fs) is much smaller than the time scale of interest (>100 ps, when the heat transfer is dominated by lattice temperature rather than electron temperature). The Fourier heat-transfer model enables us to calculate the average temperature decay of the structure's top surface (gold nanodisk outer surface and exposed Al_2O_3 top surface) over time, i.e. the impulse response of the plasmonic system, on which we then perform fast Fourier transform (FFT) to get its frequency response $\Delta T(f)$. Lastly, we apply $\Delta T(f)$ to the expression proposed in ref[277], which accounts for the pulse cumulative effect in the TDTR measurement (i.e. sample surface's temperature rise due to one pulse does not decay to zero before the next pulse arrives, see ref[276]), to calculate the in-phase and out-of-phase components of the lock-in detected signal:

$$\mathrm{Re}[\Delta R_M(t)] = \frac{dR}{dT}\sum_{m=-M}^{M}\left(\Delta T\left(\frac{m}{\tau}+f\right)+\Delta T\left(\frac{m}{\tau}-f\right)\right)\exp(i2\pi mt/\tau)\exp\left(-\pi\left(\frac{f}{f_{max}}\right)^2\right)$$

$$\mathrm{Im}[\Delta R_M(t)] = -i\frac{dR}{dT}\sum_{m=-M}^{M}\left(\Delta T\left(\frac{m}{\tau}+f\right)-\Delta T\left(\frac{m}{\tau}-f\right)\right)\exp(i2\pi mt/\tau)$$

where $\mathrm{Re}[\Delta R_M(t)]$ and $\mathrm{Im}[\Delta R_M(t)]$ represent the real and imaginary parts of the lock-in detected signal, respectively, $\frac{dR}{dT}$ is the thermoreflectance coefficient, m is integer, f is the modulation frequency (~0.8 MHz used in experiment), τ is the duration between successive laser pulses (~13 ns used in experiment), $f_{max} = 100$ GHz and $\exp(-\pi(f/f_{max})^2)$ is a Gaussian factor to improve the convergence of the real part of $R_M(t)$ over M. For each t, M is chosen to be $M = 4.98\tau/t$ for

good convergence while keeping the computation time reasonable. Finally, the ratio between $\mathrm{Re}[\Delta R_M(t)]$ and $\mathrm{Im}[\Delta R_M(t)]$ is calculated to reproduce $-V_{in}/V_{out}$.

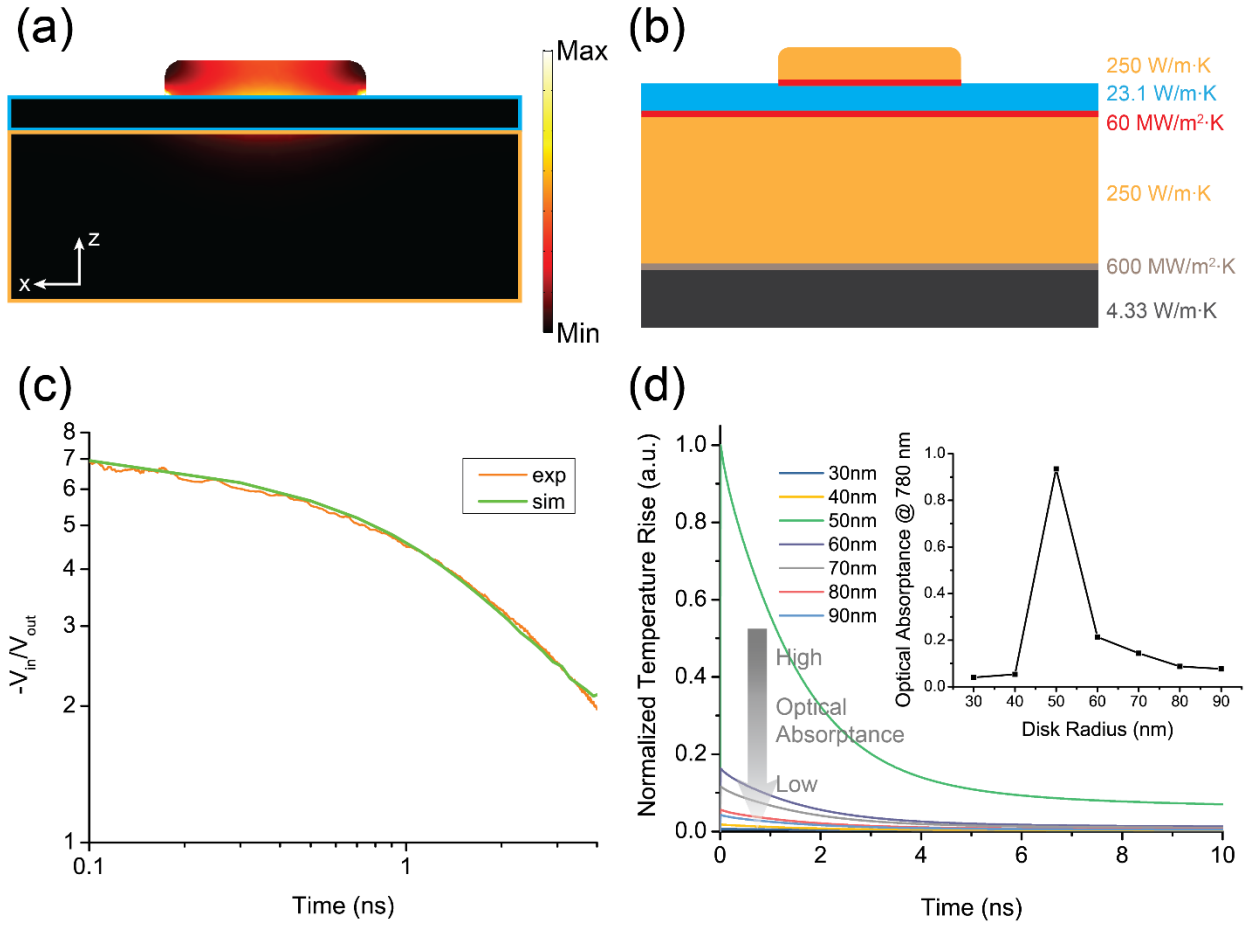

Figure 4.11 Calculation of $-V_{in}/V_{out}$

(a) Calculated power dissipation of 50 nm radius nanodisk under 780 nm light illumination. The blue- and yellow-outlined regions indicate the 20-nm-thick Al_2O_3 and 100-nm-thick Au reflector layers, respectively. (b) Thermal conductivities (in W/m·K) and thermal interface conductivities (in W/m^2·K) used for different layers in the Fourier heat-transfer finite element model. (c) Fitting of simulated and measured $-V_{in}/V_{out}$ versus pump-probe time delay of 50 nm radius nanodisk. (d) Simulated impulse response of seven different disk radii, normalized to their common maximum value. The grey arrow indicates that the initial temperature rise follows the trend of optical absorptance. Inset: simulated optical absorptance of 780 nm light for the seven disk radii.

5. ENHANCING GRAPHENE PHOTOCURRENT USING SURFACE PLASMON AND P-N JUNCTION

Disclaimer: A document with close resemblance of this section of the dissertation will be submitted for publication in a select press, the press reserves the first right of publication of this work.

5.1 Introduction

Since its first successful isolation from bulk graphite, graphene has been extensively studied as a photodetection material[214]. In addition to being cheap, lightweight and compact, graphene has a number of optical and electrical signatures that make it a unique photodetection material. Specifically, graphene offers: (i) unlimited detectable wavelength range due to the zero band-gap[280], (ii) uniform responsivity over the entire spectrum resulting from the invariant optical absorption (2.3%)[281], (iii) ultrafast response speed because of the ultrahigh carrier mobility (for photovoltaic effect)[179], [282] and thermal conductance (for photothermoelectric effect)[64], [283]–[285]. Despite these remarkable features, the relatively low responsivity (defined as the photocurrent amplitude per input optical power, in A/W) significantly hinders practical applications of graphene photodetectors. This is mainly due to the weak absorption of light by a single layer graphene[201]. Therefore, various systems have been investigated to assist light-graphene interaction and enhance the responsivity. Among these, quantum dot-loaded graphene phototransistor exhibits the highest responsivity gain[211], [286], but the strong gain comes at the price of the reduced operation speed (~10 ms, or 100 Hz) due to the slow quantum dot discharge process. Photonic waveguides have also been utilized to boost the responsivity, however, such structures usually have large and sophisticated device footprint because long waveguides are required to increase the photon-graphene interaction length[206], [287]. A third approach to enhance graphene photo-responsivity is to utilize plasmonic structures, which relies on the highly confined light-induced surface plasmon oscillations in metallic nanostructures to aid light absorption in graphene[30], [65], [72]–[74]. Such systems have relatively simple device configuration and do not compromise the graphene photodetector operation speed. However, most of the proposed plasmonic-enhanced graphene photodetectors utilize only on the optical

enhancement whereas electrical junction control (discussed in detail later) is largely neglected. In this section of the dissertation, I propose a system that utilizes both the optical and electrical controls of a plasmonic-enhanced graphene photodetector that shows superior performance compared to previously suggested designs.

The key factor in improving the responsivity of graphene photodetectors is in enhancing the photothermoelectric (PTE) effect that separates the free charge carriers via temperature gradient (∇T). This concept relies on earlier works demonstrating that the PTE effect is the dominant photocarrier generation mechanism in graphene[181]–[183], [208]. In simple words, the majority charge carriers (electrons or holes, depending on the doping type of graphene) are driven from the hot region to the cold region, and the net charge carrier movement leads to the detectable photocurrent. Typical graphene photodetectors rely on the optically-induced local heating to generate PTE current. However, intrinsic graphene sheets convert only 2.3% of incident light to heat, leaving much room for improvement. Plasmonic systems – devices that harness the optically-induced unbound electron oscillations in metallic scatterers to enable nanoscale light control[19], [22], [237], [288] – make a promising candidate to generate localized heating, thereby large ∇T, upon optical illumination[251], [289], [290]. Yet, equally important in graphene photocurrent generation is the uneven electrical doping level (i.e., a junction) at the center of the ∇T to give rise to a nonzero photocurrent[205]. Otherwise, if the doping level is uniform, the same type of charge carrier would be driven by the ∇T to opposite directions with the same strength and result in zero net current. In most plasmonic-enhanced graphene photodetectors, the doping is achieved passively by depositing metal contacts on graphene[291], and the uneven doping, thereby maximum photocurrent, occurs at the metal contact edges (see Figure 5.1 first row). The majority of previously reported approaches do not offer control over the graphene doping level because the doping level in the metal-contacted graphene region is fixed. In this work, we introduce the doping control in addition to the widely-used optical enhancement via plasmonic structures. Because the doping is achieved via electrical gating, we henceforth refer to doping control/enhancement as electrical or junction control/enhancement.

As reported in ref.[182], PTE effect largely dominates the photocurrent generation mechanism in graphene with channel lengths greater than 5 μm. Thus, in this work we neglect the competing photovoltaic (PV) effect (the channel length in our device is 50 μm). The PTE current in graphene is governed by

$$I_{PTE} = \int_0^W \int_{-L/2}^{L/2} s(x)\nabla T_{el} \frac{\mathrm{d}x\mathrm{d}y}{RW} \tag{5.1}$$

where W and L are the width and length of graphene sheet, respectively, $s(x)$ is the spatial distribution of the Seebeck coefficient (controlled by the doping type and level in graphene), T_{el} is the electron temperature, and R is the total resistance of graphene. To better illustrate the graphene PTE current generation mechanism, we simplify Equation 5.1 by considering only one dimension (along *x*-direction) and create a series of schematic illustrations in Figure 5.1. The illustrations are categorized into four cases (rows), depending on the optical heating and electrical junction enhancement scenarios. The last column of Figure 5.1 depicts the integrand of Equation 5.1, and the PTE current is directly obtained by calculating the area under each curve, with red-shaded area denoting positive contribution and blue-shaded area negative contribution. Case 1 represents the most pristine graphene photodetectors which consist of only metal contacts and graphene, with neither heating nor junction enhancement[177], [178]. Note that both the metal contacts and common contaminants p-dope graphene, thus the $s(x)$ is positive in both metal-contacted region and exposed region, and experiences a step due to the difference in the doping levels. As a result, the integrand has unequal positive and negative contributions to result in nonzero PTE current. Some previous works have studied the graphene PTE effect using vigorous electrical junction control without plasmonic enhancement[181], [183], [292], thus belong to Case 2. Here, a p-n junction is introduced at the center of the temperature gradient, and ensures a positive contribution to the PTE current on both sides. As mentioned above, plasmonic structures help to convert light into local heating (represented by high T(x) and dT/dx profiles in Figure 5.1), hence, most of the previously demonstrated plasmonic enhanced graphene photodetectors[30], [72], [74] fall into Case 3. It is evident that Case 4 with both optical heating and electrical junction enhancements results in the strongest PTE current, and this forms the backbone of the design presented in this work.

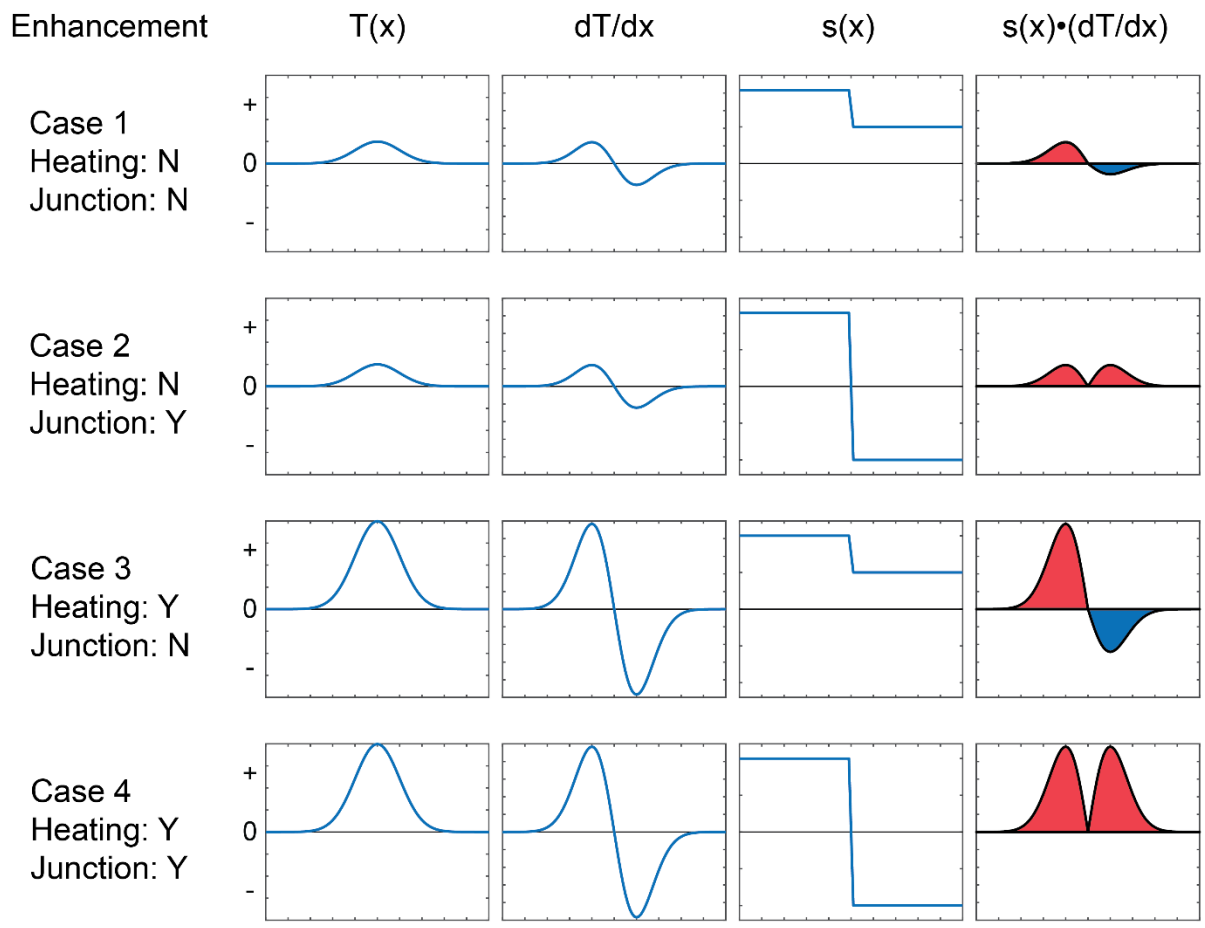

Figure 5.1 A one-dimensional schematic illustration of the photothermoelectric (PTE) current generation in graphene

Based on the enhancement conditions of optical heating and electrical junction (Y: yes, N: no), graphene photodetectors can be categorized into four cases, each represented by a row. In all plots, the horizontal axes denote the spatial coordinate *x*, and the vertical axes are denoted by their respective column headers. The T(x) column illustrates the electron temperature profile due to laser illumination, and the dT/dx column is obtained by taking the spatial derivative of T(x). The s(x) represents the spatial distribution of the Seebeck coefficient, and the s(x)·(dT/dx) column is obtained by taking the product of the s(x) and dT/dx columns. The PTE current is calculated by integrating the s(x)·(dT/dx) function, i.e. adding the areas of the shaded regions, with red (blue) denoting positive (negative) contribution to the PTE current.

5.2 Device design

Figure 5.1 illustrates the importance of the spatial overlap between the center of the optical heating area and a p-n junction for maximal graphene photocurrent generation. In this work, we create the p-n junction in graphene by a pair of split-gates formed by (from bottom to top) an aluminum (Al)-aluminum oxide (Al_2O_3)-graphene capacitor structure, and deposit Al nanodisks

on graphene to form gap plasmon structure with the underlying Al_2O_3 and Al layers to enhance optical absorptance. In this way, the optical heating enhancement (gap plasmon structure) and the electrical enhancement (split-gates) are seamlessly lumped together by their shared components of the Al_2O_3 and Al layers. More importantly, gap plasmon structures have been shown to exhibit high optical absorptance[262]–[264] and are especially efficient in light-to-heat conversion[185]. The choice of materials is based on two reasons: i) it is relatively easy to tune the resonance wavelength of Al gap plasmon structure in the visible spectrum to make color-sensitive graphene photodetectors; ii) the high quality of Al_2O_3 grown on Al guarantees robust electrical gating to graphene. In this work, we investigate the realistic optimal responsivities obtainable in graphene photodetectors that can be produced in large scales, thus chose to work with graphene grown by chemical vapor deposition (CVD) because of its compatibility with industry-level fabrication. Figure 5.2(a) depicts a schematic illustration of the proposed device and its working principle. The pair of split-gates are separated by a minuscule gap to ensure electrical isolation between the two gates, hence the doping level thus Seebeck coefficients on the two sides of graphene can be independently controlled by electrostatic gating. Simultaneously, the nanodisk gap plasmon structure absorbs the incident light and creates a localized temperature profile, which then drives the majority charge carriers on the two sides (electrons on the n doping side and holes on the p doping side) to opposite directions for maximized photocurrent. Figure 5.2(b) shows the cross-sectional view of the design and illustrates how the split-gates and the gap plasmon structure function together. We note that in the fabricated sample, the poor adhesion of nanodisks to graphene somewhat compromises the uniformity of the nanodisk distribution, but this issue can be resolved by introducing a thin Al_2O_3 layer between the nanodisks and graphene (not investigated in this work).

Since the plasmonic structure has more stringent requirements on layer thicknesses than the electrical gating, the bottom-most Al layer and the Al_2O_3 layer are carefully designed to be 100 nm and 20 nm thick, respectively, in order to achieve high optical absorptance in the visible spectrum. The split-gates are defined by electron-beam lithography (EBL) with a 150 nm wide gap (taking into account the fabrication limitations), Al metallization and liftoff, followed by atomic layer deposition (ALD) growth of Al_2O_3. A graphene sheet grown by CVD is transferred on the Al_2O_3 layer, and 30 nm thick Al nanodisks are then placed on the graphene sheet by EBL, metallization and liftoff. Figure 5.2(c) presents a close-up schematic view of the gap plasmon

structure sans the graphene sheet. The nanodisk radius is varied across samples to alter the absorptance spectrum thereby control the responsivity at different wavelengths. We also fabricated a separate sample containing only the gap plasmon structure (i.e., no graphene) for optical characterization, because the absorptance measurement requires an area of uniform gap plasmon structure larger than that of the graphene photodetector. In Figure 5.2(d), we show three spectra measured on three different areas, one without nanodisks (i.e., only 20 nm thick Al_2O_3 and 100 nm thick Al) and two with nanodisks of radii R = 50 nm and R = 60 nm, respectively. Since graphene's optical response in the visible range is negligible, it is reasonable to use Figure 5.2(d) as a guideline for the optical absorptance in the nanodisks-loaded graphene photodetectors. Based on the conclusions from ref.[185], on the mesoscopic scale, the optically induced ∇T on gap plasmon structure scales linearly with its optical absorptance. Hence, the responsivity of gap plasmon-assisted graphene photodetector is expected to follow the optical absorptance.

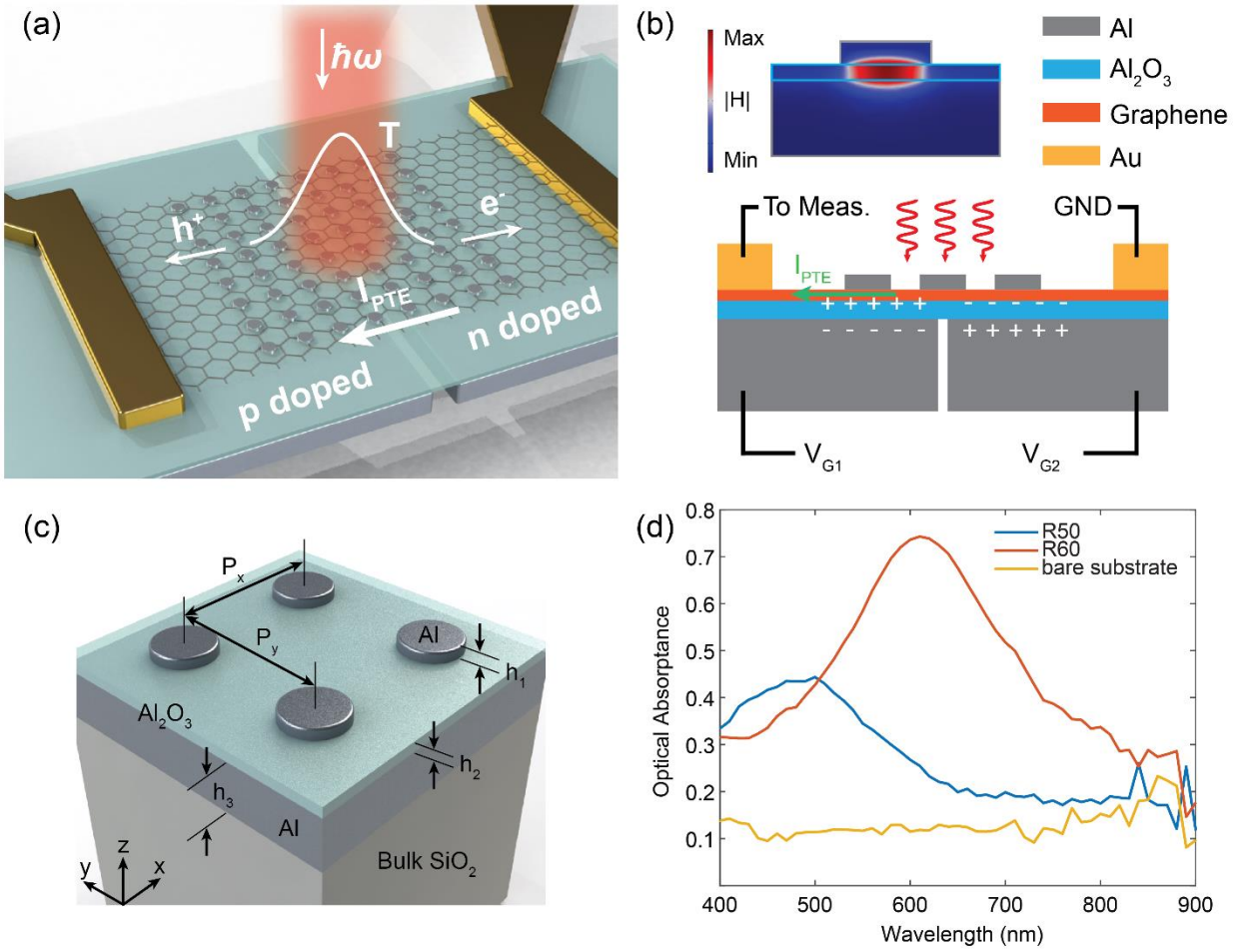

Figure 5.2 Graphene photodetector design and optical characterization

(a) Schematic of the graphene photodetector, which integrates both optical heating enhancement (realized via gap plasmon structure) and electrical junction enhancement (realized via split-gates), graphene lattice not drawn to scale. (b) Cross-sectional schematic of the graphene photodetector with split-gates and nanodisk gap plasmon structure. V_{G1} and V_{G2} are used to independently control the doping type in the two sides of graphene. Nanodisks cause localized heating by absorbing light, which drives electrons (holes) from center to the left (right) to give rise to I_{PTE}. Top left inset shows the simulated normalized magnetic field distribution under a resonant condition, where most of the incoming electromagnetic energy is squeezed in the Al_2O_3 layer instead of being reflected back. The nanodisk, Al_2O_3, and Al reflector layers are outlined by their representative colors. GND: ground. (c) Schematic of the gap plasmon structure: the aluminum (Al) nanodisk array (NDA). The Al nanodisks have a thickness of h_1 = 30 nm, arranged with periodicity $P_x = P_y$ = 300 nm, residing on an Al_2O_3 layer with a thickness of h_2 = 20 nm atop an Al back reflector layer with a thickness of h_3 = 100 nm. The disk radius varies across NDAs, and all the arrays are deposited on a 0.7 mm thick bulk SiO_2 substrate. (d) Measured optical absorptance spectrum in the range of 400 – 900 nm, on two NDAs with R = 50 nm and R = 60 nm, and on the bare substrate (only Al_2O_3 and Al layers on bulk SiO_2) without nanodisks. The absorptance measurement is carried out on a sample containing no graphene.

5.3 Results and discussion

We fabricate electrical contacts for electrical characterization under vacuum and room temperature conditions. Figure 5.3(a) shows a microscopic image of the fabricated device with R = 60 nm nanodisks, as well as the electrical connections that are made to the device for graphene electrical resistance (R_{SD}) and photocurrent (I_{PTE}) measurements. We first measure the R_{SD} while independently sweeping the voltages V_{G1} and V_{G2} on the split-gates and show the result in Figure 5.3(b). The central maximum R_{SD} point indicates the charge neutrality point (CNP), and two orthogonal lines intersecting at the CNP can be drawn to divide the gating condition into four different regimes, based on the types of carrier supplied to either side of graphene. The asymmetry in the two gating voltages at the CNP is likely due to the trapped charges in the Al_2O_3 layer introduced during the fabrication processes. Next, for the I_{PTE} measurement, a continuous-wave (CW) laser with λ = 638 nm and a power of 32 μW is focused to a spot size of ~10 μm, modulated by a mechanical chopper at 651 Hz, and illuminates the central area of the photodetector (red spot in Figure 5.3(a)). The I_{TPE} is then collected from the source and drain contacts using a lock-in amplifier that is synchronized with the mechanical chopper. Figure 5.3(c) shows the measured I_{PTE} when V_{G1} and V_{G2} are swept, from which distinct features can be seen in the four different doping regimes defined in Figure 5.3(b). Additionally, a diagonal line can be drawn along the zero-I_{PTE} line in the p-p and n-n doping regimes. The three dashed lines divide Figure 3c into six regions exhibiting alternating signs of I_{PTE}, which clearly indicates the dominance of the PTE effect in the photocurrent generation mechanism[182], [183]. It is also evident that the I_{PTE} is strongest under the p-n or n-p doping regime, in agreement with our previous discussion. Finally, we measure the I_{PTE} spatial map in the area outlined by the dashed box in Figure 5.3(a), while keeping the gating voltages at V_{G1} = -2 V and V_{G2} = 9 V (marked by the star in Figure 5.3(c)). As can be seen from Figure 5.3(d), the maximum I_{PTE} happens at the central line where the p-n junction is created by the split-gates, and diminishes as the laser moves away from it. The I_{PTE} changes sign at the source and drain contact edges, due to the uneven doping between metal-doped graphene and electrostatically-doped graphene (i.e. p(Au)-p^+(G1) on the source side and n(G2)-p(Au) on the drain side). We calculate the average I_{PTE} from the gap plasmon-assisted graphene photodetector by taking the average of the measured data points inside the box highlighted in Figure 5.3(d). The measured responsivity is 52 μA/W on a device with nanodisks of radius R = 60 nm, which has an optical absorptance of 71% at the incident laser wavelength 638 nm.

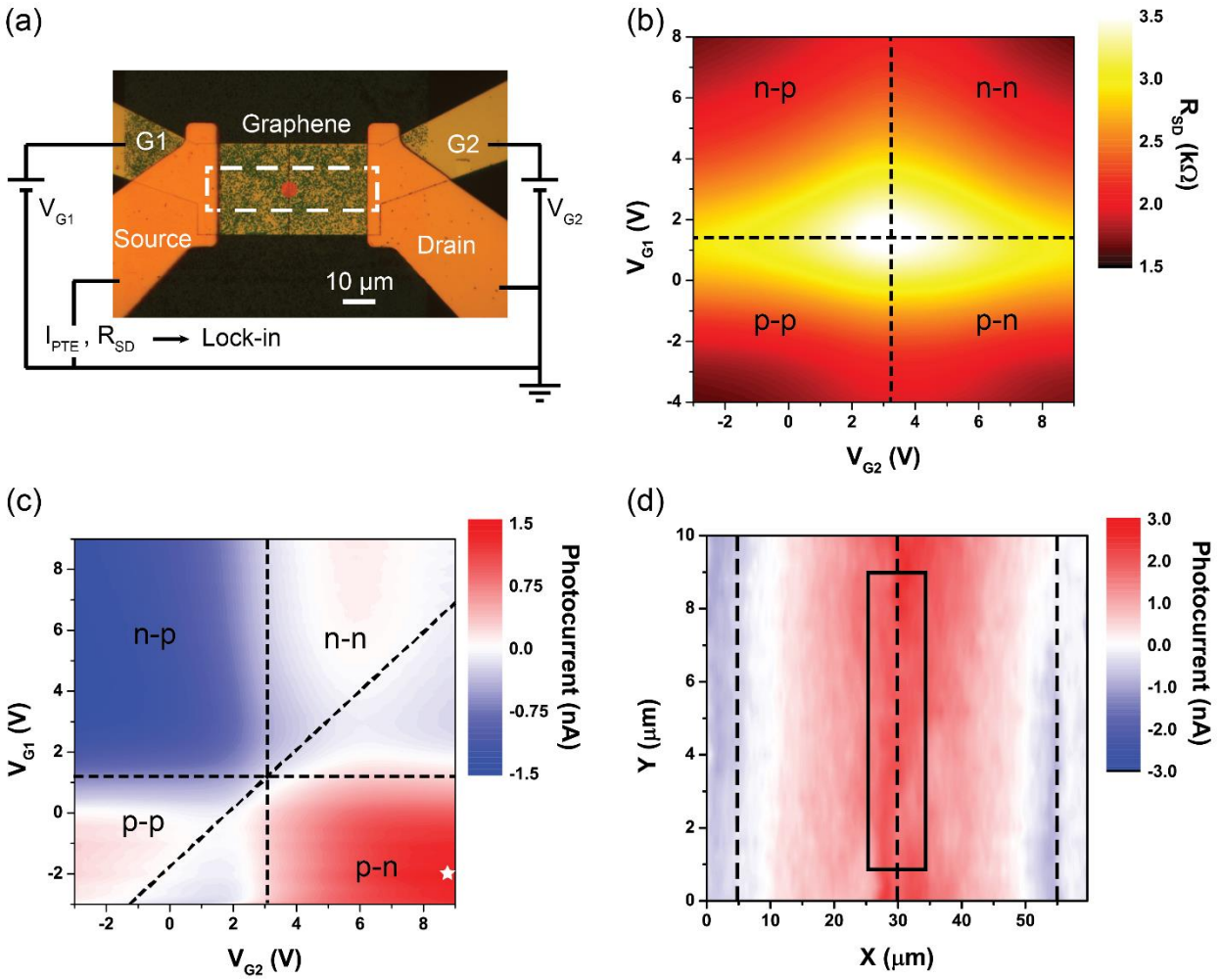

Figure 5.3 Photocurrent characterization of optically- and electrically-enhanced graphene photodetector

(a) Microscopic image of a fabricated graphene photodetector loaded with nanodisk with a radius R = 60 nm, and the schematic for the electrical measurements. The green shade results from the strong absorption of the red part of the visible spectrum by the nanodisks. V_{G1} and V_{G2} are the gating voltages supplied to the two sides of graphene separated by the 150 nm wide gap in the bottom-most Al layer, the graphene photocurrent signal is measured using a current preamplifier and a lock-in amplifier via the source and drain contacts. The graphene resistance is obtained separately by measuring the voltage drop across the source and drain contacts when a 100 nA current modulated at 17.35 Hz is supplied to graphene. (b) Measured graphene electrical resistance (R_{SD}) when V_{G1} and V_{G2} are independently swept. Four junction regimes are identified around the CNP. (c) Measured photocurrent signal as V_{G1} and V_{G2} are independently swept, the dashed lines mark the photocurrent sign changes. The CW laser for this measurement has a power of 32 μW, a diameter of ~10 μm, and its illumination position is marked by the red spot in (a). (d) Spatially resolved photocurrent map in the area marked by the dashed box in (a), measured with V_{G1} = -2 V and V_{G2} = 9 V (indicated by the star in (c)). The vertical dashed lines denote the source/drain contacts and the central 150 nm-wide gap, respectively. The data points in the boxed region are used to calculate the average responsivity of this device.

To compare the four cases presented in Figure 5.1, we measure the photocurrent in different locations of two separate devices both gated to achieve a p-n junction in the center, and show the results in Figure 5.4(a). One of these devices contains only graphene sheet (top left in Figure 5.4(a))

and the other is loaded with nanodisks with radius R = 60 nm (top right in Figure 5.4(a)). In both devices, laser illumination on the central line corresponds to the cases of the enhanced p-n junction, whereas illumination on the Au electrode/graphene interface denotes un-enhanced junction, as can be seen from the reversed sign (because of the p(Au)-p^+(G1) doping on the left edge, and p(G1)-n(G2) doping at the center) and lower I_{PTE} amplitude on the edges of Figure 5.3(d) compared to the central area. On the other hand, nanodisks dramatically increase the optical absorption thereby ∇T, making Device 2 represent the cases of enhanced optical heating. The table in Figure 5.4(a) summarizes the measured responsivities for the four different cases. The absolute values of the responsivities nicely correlate with the schematic illustrations in Figure 5.1, strongly substantiating our prediction as well as showcasing the power of ∇T and junction enhancement. By comparing the photocurrent of Case 4 and Case 1, we conclude that a 25-fold responsivity increase can be achieved with optical and electrical enhancement compared to the generic (un-enhanced) case.

We then repeat the measurement using two additional laser wavelengths (532 and 825 nm) on three devices (no nanodisk, with disk radius R = 50 nm and R = 60 nm, respectively). These measurements allow us to investigate the correlation between the optical absorptance and the I_{PTE} responsivity. In Figure 5.4(b), we plot the average responsivity calculated in the same way as shown in Figure 5.3(d), versus the measured optical absorptance. The red fitting line (note that the red line is a linear fit, but appears curved due to the log-log plot scale and the *y* axis starting from 3 μA/W) indicates that the responsivity scales linearly with the optical absorptance, agreeing with our previous discussion and design principle that the optically induced ∇T, hence responsivity, is directly proportional to the optical absorptance. Additionally, the source-drain bias (V_{SD}) can be utilized to enhance the responsivity by creating a static electric field between the two electrodes to facilitate the electron harvesting. Figure 5.4(c) presents the measured responsivity as the V_{SD} is swept from -2.3 to 2.3 V, from which it can be concluded that an additional 7-fold responsivity enhancement can be achieved at 2.3 V compared to zero V_{SD}. All measurements except the one shown in Figure 4c are done with V_{SD} = 0 V.

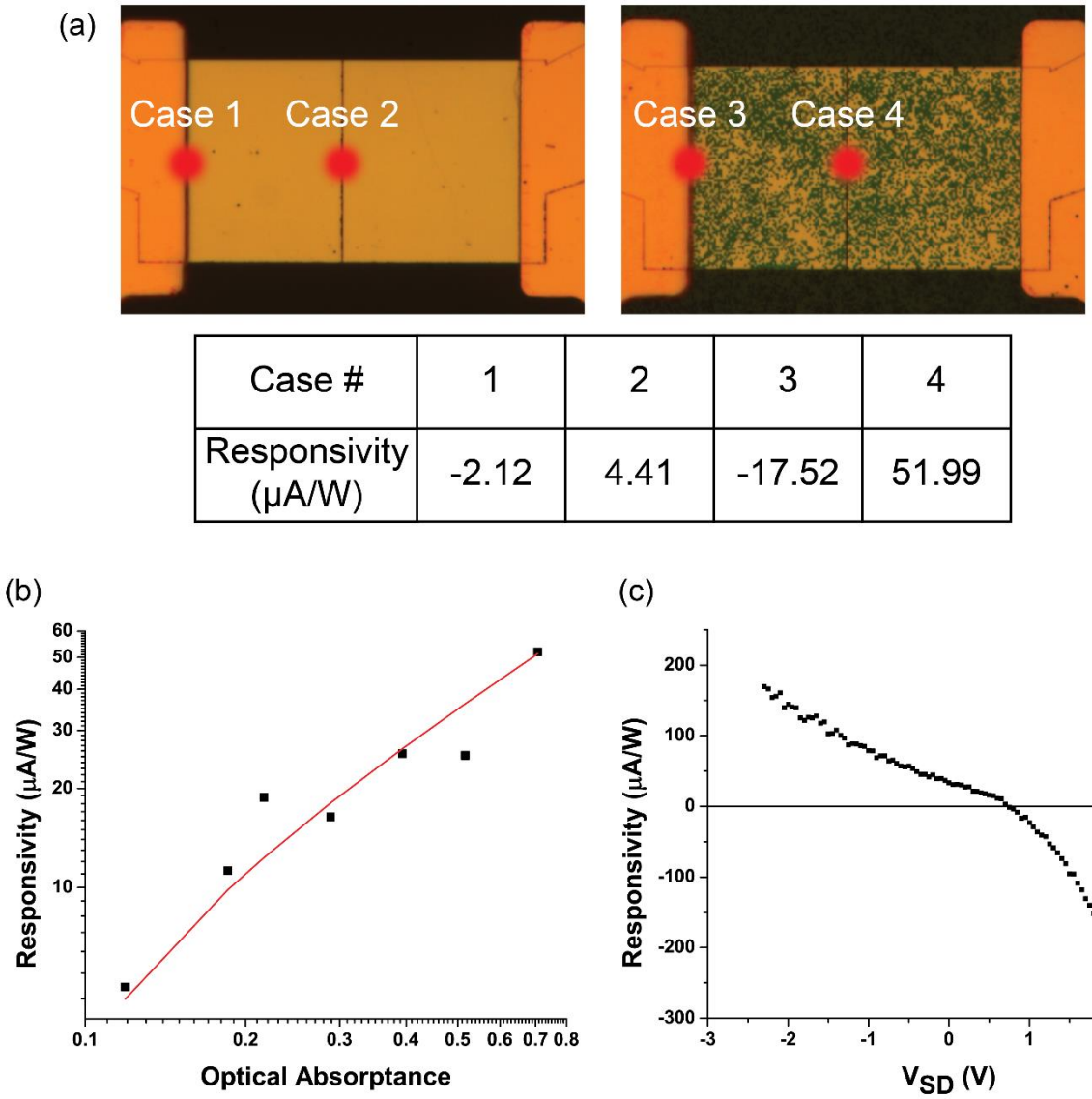

Case #	1	2	3	4
Responsivity (μA/W)	-2.12	4.41	-17.52	51.99

Figure 5.4 Graphene photodetector enhancement

The four cases categorized in Figure 5.1 can be reproduced in the experiment by illuminating the laser spot on the four positions in (a). In all four measurements, both devices are gated to achieve a p-p^+ (p-n) junction on the left edge (in the center) to represent the un-enhanced (enhanced) electrical junction. The device on the left (right) contains no nanodisks (nanodisks of R = 60 nm) therefore represent the case of un-enhanced (enhanced) optical heating. The table summarizes the measured photo-responsivities of the four cases, with case numbers corresponding to the enhancement schemes in Figure 5.1. (b) Measured photo-responsivity versus optical absorptance (black data points), and the linear fit (red line) to the data points. The linear fit appears to be curved due to the log-log plot scale. (c) Measured photo-responsivity as a function of an applied DC source-drain bias (V_{SD}), on a device with an optical absorptance of 71% at the illuminating laser wavelength of 638 nm. All measurements in (b) and (c) are carried out by illuminating the laser at the central p-n junction.

The responsivity can be further enhanced if the following two methods are implemented together with the proposed device configuration: i) to increase the optical absorptance and ii) to

improve the quality of graphene. In this work, the highest optical absorptance achieved is 71%, due largely in part to the non-ideal adhesion between nanodisks and graphene. The optical absorptance can be improved by refining the fabrication process, for example by introducing a thin Al_2O_3 layer between nanodisks and graphene to increase adhesion between nanodisks and graphene. As a proof of concept demonstration of the device design, this work was done with CVD graphene, however, it is well known that exfoliated graphene exhibits stronger photoresponse, and the responsivity is expected to see a significant increment if exfoliated graphene is used in combination with the proposed device design.

5.4 Conclusions

As the photothermoelectric (PTE) effect has been shown to be the dominating mechanism of the photo-carrier generation in graphene, we propose a new approach to enhance graphene photocurrent by spatially overlapping plasmon-induced optical heating and a p-n junction. We design a novel metal/dielectric/nanodisk tri-layer device configuration, which forms a gap plasmon structure and a pair of split-gates to simultaneously realize enhanced plasmon-induced optical heating and enhanced p-n junction control, respectively. Specifically, the bottom metallic layer (with a gap in the center) serves as the back reflector of the gap plasmon structure, as well as the electrodes of the split-gates. The middle dielectric layer constitutes the optical spacer for gap plasmon structure, also the gating dielectric of the split-gates to create a p-n junction. Graphene is then placed on the dielectric layer, followed by deposition of the nanodisk array. Although the nanodisks do not play a role in electrical control, they are an essential part of the gap plasmon structure and efficiently convert light into localized heating. With rigorous experiments, we proved the dominance of the PTE effect in graphene photocurrent generation, and showed that with optical heating and electrical p-n junction enhancement, the photocurrent sees a 25-fold increase compared to the un-enhanced case. A source-drain bias of 2.3 V can further enhance the photocurrent by 7 folds. The overall thickness of such a photodetector is 150 nm, much smaller than the state-of-the-art semiconductor photodetectors which are several microns thick. In addition, the relatively narrowband optical absorptance of the nanodisk gap plasmon structure makes it possible to control the color sensitivity using nanodisks with different radii, eliminating the need for an additional color filter layer when integrated into cameras. Lastly, we note that although photodetectors made with exfoliated graphene usually exhibit higher responsivities[285], [287],

they are not suited for large-scale manufacturing due to the limited size and yield of exfoliated graphene. Our work indicates optimal responsivities that are achievable with CVD graphene, which holds promise for mass production and commercialization. The proposed design represents a leap towards realizing graphene's potential in constructing ultrathin, lightweight, and ultrafast photodetectors.

6. ENABLING OPTICAL STEGANOGRAPHY, DATA STORAGE, AND ENCRYPTION WITH PLASMONIC COLORS

Disclaimer: A document with close resemblance of this section of the dissertation is under review for publication in Nature Communications, Nature Publishing Group (or any other press to which the document should be submitted) reserves the first right of publication of this work.

6.1 Introduction

The rapid development of the Internet-of-Things (IoT), widespread social networking, and multimedia content delivery with the increasing dominance of high-resolution digital static and dynamic color images produces an astounding amount of data that should be stored and accessed around the world. The price for the increasing dependence on data is a never-ending growth of the Global Datasphere that has been estimated to be 33 zettabytes (ZB, 1 ZB = 10^{21} bytes) in 2018 and expected to exponentially grow up to 175 ZB by 2025[293]. The class of "cold" data – those that constitute ~40% of the overall data volume but are accessed less frequently[294], exemplified by digitized movies, images, texts, and big data, needs to be stored at long-lasting, physically-safe, and low power-consuming archives. Currently, the most widely-used medium for cold data storage is Blu-ray discs, for their superior performance in data security, robustness, durability, and cost of operation, compared to magnetic-recording media such as hard disc drives (HDDs). However, Blu-ray discs are nearing the theoretical limit for storage density, as a basic storage unit accommodates only *one* bit of information, and its size is already close to the diffraction limit of the readout laser[295] thus cannot be further shrunken. There is a rising need for affordable, long-term storage of big data with a high-speed readout and this need is becoming a social and technical challenge[295].

Alternative optical storage has been already offering solutions as a media capable of storing large volumes of data with a promise to cover at least several human generations[296]. Thus far, the optical storage industry has been employing direct engineering strategies: (i) recording on both the land and the valley regions of the optical disc groove, (ii) increasing the number of layers per disc, and (iii) arranging the multilayer discs in parallel arrays[295]. This straightforward multi-layer, multi-disc engineering strategy does not deliver a significant cost per bit advantage – each

layer on such a disc is still fabricated individually. Also, by retrieving only a single bit of information per reading, the sequential readout of information significantly limits the overall performance. In light of this, research efforts have spurted towards advanced optical data storage systems where *more than one* bit of information could be stored in a single storage unit[39], [297]–[300]. Although some of those studies advanced the exploration of optical data storage, most of the proposed solutions were not mature for practical applications. For example, Chen *et al.*[297] used a large storage unit area that compromised the desired storage density, the work of Mansuripur *et al.*[298] required a scanning laser for information readout that could limit the operation speed, and the technique proposed by Li *et al.*[299] relied on a very slow chemical process to increase the data storage capacity. While the recent work by Wiecha *et al.*[39] is an encouraging and important progression towards practical applications in many aspects, the proposed complicated structure may pose a challenge to scalable manufacturing.

Because of their unparalleled ability to localize light, plasmonic metasurfaces have enabled various miniaturized light manipulation techniques[19], [73], [237], and they also provide a viable solution to further increasing the optical data storage capacity as well as the readout speed. Here, we propose a simple anisotropic plasmonic metasurface (APM) consisting of aluminum (Al) nanoantenna elements to encode many-bit information in a single nanopixel with an area of 500 × 500 nm^2, which can be retrieved via customized color codes reflected from the nanopixel under a meticulously designed sequence of polarizer arrangement. Importantly, the optical rotation effect[301] of such APM dictates that when broadband polarized light interacts with each nanopixel of the APM, the reflected spectrum (thereby color) is distinctly modified as the polarization of either the incident or the reflected light changes. We make use of this exceptional flexibility to realize *high-density optical data storage*, *optical steganography and encryption*. In high-density optical data storage we demonstrate a storage density that is 5% greater than the state-of-the-art Blu-ray disc using a readout system with moderate sensitivity. The storage density can be increased even further by employing machine learning for color or spectral discrimination, along with a readout system of higher spectral sensitivity. Furthermore, such color-based data storage is compatible with our new parallel-processing data readout scheme where the information stored in multiple storage units is acquired simultaneously, significantly surpassing modern sequential systems in operation speed. In optical steganography**,** we encode more vivid "cross-talk"-free color images in a common area than any other relevant work. In information encryption**,**

our APM is for example capable of encrypting the entire English alphabet in a single ciphertext element, showing enhanced functionality vs comparable digit-based plasmonic/optical encryption.

Our APM relies on the localized surface plasmon resonance (LSPR) – resonant free-electron oscillations at the metal-dielectric interface when stimulated by light – to modify the reflection spectrum. Since the LSPR is very sensitive to the relative angle between the anisotropic nanoantenna orientation and the incident/reflected light polarization, the reflected spectrum (color) varies with the relative angle between the two. As a result, the information can be stored in the orientation states of the nanoantennas, and conveniently retrieved by their reflected colors. Compared to polarization-tunable color-producing structures working in the *transmission* mode[302]–[306], a reflective metasurface, which is free from anti-reflection complications and propagation-accumulated phase ($\Delta\Phi = \beta \times d$, where β is the propagation constant and d is propagation distance), can be made with smaller thicknesses while simultaneously exhibiting high reflection efficiency[118], [119], [307]–[311]. Such a feature can be utilized to shrink the device footprint and increase the saturation and intensity of the reflected colors in a bright-field optical microscope, leading to clear and vibrant microprints[312]. In contrast to the plasmonic color-producing structures based on composite metallic resonators, the use of all-Al design not only simplifies fabrication process by forming connected metal structures but also reduces the manufacturing cost[313]. Moreover, the proposed design is compatible with commercial nanoimprint process[314] and promises to bridge the gap between proof-of-concept demonstration and large scale manufacturing. With respect to color generation performance, our structure yields a continuous closed elliptic trace on the International Commission on Illumination (CIE) 1931 chromaticity diagram, while most state-of-the-art polarization-tunable color-producing structures can only produce a limited range of colors represented on the same diagram by a limited straight segment[303]. Such a significant broadening of the reproducible colors is achieved due to the dispersive optical-rotation effect near the LSPR band of the Al nanoantennas. Employing these advantages, we experimentally showcase a data storage APM with a storage density 5% greater than Blu-ray discs and a 143-fold readout speed increase, as well as advanced steganography color displays and encrypted color tags, featuring large viewing angle tolerance and abated “cross-talk” effect (i.e., undesired mixing of the overlaid images between the different polarization states).

6.2 Results

6.2.1 Theoretical fundamentals and numerical simulations

The proposed metasurface consists of periodic arrangements of rectangular-shaped Al nanoantennas attached to an optically thick Al film. This architecture is capable of converting the diagonally-oriented (45° with respect to the long axis of the nanoantenna) linearly-polarized (LP) visible light into other polarization states. Importantly, a complete 90° optical rotation angle can be readily achieved with high reflection efficiency and device compactness due to the LSPR. Al is chosen here due to its broad-band plasmonic properties - it supports plasmon resonances in the wavelength range from the ultraviolet to the near-infrared[308]. Moreover, the lower cost of Al and its stability in air makes it more suitable for our goal than conventional plasmonic metals such as silver and gold.

As shown in the lower inset of Figure 6.1(a), the unit cell of the APM spans an area of 250 nm × 250 nm with the optimized length (l), width (w) and thickness (h) of the nanoantenna being, l = 200 nm, w = 80 nm, and h = 70 nm. The period of the nanoantenna array is kept subwavelength to avoid diffraction, which causes unwanted sharp peaks in the reflectance spectra and deteriorates the color saturation. The red curve in Figure 6.1(a) indicates the phase difference δ that exhibits a pronounced 180° drop from ~460 nm to 600 nm. The four insets in Figure 6.1(a) show the calculated elliptical polarization states of the reflected E-field at four select wavelengths, implying that the polarization state of the strongest reflected light is wavelength-dependent, a quintessential feature of the optical-rotation effect[301], [315].

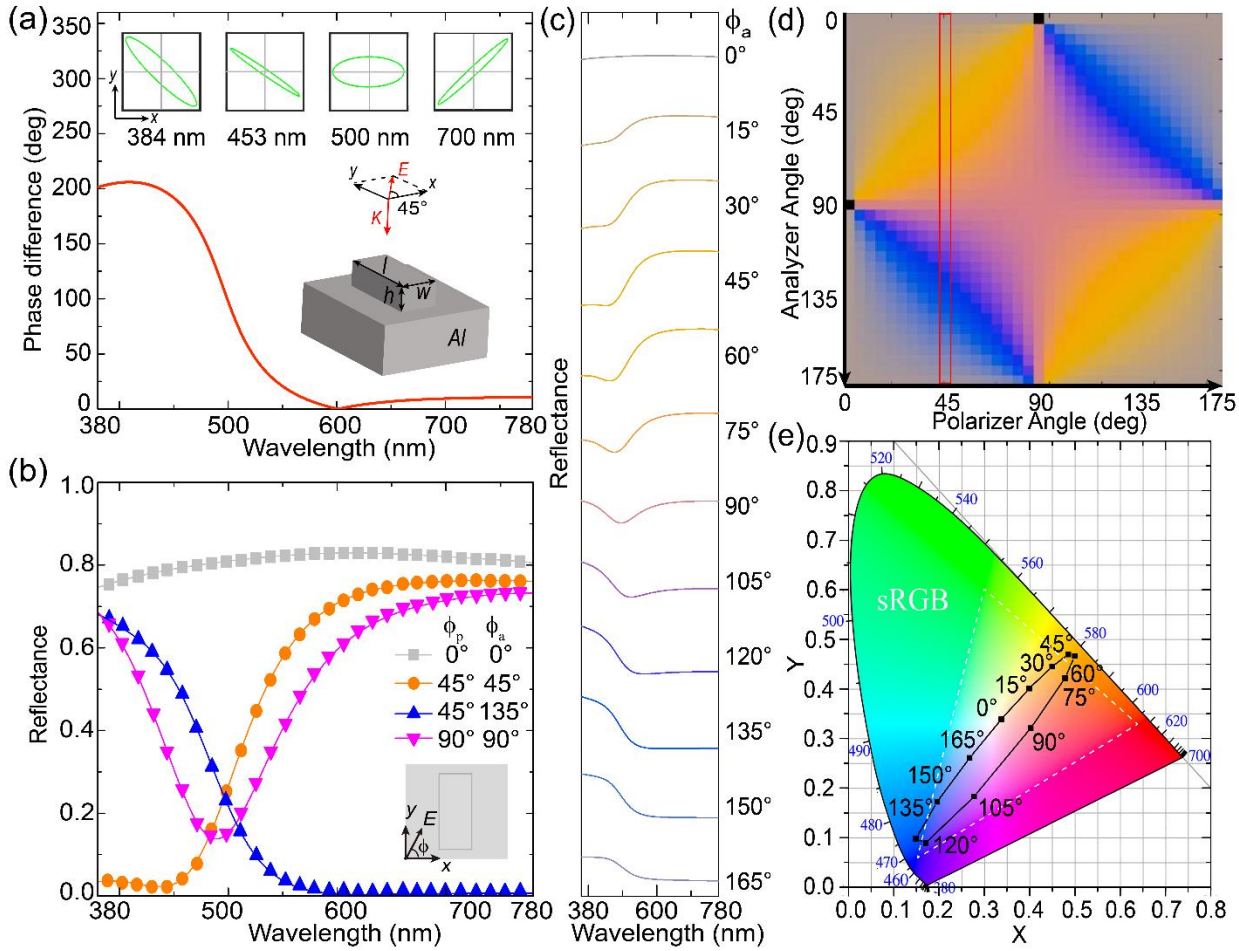

Figure 6.1 Simulated results of the APM color filter

(a) Calculated reflected light phase difference between *x*- and *y*- polarizations. The four upper insets show the elliptical polarization states of the reflected wave at four select wavelengths, and the lower inset is a schematic of one unit cell containing an individual Al nanoantenna with the incident polarization state. (b) Simulated reflectance spectra corresponding to different combinations of polarizer-analyzer angles, leading to four distinct colors. (c) Simulated spectra of light reflected from the APM when the analyzer is rotated from 0° to 165° with a step of 15°, while the polarizer is fixed at 45° with respect to the long axis of the nanoantenna. The lines in **c** are presented in colors calculated from a given reflectance spectrum and the color-matching functions. (d,e) Calculated color palette and corresponding color information on the CIE 1931 chromaticity diagram, when both the polarizer and analyzer are rotated. Colors are obtained with simulated reflectance spectra and color-matching functions. The elliptical color palette shown in (e) is remapped from the region enclosed by the red box in (d).

The detailed simulation approach is given in the Methods section, and the polarized field calculations are described in Supplementary Information. To make APM produce a wide palette of colors, various combinations of polarizer-analyzer angle differences ($\phi_p - \phi_a$) are utilized. The corresponding reflectance spectra at normal incidence are depicted in Figure 6.1(b). For (ϕ_p=0°, ϕ_a=0°), the reflectance spectrum becomes nearly flat across the entire visible spectrum, and the APM reflects a grey color. On the contrary, the spectra for (ϕ_p = 45°, ϕ_a = 45°), (ϕ_p = 90°, ϕ_a = 90°)

and (ϕ_p = 45°, ϕ_a = 135°) show distinctive profiles, where the maximum reflectance exceeds 70% while the reflectance at off-resonant wavelengths is highly suppressed. Such a high contrast between the peak and dip values in the reflectance spectra improves color saturation and stability against fabrication uncertainties. Figure 6.1(c) depicts the simulated reflectance spectra when the analyzer is rotated from ϕ_a = 0° to ϕ_a = 165° with a step of 15° when the polarizer angle is fixed at 45° with respect to the long axis of the nanoantenna. The corresponding color palette versus polarizer-analyzer angle combinations is plotted in Figure 6.1(d). Based on the color matching functions defined by CIE, distribution of the colors in the CIE 1931 diagram can be clearly observed in Figure 6.1(e).

6.2.2 Optical steganography: plasmonic “kaleidoscope”

We fabricate the simulated all-Al APM with standard electron-beam lithography (EBL), metallization and lift-off technique. A detailed description of the fabrication process is introduced in the Methods section. Figure 6.2(a) shows the measured reflectance spectra under the same polarizer-analyzer combinations as shown in Figure 6.1(b). The excellent uniformity and high-fidelity profile of the fabricated nanoantennas lead to a good agreement between measured and simulated spectra. Some differences are due to the shape distortion at the fabricated nanoantenna corners, as well as changes in optical properties of nanostructured Al, which are not accounted for in simulations. To explore the potential use of this APM as a tunable plasmonic color filter, we photographed the colors with a chromatic charge-coupled device (CCD) camera integrated into an optical microscope. The detailed optical setup is schematically presented in Supplementary Figure 6.6. For comparison, we present the simulated and experimentally photographed colors (blue, orange, magenta and grey) in the left and right columns of Figure 6.2(b), respectively.

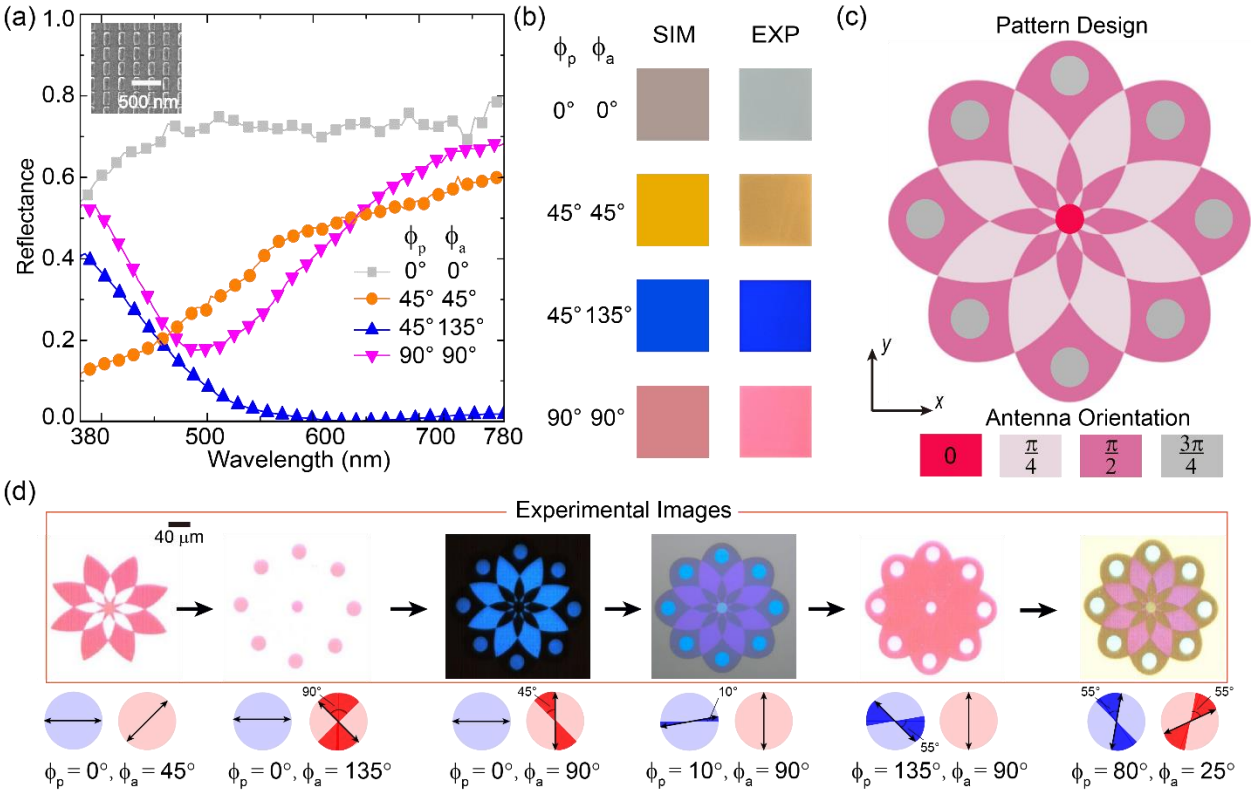

Figure 6.2 Experimental results of the APM color filter and steganography

(a) Measured reflectance spectra of the APM under four different combinations of polarizer-analyzer angles corresponding to those in Figure 6.1(b). Inset: SEM image of the Al nanoantennas taken in a random area of the fabricated APM. (b) Comparison between the simulated colors (left) and CCD camera photographed colors (right) under the four polarizer-analyzer combinations (same as in (a)). All photographed images were obtained by collecting the reflected light into the CCD camera with a 20× objective lens (NA = 0.45) under white light illumination. (c) Schematic of the steganographic flower pattern presented with different colors indicating different nanoantenna orientations. (d) Experimental optical micrographs upon rotating polarizer and analyzer. The circles below the photographs represent the polarizer (blue) and analyzer (red) angles, with the highlighted regions and corresponding numbers indicating the angles by which the polarizer/analyzer is rotated from the previous state.

The grey, blue, and magenta colors obtained (photographed) from the experiment agree reasonably well with the simulated ones, while the experimental orange color exhibits some discrepancy from the simulation. The discrepancy can be explained by the orange spectral curve depicted in Figure 6.2(a) – the broader resonance linewidth and relatively flat reflectance profile lead to the reduced color saturation.

A broad palette of colors can be observed when rotating the polarizer and analyzer. In contrast to the dynamic plasmonic colors tuned by heat[316] or chemical reaction[35], [299], [317], the appearance of the color images encoded by our meticulously designed APM can be readily changed without causing any deformations to the structure. Such an APM opens up an avenue for

advanced steganography – a technique used to conceal a message or image within another message or image. To demonstrate the concept of steganography with a plasmonic "kaleidoscope", we design a pattern of an eight-petal flower decorated with a core and eight circular speckles as depicted in Figure 6.2(c). The areas occupied by differently oriented nanoantennas ($0, \frac{\pi}{4}, \frac{\pi}{2}, \frac{3\pi}{4}$, all nanoantenna orientations are with respect to the *x*-direction henceforth) are labelled by different colors and nanoantenna orientation angles. The square Al nanoantennas (with dimensions of $l \times w$ = 80 nm × 80 nm) are used as the metasurface background, which blends in well with the peripheral part of the flower at specific polarization states. The performance of the plasmonic steganography is presented in Figure 6.2(d). A magenta flower with eight petals is perfectly observed when the polarizer and analyzer are set at 0° and 45°. When the analyzer is rotated by 90° in the counter-clockwise (CCW) direction, the flower pattern undergoes dynamic profile change with the disappearance of the petals and emergence of "cluster of speckles", because the areas occupied by $\frac{\pi}{4}$ and $\frac{\pi}{2}$ oriented nanoantennas perfectly match the colors generated from the background square-shaped nanoantennas. Simultaneously, the areas occupied by 0 and $\frac{3\pi}{4}$ oriented nanoantennas render a clear-cut magenta flower which sharply contrasts with the background. Based on the same principle, more distinct images from this pattern can be revealed under many other polarizer and analyzer angle combinations (see Figure 6.2(d)), largely increasing the information capacity of the steganography technique.

6.2.3 Towards a higher spatial resolution

On top of expanding the available color palette, tunability and abating the "cross-talk" effect, shrinking the dimensions of distinguishable nanopixels is of great importance for increasing the spatial resolution and information capacity of the APM. In order to find out the minimum nanopixel size that can support distinguishable colors, we fabricate checkerboard patterns with alternating nanopixels formed by nanoantennas in different orientations as shown in Figures 6.3(a-c). When the polarizer is 0°, and the analyzer is 90° with respect to the *x*-direction, the alternating blue-black checkerboard pattern is distinctly observed as depicted in Figures 6.3(a,b).

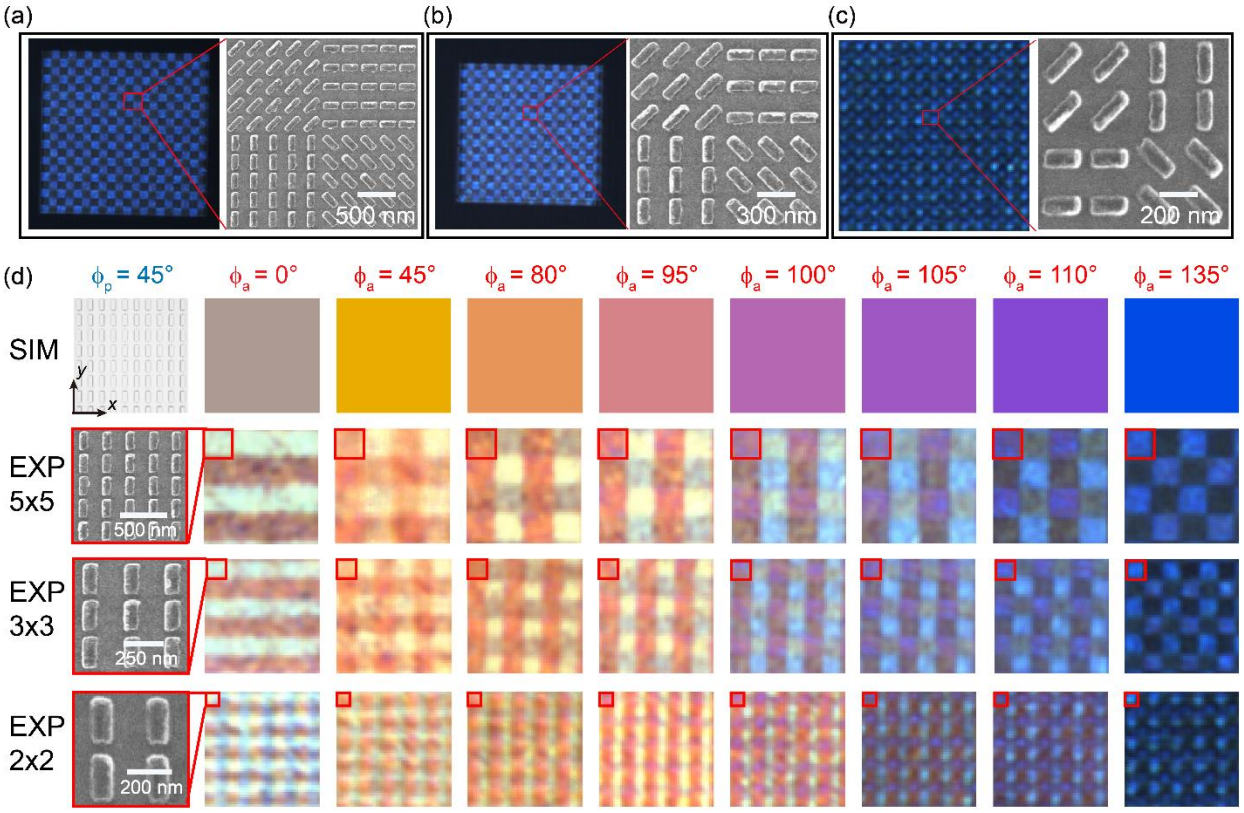

Figure 6.3 Rendering colors by nanopixels

(a-c) The bright-field optical micrographs of the checkerboard patterned metasurface and the enlarged SEM images in the region of the red box. Each square red box in the checkerboard has a side of (a) 1.25 μm (b) 0.75 μm and (c) 0.5 μm and consists of an array of (a), 5×5 (b), 3×3 and (c), 2×2 nanoantenna unit cells. (d) Simulated colors from infinite nanoantenna arrays (line 1), photographed images from 5×5 nanoantennas (line 2), 3×3 nanoantennas (line 3) and 2×2 nanoantennas (line 4). The corresponding analyzer angles are marked below; the polarizer angle is fixed at 45°.

Remarkably, Figure 6.3(c) shows that nanopixels with only 2 × 2 nanoantennas can exhibit vibrant alternating black-and-blue dots. The total area of such a nanopixel is 500 × 500 nm^2, which is equivalent to a spatial resolution of around 50,000 dots per inch (dpi) and exceeds the reported values in the most recent literature[318]–[323]. This effect originates from the LSPR's high field confinement at the nanoantenna/air interface. By rotating the analyzer but fixing the polarizer at 45° with respect to the *x*-direction, more colors are expected to reflect from each nanopixel according to previous analysis. Interestingly, Figure 6.3(d) shows that eight different colors (see the regions enclosed by the red boxes) are observed by photographing the checkerboard pattern with a 100× and 0.9 NA objective. These images agree well with the simulated colors, implying

that such an APM exhibits significant viewing angle tolerance and large data storage potential with 500×500 nm^2 nanopixels.

6.2.4 High-density data storage

Owing to the high spatial resolution and great diversity in color generation, our APM can be used to augment current data storage technology. In conventional data storage devices, a storage unit accommodates only a single bit of information (0 or 1). With our APM, however, information is stored in the orientation of the nanoantennas and is retrieved by a set at of analyzers acquiring color sequences that uniquely match the nanoantenna orientations. Since a large variety of distinguishable colors can be rendered by rotating the nanoantennas, the amount of information stored in one APM storage unit can greatly surpass a single bit. In our proof-of-concept demonstration, we utilize eight nanoantenna orientations evenly distributed between 0 and $\frac{7\pi}{8}$ to represent eight distinct information states, which can be regarded as three bits of information with each nanoantenna orientation representing 000, 001, 010, 011, 100, 101, 110, or 111. Consequently, an APM can be programmed by EBL with nanopixels being the fundamental storage units each carrying 3-bit information. From the experimental result of the previous section, the nanopixels can be as small as 500×500 nm^2 (2×2 nanoantennas, or unit cells) in order to render distinguishable neighboring colors. Then, the storage density of the proposed APM (3 bits per 500×500 nm^2) is calculated to be 5% larger than that of the state-of-the-art Blu-ray technology (~1 bit per 320×274 nm^2, the dimensions of a Blu-ray bit are estimated from[324]). An example of such data-storage APM is shown in Figure 6.4(a).

To translate the APM's antenna orientations into binary information, we propose a set of color codes that link the nanoantenna-rendered colors with the designated binary states, as well as a parallel-processing data readout system. Figure 6.4(b) presents the experimentally-obtained color codes (see more details on the color code generation in Supplementary Figure 6.7). The figure shows that a given nanoantenna orientation renders a unique color sequence when sequentially imaged with analyzer angles of 0°, 45°, 90° and 135° (with the polarizer fixed at 45°). The core idea here is that a 3-bit code is assigned to each nanoantenna orientation state and then retrieved from the corresponding color sequence with an imaging system.

The readout system consists of four white-light sources and four CCD cameras as shown in Figure 6.4(c). All four white-light sources are linearly polarized to 45° and illuminate adjacent

regions on the pre-programmed APM. Each illuminated region, hereafter referred to as *a frame*, may contain multiple nanopixels. For example, the frame shown in Figure 6.4(a) contains 16 nanopixels. CCD cameras record the rendered colors from the frame (each nanopixel in a frame may render a different color) after passing through four respective analyzers at angles mentioned above, and a local cache stores the color information on each nanopixel at each analyzer. Next time, when the array of frames moves forward by the length of one frame, the given frame is imaged at the next analyzer angle. When the frame passes all four CCD cameras, its constituent nanoantenna orientations, thereby stored data, is retrieved by looking up their color codes – the cache-stored color sequence. The four CCD images in Figure 6.4(c) are the color maps of the *single* frame shown in Figure 6.4(a) (also highlighted by the red box in Figure 6.4(c)), imaged under the four different analyzers.

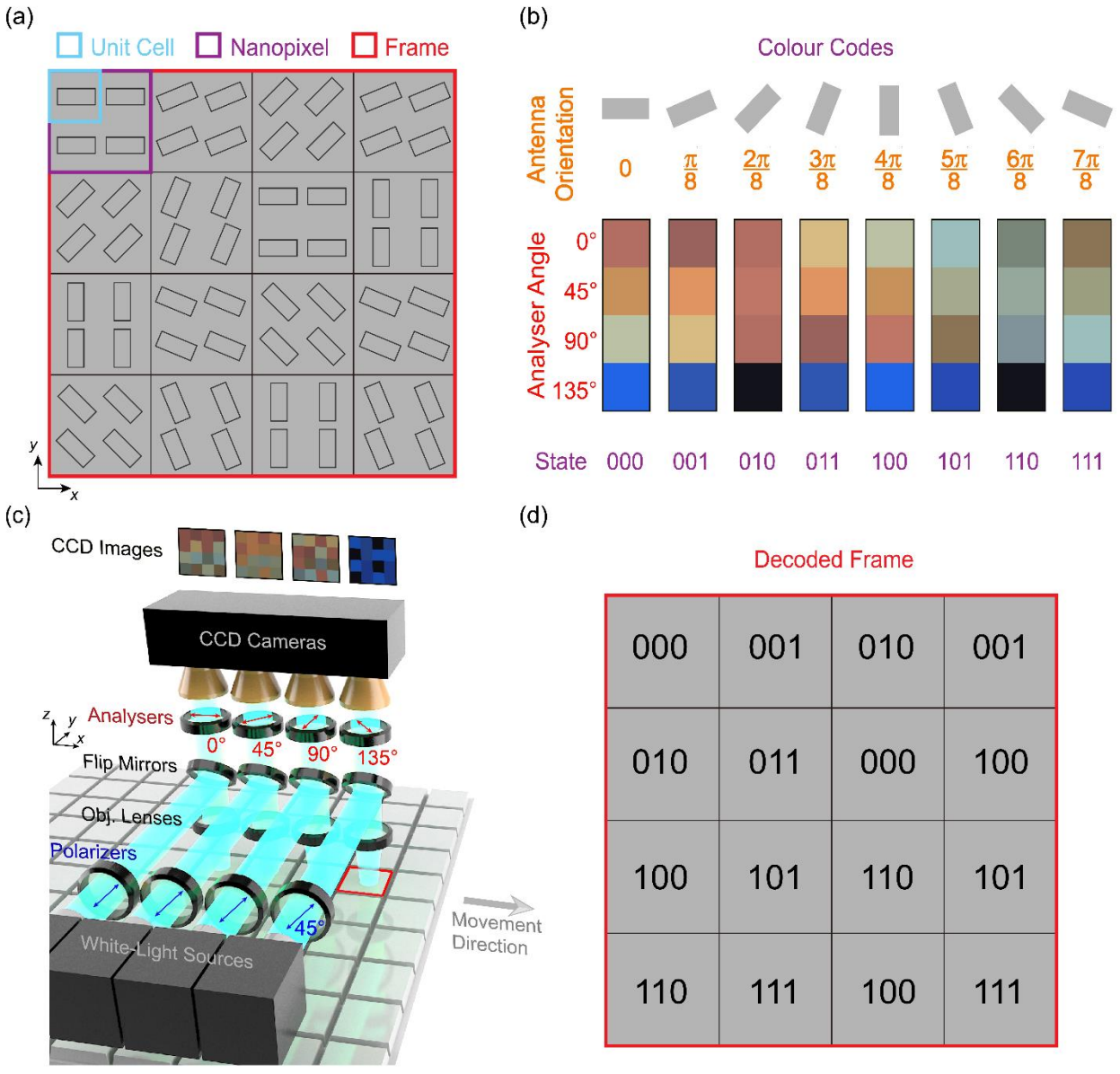

Figure 6.4 APM as a data storage device

(a) A frame (red box) of a data-storage APM containing 16 nanopixels (the purple box highlights *one* nanopixel), each consisting of 4 unit cells (the blue box highlights *one* unit cell). A *nanopixel* serves as an indivisible data storage unit, which accommodates 3 bits of information. (b) A unique color code is created for each nanoantenna orientation, which is then assigned a 3-bit information state, so that a 3-bit information can be stored in a nanopixel. (c) The schematic of a proposed imaging system for speedy APM information readout, which consists of four white-light sources, four CCD cameras and a sample-moving stage. The region highlighted by the red box shows the APM frame in (a), and the four CCD images show the color maps of this frame imaged under the four respective analyzers. (d) The stored binary data in (a) is retrieved after comparing the color sequence on each nanopixel and the color codes in (c).

Consequently, the color sequence on each nanopixel can be obtained to retrieve the binary data stored in the frame, as shown in Figure 6.4(d). The detailed data retrieval procedure is

presented in Supplementary Figure 6.8; the same procedure is applied to all frames of the APM to read the complete information. The advantage of the proposed readout scheme becomes apparent when the readout speed is considered. It takes 4X steps and a rotating analyzer for a setup with one light source and one camera to complete reading the information in one APM, where X is the number of frames in the APM; whereas only X + 3 steps are needed with the proposed parallel-processing setup, which also eliminates the need for a rotating analyzer. As we show in Supplementary Information Section 6.4.5, with ultra-high speed cameras (e.g. iX Camera i-SPEED 726) and other Blu-ray-equivalent components, it is possible to achieve a data readout speed of 18.3 Gbits/s, 143 times higher than the Blu-ray technology. It is worth noting that in the proposed readout scheme, the illuminating light need not be focused on one nanopixel, but instead enhances the readout speed by covering multiple nanopixels, provided that the color on each nanopixel can be spatially resolved by the CCD cameras (in this case, at each analyzer angle the cache stores a map of color pixels each corresponding to a nanopixel, as shown by the CCD images in Figure 6.4(c)).

The four-analyzer scheme used in the retrieval protocol is redundant for a 3-bit APM. Theoretically, even two analyzer angles are already sufficient to generate color codes that uniquely correspond to a nanoantenna orientation (it can be also observed from Figure 6.4(b), e.g., 0° and 90° analyzers). However, the redundancy is beneficial here; it can be used for error correction, hence enabling more robust information retrieval. Below we demonstrate the use of the four-analyzer scheme with more advanced APMs beyond 3 bits per nanopixel. Indeed, the data storage density in our APM can be further increased and is ultimately restricted by the CCD spectral resolution. We choose eight nanoantenna orientations in our experiment because the colors generated from these nanoantennas are easily distinguishable by the naked eye. Nonetheless, we show with simulation (see Supplementary Figure 6.9) that 4-bit information can be reliably stored in a single nanopixel using 16 different orientation states ranging from 0 to $\frac{15\pi}{16}$. In this case, the storage density increases to 40% higher than a conventional Blu-ray disc, and the readout speed increases to 191 times greater. As shown in this example, to increase the storage capacity per nanopixel in the APM, one needs only to utilize more nanoantenna orientations while keeping the nanoantenna geometry and the nanopixel size unchanged. In contrast to this, for the structures built on changing topologies (see e.g., ref[39]), the topological complexity significantly increases with storage density, and the structure needs to be enlarged to compensate for fabrication limitations.

We may comment that implementing machine learning for color or spectral recognition[39] along with multiplayer storage system[325], [326] are also viable steps towards further increasing the storage density while maintaining high readout accuracy. The potential in enhancing the data storage capacity and readout speed offered by our APM is a critical advancement in the area of optical data storage technology.

6.2.5 Optical information encryption

The checkerboard pattern shown in the SEM image of Figure 6.3(a) can also be used in information encryption applications. In this context, the structure with four alternating nanoantenna orientations is regarded as a ciphertext. As shown in Figure 6.5(a), when the ciphertext is imaged under 26 different polarizer-analyzer combinations, distinct color patterns can be obtained to represent the entire English alphabet. In order to attain the large variety of color patterns, the polarizer and analyzer angles are no longer limited to integer multiples of 45° but are chosen to optimize the distinguishability between patterns, and are used as keys to decrypt the information. As an example, in Figure 6.5(b) we show that when the ciphertext and two different key sets are sent to two recipients, different color patterns are perceived, from which one reads YES whereas the other reads OUT.

Although they are based on the same APM design, our proposed data storage and information encryption schemes are fundamentally different. In a data storage device, an APM needs to be pre-programmed to possess various nanopixels, and an invariant system acquires the information. In an information encryption system, the ciphertext is invariant, and various decryption key sets reveal the information.

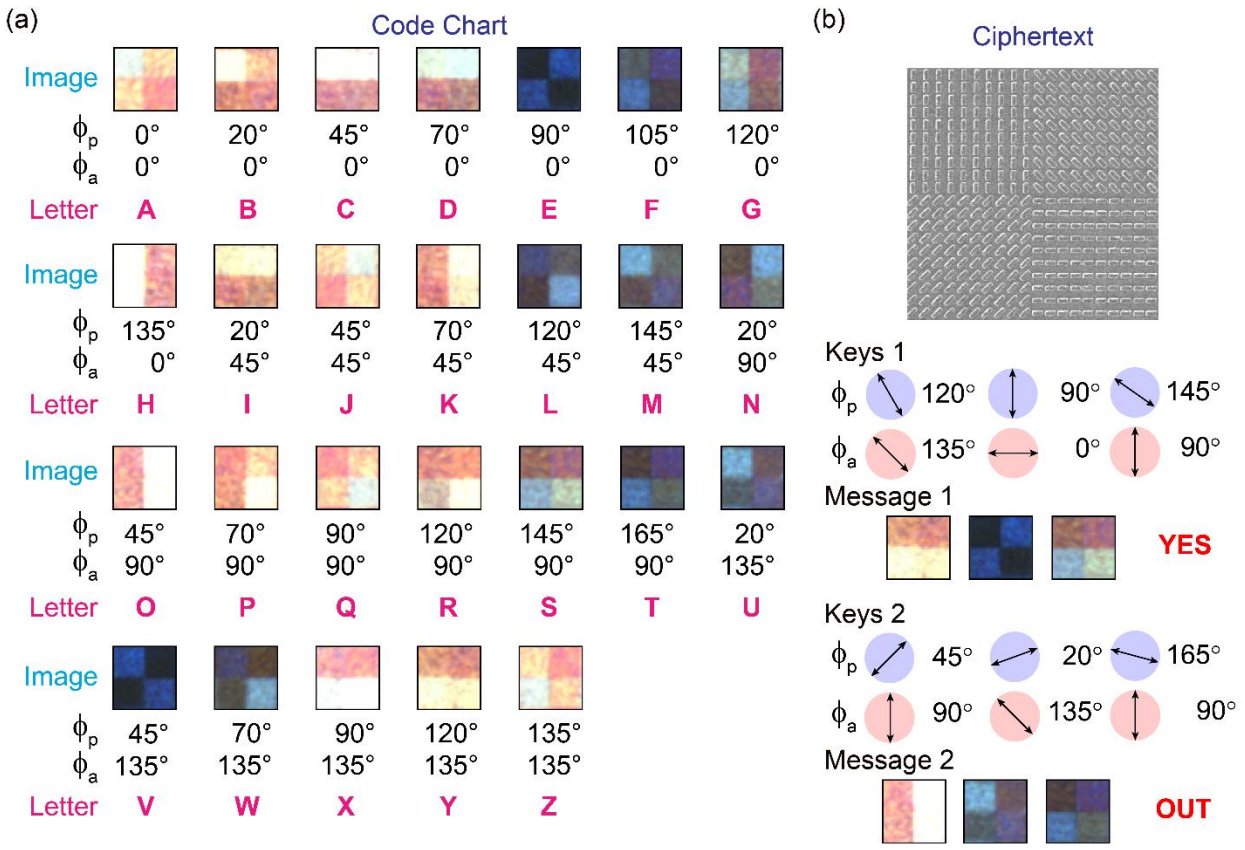

Figure 6.5 APM as an information encryption device

(a) Code chart of the color patterns when a ciphertext APM is photographed with white light under 26 polarizer (ϕ_p) and analyzer (ϕ_a) combinations, each representing a letter in the English alphabet. The polarizer and analyzer angles are used as decryption keys. (b) SEM of the ciphertext APM, and the different messages decrypted (YES and OUT) from the ciphertext by two sets of decryption keys.

6.3 Discussion

We propose a metasurface platform based on plasmonic color to realize three major functionalities in information technology – steganography, optical data storage, and encryption. With the metasurface, we demonstrate polarization-tunable colors in areas of 500 × 500 nm^2, presenting ~50,000 dpi resolution. The great color diversity leads to a judiciously designed optical steganography with vivid colors, abated "cross-talk" effect, and swift tuning. When used in optical data storage, such APM maintains the advantages of Blu-ray discs such as high durability (data are stored on physically-stable APM), low cost of operation (zero power consumption in idle state), and high data security/authenticity (stored data are immune to magnetic fields and cannot be

altered). However, paired with the novel multiple-bit data storage scheme, our APM surpasses Blu-ray disc technology in both storage density and readout speed. Additionally, the metasurface is also used as a tool for information encryption, and multiple combinations of polarizer and analyzer angles are used as keys to decrypt the text phrases. These outstanding results are achieved without using disc-hole array constructions[327] which are fabrication-challenging and increase the thickness of the filter.

Besides the small dimension of the pixel size, the fact that both polarizer and analyzer contribute to the optical response is essential. This feature not only presents the opportunity to erase, restore and tune the color image encoded in a common area but also improves the quality of imaging by abating the "cross-talk" effect which usually occurs in polarization-tunable color-producing structures[328]. Catalytic magnesium metasurface provides an alternative approach to tune the color[35], [299], however, the chemical reaction slows down the tuning speed and the nested lithography limits the diversity of the information codes. In contrast to the known "five-dimensional" data storage technique[326], our metasurface can selectively generate different information without causing any deformation to the nanoantennas, therefore are more robust for read-only data storage applications.

In summary, we design and experimentally demonstrate a versatile plasmonic color metasurface with a surface-relief Al film, which is used in advanced optical steganography, data storage, and encryption via tuning of reflected colors by rotating a polarizer and an analyzer. Employing the localized surface plasmon mode allows us to achieve a very high spatial resolution in the experiment. Based on the great color variability and high spatial resolution, we create and experimentally demonstrate an original technique to store multiple-bit information with the nanoantenna orientation states and retrieve this information using unique color codes. With this technique, the storage density already exceeds that of a conventional Blu-ray disc technology. Specially arranged analyzers enable a parallel data readout that outperforms traditional data readout system in operation speed. In addition, we utilize the tunable colors to realize advanced optical steganography and encryption. The proposed approach offers a wide range of tunable colors without causing any deformation to the structure, thus demonstrating great potential in advanced dynamic color applications.

6.4 Supplementary information

6.4.1 Experimental setup for photographing the APMs

Figure 6.6 illustrates the working principle of the APM. Optically broadband LP light is obtained from a halogen lamp with a broadband linear polarizer (Polarizer, Figure 6.6). A beam splitter guides the incident LP light to the APM, and the reflected light to a chromatic camera. Since the APM leads to the occurrence of dispersive optical-rotation effect (see the main text), a distinct reflectance spectrum is observed for each rotation state of the analyzer (Analyzer, Figure 6.6) – yet another broadband linear polarizer. In our experiment, we use the microscope Nikon Eclipse 80i, and LV-LH50PC HALOGEN 12V50W as the halogen lamp for illumination.

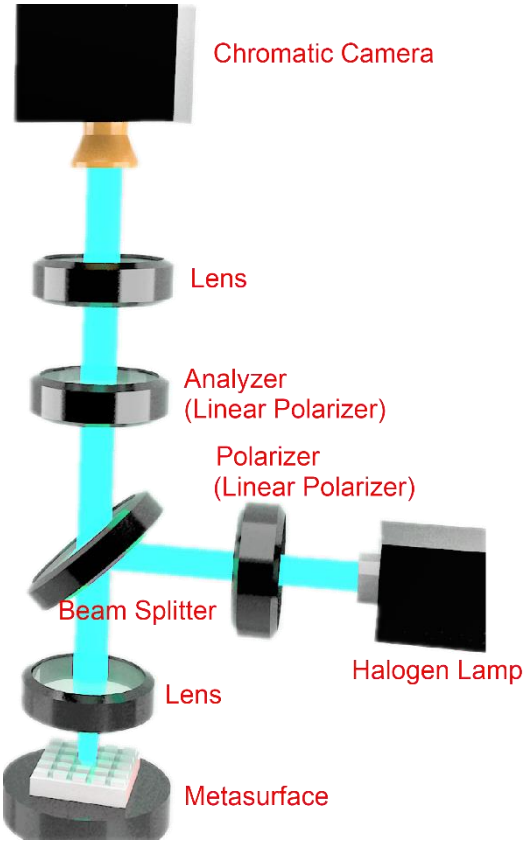

Figure 6.6 Experimental setup for photographing the APMs

Two broadband linear polarizers, Analyzer and Polarizer, which cover the visible region (380 nm – 780 nm), and a chromatic camera are integrated with a microscopic setup to image colors reflected from the APM under various Analyzer and Polarizer combinations. The halogen lamp is a broadband white light source.

6.4.2 Color codes for the data storage initial experimental validation

In this section, we present the method to generate the color codes (Figure 6.4(b) of the main text) that are used to retrieve information from the APM. We fabricate a wheel pattern containing the eight nanoantenna orientations and image the wheel using four analyzer rotation states (0°, 45°, 90°, 135°) with the polarizer rotation angle fixed at 45°.

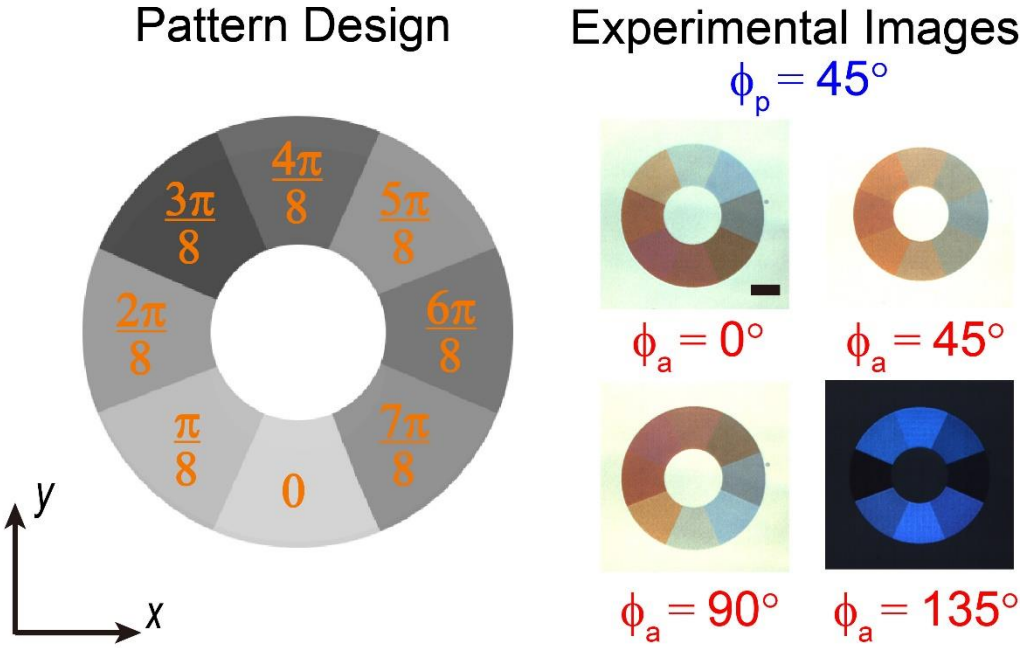

Figure 6.7 Experimental color codes generation

Left panel: The designed pattern is a wheel consisting of eight equal segments, each occupied by nanoantennas with the orientation marked by the orange-colored numbers. Right panel: the photographed images under four analyzer angles with polarizer fixed at 45°. The diverse colors from all eight segments under each analyzer angle are picked to construct the color codes in Figure 6.4(b) of the main text.

Figure 6.7 shows the wheel pattern design and the experimentally obtained images. Each nanoantenna orientation state renders a different color at a given analyzer rotation angle, thus allowing us to construct a color code sequence for each nanoantenna orientation examined with four analyzer states, as shown in Figure 6.4(b) of the main text. Assigning an individual 3-bit information state to each 4-color code, we, therefore, establish a unique correspondence between the nanoantenna orientation state and the 3-bit information. As discussed in the main text, the redundancy in analyzer angles is conducive to more robust data readout and is suitable for more advanced APM data storage systems (see Section 6.4.4 of Supplementary Information).

6.4.3 Reading APM stored information

This section uses an example to illustrate how the binary information stored in a single APM nanopixel is read out using the setup in Figure 6.4(c) of the main text. A nanopixel with the nanoantenna orientation state of $\frac{\pi}{8}$ is first imaged with 0°-analyzer – the camera records a maroon color (Figure 6.8(a)). As the sample moves, the sample nanopixel is then sequentially imaged with analyzers at 45°, 90°, and 135° rotation states, so that orange, beige, and blue colors are acquired by the camera, respectively (Figures 6.8(b-d)). During the entire imaging process, the rotation state of polarizer is fixed at 45°. A local cache stores the maroon-orange-beige-blue 4-color sequence from the given nanopixel, and looks it up in the color codes (Figure 6.8(b) of the main text), to retrieve a binary code of 001 stored in this nanopixel. Several nanopixels in a frame are imaged at once; therefore, the readout speed is significantly increased compared to the conventional single-point readout systems (see Supplementary Section 6.4.5).

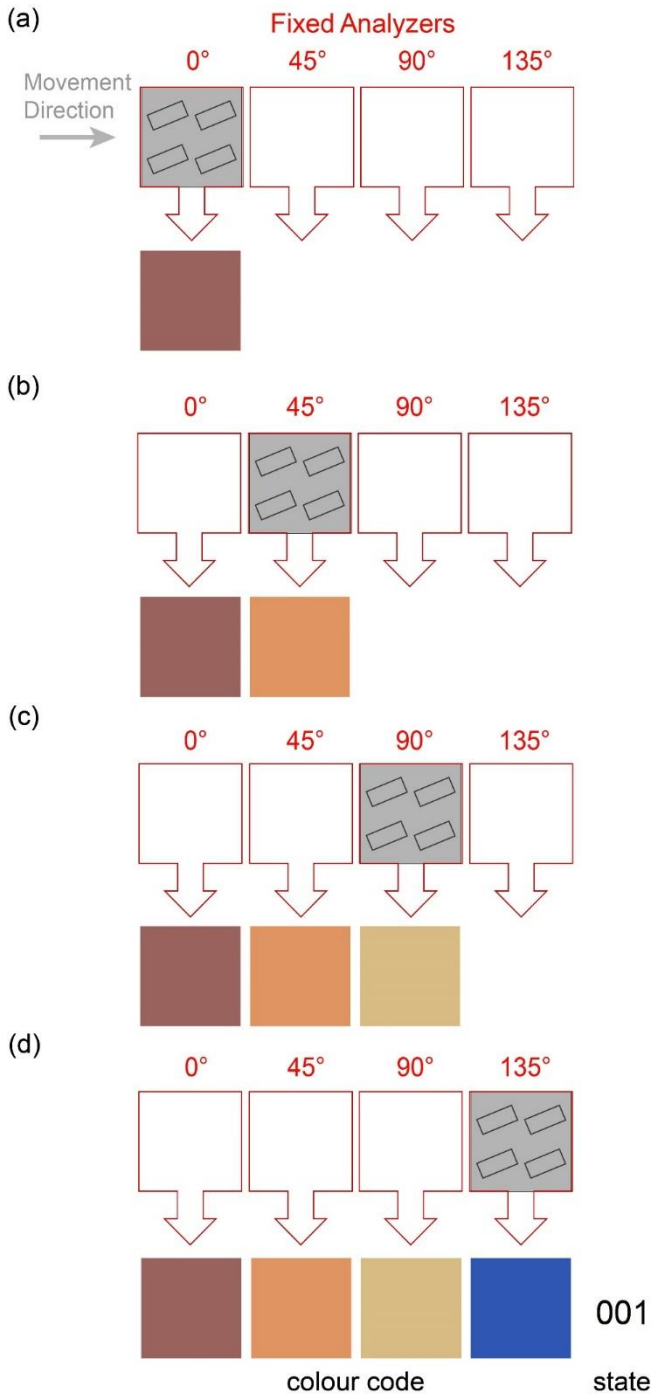

Figure 6.8 Reading binary information stored in an APM nanopixel

The nanopixel containing $\frac{\pi}{8}$-oriented nanoantennas is imaged with Analyzer at 0°, 45°, 90° and 135° rotation states, respectively, and renders maroon (a), orange (b), beige (c), and blue (d) colors. The color sequence in (d) is matched with the look-up table of Figure 6.4(b) in the main text, to retrieve the binary code 001.

6.4.4 Enhanced data storage capacity

As stated in the main text, our APM can be used in data storage applications where the information is stored in the nanoantenna orientation states. In the main text, we demonstrate the concept using eight nanoantenna orientations experimentally – the photographed colors generated from these orientations are easily distinguishable even by the naked eye. Here, we show with a numerical simulation that the data storage capacity can be further enhanced by utilizing 16 different nanoantenna orientations, so that each orientation can represent a 4-bit word (a tetrad), thereby doubling the data storage capacity compared to the demonstration in the main text. Figure 6.9 shows the simulated color codes of the 16 nanoantenna orientation states obtained with the four analyzer rotation states (0°, 45°, 90°, 135°) at a fixed polarizer angle of 45°. It can be concluded that the 16-color sequences uniquely represent the nanoantenna orientation states, therefore, can be used to retrieve the corresponding information states. It is to be noted, however, that as the data storage capacity increases, some of the color sequences become indiscernible by the naked eye. Improving the robust read-out may require (i) a higher spectral resolution of the camera, (ii) optimization of the angular states of both antennas and analyzer, and (iii) the use of the overdetermined number of the analyzer rotation states (as we already do for the 3-bit states in the main text).

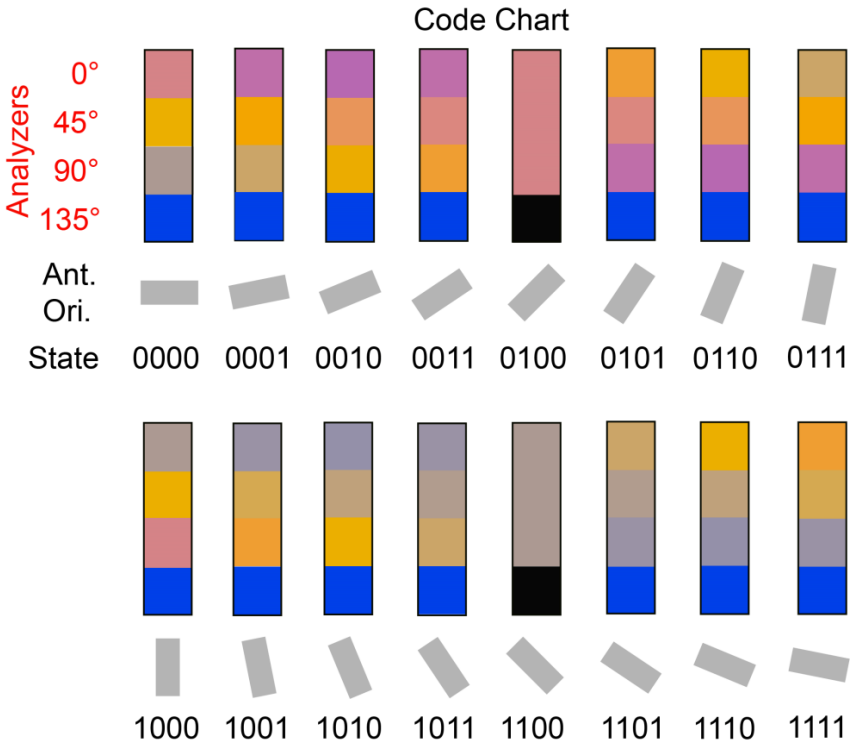

Figure 6.9 Simulated 4-color sequences encoding 4 bits of information (16 states)

The nanoantenna orientation states change from 00 to $\frac{15\pi}{16}$ with a step of $\frac{\pi}{16}$. The code chart shows that the reflected 4-color sequences obtained with analyzers with four rotation states (0°, 45°, 90°, 135°) uniquely match the nanoantenna orientation states. The experimental setup is identical to the setup shown in Figure 6.4(c) of the main text.

6.4.5 The estimate of data readout speed

In this section, we discuss the theoretical limit of the data readout speed using the system shown in Figure 6.4 of the main text. In the following calculations, we consider a 3-bit APM, i.e. each nanopixel of area 500 × 500 nm^2 stores 3 bits of information. The data readout system is an image-based parallel processing system, meaning that all the information in a frame (see main text for the definition of a frame) can be retrieved at once by taking an image of the frame. As a result, the factors to consider regarding the readout speed are: 1. The number of bits per frame; 2. The time required for a camera to take an image of the frame; 3. The time required for the translational stage or disc spinner to move from one frame to another. In the following, we first calculate the three factors, respectively, and then obtain the readout speed by combining them.

1. The number of bits per frame: The frame area is mainly limited by the field of view of the objective lens. In our experiment, we use an objective lens with a field of view (diameter) of 0.18 mm, which means the maximum frame area is

$$A_{frame} = \pi\left(\frac{1}{2}D_{frame}\right)^2 = \pi\left(\frac{1}{2}0.18\text{ mm}\right)^2 = 2.54\times10^{-8}\text{ m}^2$$

and the number of nanopixels in each frame is $N_{np} = \frac{A_{frame}}{A_{np}} = \frac{2.54\times10^{-8}\text{ m}^2}{(500\text{ nm})^2} = 10^5$

Since each nanopixel stores 3 bits of information, the number of bits stored in one frame is $N_{bits} = 3N_{np} = 3\times10^5$.

2. The Frame Read-out Time: a high-speed color camera (e.g. iX Camera i-SPEED 726) is capable of taking images with a resolution of 1064×102 (108,528 pixels, enough to image the 10^5 nanopixels in one frame) at a speed of 200,000 frames per second (FPS). Therefore, the time required to take one color image with high enough resolution is

$$t_{camera} = \frac{1}{FPS} = \frac{1}{200000\text{ s}^{-1}} = 5\times10^{-6}\text{ s}.$$

3. Time required for the translational stage or disc spinner to move from one frame to another: In this calculation, we assume a disc spinner with a spinning speed of 5,000 RPM (or 523.6 rad/s) and an APM disc of radius 60 mm (same as a Blu-ray disc). Since the linear velocity varies at different radii, we take an average radius of 30 mm, giving a linear velocity of

$$v_{lin} = \omega R_{disc} = 523.6\,\text{rad/s}\times30\text{ mm} = 15.71\text{ m/s}.$$

Therefore, the time required to move from one frame to another is

$$t_{spin} = \frac{D_{frame}}{v_{lin}} = \frac{0.18\text{ mm}}{15.71\text{ m/s}} = 1.14\times10^{-5}\text{ s}.$$

Combining the results of 1, 2 and 3, the data readout speed of our proposed system is

$$\rho_{APM} = \frac{N_{bits}}{t_{camera}+t_{spin}} = \frac{3\times10^5\text{ bits}}{5\times10^{-6}\text{ s}+1.14\times10^{-5}\text{ s}} = 1.83\times10^{10}\text{ bits/s},$$

or 18.3 Gbits/s. Compare with the maximum data readout speed of 128 Mbits/s in Blu-ray discs[324], and our system shows a readout speed that is *143 times faster*.

We note that although a frame needs to pass four cameras to have its information retrieved, the time required to read information from one frame is *not* multiplied by four. This multiplication is not required because we implement the parallel data acquisition with four cameras in the readout

setup, which take X + 3 images to read the information from a given APM, with X being the number of frames in the APM (see analysis in main text). As X gets large enough, X + 3 can be well approximated by X, effectively representing the case of taking *a single image per frame*.

6.4.6 Dielectric permittivity of Al

During fabrication, we use an unpatterned sample to grow Al under the same conditions as the APM sample and characterize the dielectric permittivity of Al using this sample with a Variable-Angle Spectroscopic Ellipsometer, VASE (J. A. Woollam Co., W-VASE). Figure 6.10 shows the permittivity data fitted by a dispersive material model with one Drude term and three Lorentz oscillator terms,

$$\bar{\varepsilon}(h\nu) = \varepsilon_1 + i\varepsilon_2 = \varepsilon_{1\infty} + \sum\nolimits_k \frac{A_k}{\varepsilon_k^2 - (h\nu)^2 - iB_k h\nu}$$

For k^{th} oscillator, A_k is the amplitude, E_k is the center energy, and B_k is the broadening of the oscillator. $h\nu$ is the photon energy in eV, $\varepsilon_{1\infty}$ is an additional offset term. In our fitting for Al permittivity, $\varepsilon_{1\infty} = 1.4842$, and the other parameters are listed in Table 6.1:

Table 6.1 Drude-Lorentz fitting parameters for Al film

k	A (eV^2)	B (eV)	E (eV)
1*	141.60	0.13445	0
2	8.8166	0.30195	1.5293
3	9.9312	0.61558	1.7383
4	20.048	1.9767	2.0991

* The Drude term

This experiment-based Drude-Lorentz model is used in all numerical simulations presented in this work.

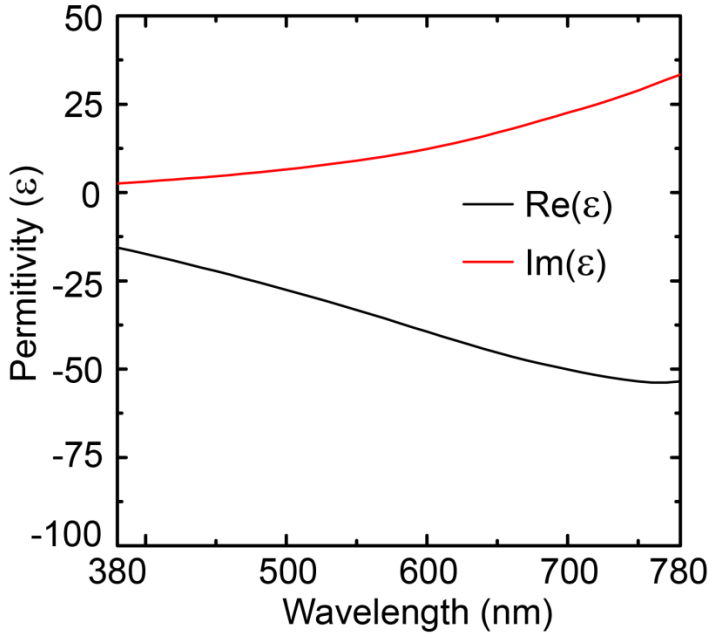

Figure 6.10 Real (black) and imaginary (red) parts of the measured Al dielectric function

7. CONCLUSIONS AND OUTLOOK

In this dissertation, I have summarized my efforts in creating a number of metasurfaces with highly diversified functionalities: building plasmon resonators, enhancing photodetector performance (with fractal metasurface and gap plasmon metasurface, respectively), enabling thermoplasmonic characterization, generating tunable nanoscale colors, and augmenting the current data storage technology. Besides these, I would like to name two works that are not included in this dissertation: accelerating light beam and on-chip synchrotron radiation enabled by metasurface. These two works were led by R. Merlin group at University of Michigan, and I fabricated two metasurfaces that can bend light to propagate in curved trajectories with radii of curvature from 100 to 400 μm. Specifically, in the on-chip synchrotron radiation work, we successfully "emulated" a spiraling electron with an optical pulse, and probed the evolution of the nonlinear polarization that is generated from this pulse, which is analogous to the synchrotron radiation from a spiraling electron traveling at a speed 3 times faster than the speed of light. I would recommend the readers refer to *Henstridge et al., Optica 5 (6), 678-681, 2018*, and *Henstridge et al., Science 362 (6413), 439-442, 2018* for these two works.

One important aspect of metasurface's major applications that is not covered in my PhD research is metalenses. Metalenses are a group of metasurfaces specially designed to replace the conventional bulky optics for imaging applications, they achieve light focusing by imparting appropriate optical phase discontinuities at a pixelated surface. Since arbitrary phase discontinuity can be provided by chosen optical elements, besides being ultimately thin, well-engineered metalenses often exhibit better performances than conventional bulky optics, such as reduced aberration and large numerical aperture. The metalenses, and other functional metasurfaces, are discussed in detail in a review article that I contributed to writing, and can be found in *Choudhury et al., Nanophotonics 7 (6), 959-987, 2018*.

Following intense research activities, metasurfaces are now starting to make way to commercialization. Some start-ups, as well as several industry-leading companies, have started investigating using metasurfaces in imaging, display, vision protection, augmented/virtual reality, and solar energy harvesting. A bright future is promised for metasurfaces, yet challenges persist. To date, most metasurfaces are designed empirically thus the performances are not necessarily

optimized. To address this problem, research efforts are burgeoning towards metasurface optimization using machine learning techniques. If successful, such techniques would require much less human input and deliver more enhanced results. However, as my advisor Dr. Vladimir M. Shalaev has pointed out, the most valuable asset of an elite physicist (or engineer) is his/her keen intuition, which is acquired via intense knowledge accumulation, and constitute the "little" human input to the machine-learning optimization process that makes a huge difference in the optimization time and final output. So, as of now, for researchers and scientists in this field, there is little need to worry about being outperformed and replaced by machines.

Finally, I would like to acknowledge that my achievements are made possible by the pioneers in the field of optics and photonics prior to me, whose dedications created a world of unimaginable marvels, simply from four equations written down by James Clerk Maxwell and one by Erwin Rudolf Josef Alexander Schrödinger. I hereby present my utmost respect for those who elegantly summarize the hidden mechanics that govern the progression of the universe and everything within it, as well as to those who wield such mechanics to do general good. I wish my discoveries would be deemed instrumental and inspirational by some that come after.

REFERENCES

[1] R. Adato and H. Altug, "In-situ ultra-sensitive infrared absorption spectroscopy of biomolecule interactions in real time with plasmonic nanoantennas.," *Nat. Commun.*, vol. 4, p. 2154, 2013.

[2] D. Rodrigo *et al.*, "Mid-infrared plasmonic biosensing with graphene," *Science*, vol. 349, no. 6244, pp. 165–168, Jul. 2015.

[3] A. Naldoni *et al.*, "Broadband Hot-Electron Collection for Solar Water Splitting with Plasmonic Titanium Nitride," *Adv. Opt. Mater.*, vol. 5, no. 15, p. 1601031, Aug. 2017.

[4] S. Ishii, R. P. Sugavaneshwar, and T. Nagao, "Titanium Nitride Nanoparticles as Plasmonic Solar Heat Transducers," *J. Phys. Chem. C*, vol. 120, no. 4, pp. 2343–2348, Feb. 2016.

[5] G. Baffou and R. Quidant, "Thermo-plasmonics: using metallic nanostructures as nano-sources of heat," *Laser Photon. Rev.*, vol. 7, no. 2, pp. 171–187, Mar. 2013.

[6] A. Pospischil, M. M. Furchi, and T. Mueller, "Solar-energy conversion and light emission in an atomic monolayer p–n diode," *Nat. Nanotechnol.*, vol. 9, no. 4, pp. 257–261, 2014.

[7] K. Jain and B. J. Lin, "Ultrafast Deep UV Lithography with Excimer Lasers," *IEEE Electron Device Lett.*, vol. 3, no. 3, pp. 53–55, 1982.

[8] J. C. Ndukaife, A. V. Kildishev, A. G. A. Nnanna, V. M. Shalaev, S. T. Wereley, and A. Boltasseva, "Long-range and rapid transport of individual nano-objects by a hybrid electrothermoplasmonic nanotweezer," *Nat. Nanotechnol.*, vol. 11, no. 1, pp. 53–59, Jan. 2016.

[9] V. E. Babicheva *et al.*, "Towards CMOS-compatible nanophotonics: Ultra-compact modulators using alternative plasmonic materials," *Opt. Express*, vol. 21, no. 22, p. 27326, 2013.

[10] N. Kinsey, C. DeVault, J. Kim, M. Ferrera, V. M. Shalaev, and A. Boltasseva, "Epsilon-near-zero Al-doped ZnO for ultrafast switching at telecom wavelengths," *Optica*, vol. 2, no. 7, p. 616, 2015.

[11] M. A. Nielsen and I. L. Chuang, *Quantum Computation and Quantum Information*. 2010.

[12] S. Bogdanov *et al.*, "Electron spin contrast of Purcell-enhanced nitrogen-vacancy ensembles in nanodiamonds," *Phys. Rev. B*, vol. 96, no. 3, 2017.

[13] S. Bogdanov, M. Y. Shalaginov, A. Boltasseva, and V. M. Shalaev, "Material platforms for integrated quantum photonics," *Opt. Mater. Express*, vol. 7, no. 1, p. 111, 2017.

[14] P. Neumann *et al.*, "Multipartite Entanglement Among Single Spins in Diamond," *Science*, vol. 320, no. 5881, pp. 1326–1329, 2008.

[15] M. Born and E. Wolf, *Principles of Optics*. Cambridge: Cambridge University Press, 1999.

[16] J. B. Pendry, "Negative Refraction Makes a Perfect Lens," *Phys. Rev. Lett.*, vol. 85, no. 18, pp. 3966–3969, Oct. 2000.

[17] M. L. Brongersma and V. M. Shalaev, "The Case for Plasmonics," *Science*, vol. 328, no. 5977, pp. 440–441, Apr. 2010.

[18] N. K. Emani, A. V. Kildishev, V. M. Shalaev, and A. Boltasseva, "Graphene: A Dynamic Platform for Electrical Control of Plasmonic Resonance," *Nanophotonics*, vol. 4, no. 1, pp. 214–223, Jan. 2015.

[19] S. M. Choudhury *et al.*, "Material platforms for optical metasurfaces," *Nanophotonics*, vol. 7, no. 6, pp. 959–987, Jun. 2018.

[20] N. Yu and F. Capasso, "Flat optics with designer metasurfaces," *Nat. Mater.*, vol. 13, no. 2, pp. 139–150, Jan. 2014.

[21] I. Staude and J. Schilling, "Metamaterial-inspired silicon nanophotonics," *Nat. Photonics*, vol. 11, no. 5, pp. 274–284, Apr. 2017.

[22] N. Yu *et al.*, "Light Propagation with Phase Discontinuities: Generalized Laws of Reflection and Refraction," *Science*, vol. 334, no. 6054, pp. 333–337, Oct. 2011.

[23] X. Ni, N. K. Emani, A. V. Kildishev, A. Boltasseva, and V. M. Shalaev, "Broadband Light Bending with Plasmonic Nanoantennas," *Science*, vol. 335, no. 6067, pp. 427–427, Jan. 2012.

[24] M. Khorasaninejad, W. T. Chen, R. C. Devlin, J. Oh, A. Y. Zhu, and F. Capasso, "Metalenses at visible wavelengths: Diffraction-limited focusing and subwavelength resolution imaging," *Science*, vol. 352, no. 6290, pp. 1190–1194, Jun. 2016.

[25] F. Aieta, M. A. Kats, P. Genevet, and F. Capasso, "Multiwavelength achromatic metasurfaces by dispersive phase compensation," *Science*, vol. 347, no. 6228, pp. 1342–1345, Mar. 2015.

[26] S. Zhang *et al.*, "High efficiency near diffraction-limited mid-infrared flat lenses based on metasurface reflectarrays," *Opt. Express*, vol. 24, no. 16, p. 18024, Aug. 2016.

[27] W. T. Chen, A. Y. Zhu, M. Khorasaninejad, Z. Shi, V. Sanjeev, and F. Capasso, "Immersion Meta-Lenses at Visible Wavelengths for Nanoscale Imaging," *Nano Lett.*, vol. 17, no. 5, pp. 3188–3194, May 2017.

[28] S. Choudhury, U. Guler, A. Shaltout, V. M. Shalaev, A. V. Kildishev, and A. Boltasseva, "Pancharatnam-Berry Phase Manipulating Metasurface for Visible Color Hologram Based on Low Loss Silver Thin Film," *Adv. Opt. Mater.*, vol. 5, no. 10, p. 1700196, May 2017.

[29] J. P. Balthasar Mueller, N. A. Rubin, R. C. Devlin, B. Groever, and F. Capasso, "Metasurface Polarization Optics: Independent Phase Control of Arbitrary Orthogonal States of Polarization," *Phys. Rev. Lett.*, vol. 118, no. 11, p. 113901, Mar. 2017.

[30] T. J. Echtermeyer *et al.*, "Strong plasmonic enhancement of photovoltage in graphene.," *Nat. Commun.*, vol. 2, p. 458, Jan. 2011.

[31] H. Jiang *et al.*, "Enhancing sensitivity to ambient refractive index with tunable few-layer graphene/hBN nanoribbons," *Photonics Res.*, vol. 7, no. 7, p. 815, Jul. 2019.

[32] H. Jiang *et al.*, "Modulating phase by metasurfaces with gated ultra-thin TiN films," *Nanoscale*, vol. 11, no. 23, pp. 11167–11172, 2019.

[33] H. A. Atwater and A. Polman, "Plasmonics for improved photovoltaic devices," *Nat. Mater.*, vol. 9, no. 3, pp. 205–213, Mar. 2010.

[34] O. Neumann, A. S. Urban, J. Day, S. Lal, P. Nordlander, and N. J. Halas, "Solar Vapor Generation Enabled by Nanoparticles," *ACS Nano*, vol. 7, no. 1, pp. 42–49, Jan. 2013.

[35] X. Duan, S. Kamin, and N. Liu, “Dynamic plasmonic colour display,” *Nat. Commun.*, vol. 8, p. 14606, Feb. 2017.

[36] X. Duan, S. Kamin, F. Sterl, H. Giessen, and N. Liu, “Hydrogen-Regulated Chiral Nanoplasmonics,” *Nano Lett.*, vol. 16, no. 2, pp. 1462–1466, Feb. 2016.

[37] P. Nyga *et al.*, “Laser-induced color printing on semicontinuous silver films: red, green and blue,” *Opt. Mater. Express*, vol. 9, no. 3, p. 1528, Mar. 2019.

[38] P. Zijlstra, J. W. M. Chon, and M. Gu, “Five-dimensional optical recording mediated by surface plasmons in gold nanorods,” *Nature*, vol. 459, no. 7245, pp. 410–413, May 2009.

[39] P. R. Wiecha, A. Lecestre, N. Mallet, and G. Larrieu, “Pushing the limits of optical information storage using deep learning,” *Nat. Nanotechnol.*, vol. 14, no. 3, pp. 237–244, Mar. 2019.

[40] K. A. Willets and R. P. Van Duyne, “Localized Surface Plasmon Resonance Spectroscopy and Sensing,” *Annu. Rev. Phys. Chem.*, vol. 58, no. 1, pp. 267–297, May 2007.

[41] S. Letokhov, “Generation of light by a scattering medium with negative resonance.,” *Sov. Phys. JETP*, vol. 26, no. 4, pp. 835–840, 1968.

[42] S. A. Maier, *Plasmonics: Fundamentals and Applications*. Boston, MA: Springer US, 2007.

[43] P. B. Johnson and R. W. Christy, “Optical Constants of the Noble Metals,” *Phys. Rev. B*, vol. 6, no. 12, pp. 4370–4379, Dec. 1972.

[44] A. K. Geim and K. S. Novoselov, “The rise of graphene,” *Nat. Mater.*, vol. 6, no. 3, pp. 183–191, Mar. 2007.

[45] K. S. Novoselov *et al.*, “Electric Field Effect in Atomically Thin Carbon Films,” *Science*, vol. 306, no. 5696, pp. 666–669, Oct. 2004.

[46] J. B. Khurgin, “How to deal with the loss in plasmonics and metamaterials,” *Nat. Nanotechnol.*, vol. 10, no. 1, pp. 2–6, Jan. 2015.

[47] W. T. Hsieh, P. C. Wu, J. B. Khurgin, D. P. Tsai, N. Liu, and G. Sun, “Comparative Analysis of Metals and Alternative Infrared Plasmonic Materials,” *ACS Photonics*, p. acsphotonics.7b01166, Oct. 2017.

[48] F. H. L. Koppens, D. E. Chang, and F. J. García de Abajo, “Graphene Plasmonics: A Platform for Strong Light–Matter Interactions,” *Nano Lett.*, vol. 11, no. 8, pp. 3370–3377, Aug. 2011.

[49] E. H. Hwang and S. Das Sarma, “Dielectric function, screening, and plasmons in two-dimensional graphene,” *Phys. Rev. B - Condens. Matter Mater. Phys.*, vol. 75, no. 20, pp. 1–6, 2007.

[50] M. Jablan, H. Buljan, and M. Soljačić, “Plasmonics in graphene at infrared frequencies,” *Phys. Rev. B*, vol. 80, no. 24, p. 245435, Dec. 2009.

[51] Z. Fei *et al.*, “Infrared Nanoscopy of Dirac Plasmons at the Graphene–SiO2 Interface,” *Nano Lett.*, vol. 11, no. 11, pp. 4701–4705, Nov. 2011.

[52] Z. Fei *et al.*, “Gate-tuning of graphene plasmons revealed by infrared nano-imaging,” *Nature*, vol. 487, no. 7405, pp. 82–85, Jun. 2012.

[53] J. Chen *et al.*, “Optical nano-imaging of gate-tunable graphene plasmons,” *Nature*, vol. 487, pp. 77–81, Jul. 2012.

[54] I. Silveiro, J. M. P. Ortega, and F. J. G. de Abajo, “Plasmon wave function of graphene nanoribbons,” *New J. Phys.*, vol. 17, no. 8, p. 083013, Aug. 2015.

[55] R. Yu, J. D. Cox, J. R. M. Saavedra, and F. J. García de Abajo, “Analytical Modeling of Graphene Plasmons,” *ACS Photonics*, p. acsphotonics.7b00740, Aug. 2017.

[56] F. J. García de Abajo, “Graphene Plasmonics: Challenges and Opportunities,” *ACS Photonics*, vol. 1, no. 3, pp. 135–152, Mar. 2014.

[57] V. W. Brar, M. S. Jang, M. Sherrott, J. J. Lopez, and H. A. Atwater, “Highly Confined Tunable Mid-Infrared Plasmonics in Graphene Nanoresonators,” *Nano Lett.*, vol. 13, no. 6, pp. 2541–2547, Jun. 2013.

[58] Z. Fang *et al.*, “Gated tunability and hybridization of localized plasmons in nanostructured graphene.,” *ACS Nano*, vol. 7, no. 3, pp. 2388–2395, Mar. 2013.

[59] H. Yan *et al.*, “Damping pathways of mid-infrared plasmons in graphene nanostructures,” *Nat. Photonics*, vol. 7, no. 5, pp. 394–399, Apr. 2013.

[60] J. H. Strait *et al.*, "Confined plasmons in graphene microstructures: Experiments and theory," *Phys. Rev. B*, vol. 87, no. 24, p. 241410, Jun. 2013.

[61] J. Christensen, A. Manjavacas, S. Thongrattanasiri, F. H. L. Koppens, and F. J. García de Abajo, "Graphene Plasmon Waveguiding and Hybridization in Individual and Paired Nanoribbons," *ACS Nano*, vol. 6, no. 1, pp. 431–440, Jan. 2012.

[62] T. Low and P. Avouris, "Graphene plasmonics for terahertz to mid-infrared applications.," *ACS Nano*, vol. 8, no. 2, pp. 1086–101, Feb. 2014.

[63] S. Thongrattanasiri, F. H. L. Koppens, and F. J. García de Abajo, "Complete Optical Absorption in Periodically Patterned Graphene," *Phys. Rev. Lett.*, vol. 108, no. 4, p. 047401, Jan. 2012.

[64] R. Yu, A. Manjavacas, and F. J. García de Abajo, "Ultrafast radiative heat transfer," *Nat. Commun.*, vol. 8, no. 1, p. 2, Dec. 2017.

[65] N. K. Emani, T.-F. Chung, X. Ni, A. V Kildishev, Y. P. Chen, and A. Boltasseva, "Electrically tunable damping of plasmonic resonances with graphene.," *Nano Lett.*, vol. 12, no. 10, pp. 5202–6, Oct. 2012.

[66] Y. Yao *et al.*, "Electrically Tunable Metasurface Perfect Absorbers for Ultrathin Mid-Infrared Optical Modulators," *Nano Lett.*, vol. 14, no. 11, pp. 6526–6532, Nov. 2014.

[67] Y. Yao *et al.*, "Broad Electrical Tuning of Graphene-Loaded Plasmonic Antennas," *Nano Lett.*, vol. 13, no. 3, pp. 1257–1264, Mar. 2013.

[68] Y. Yao *et al.*, "Wide wavelength tuning of optical antennas on graphene with nanosecond response time.," *Nano Lett.*, vol. 14, no. 1, pp. 214–9, Jan. 2014.

[69] S. H. Mousavi *et al.*, "Inductive Tuning of Fano-Resonant Metasurfaces Using Plasmonic Response of Graphene in the Mid-Infrared," *Nano Lett.*, vol. 13, no. 3, pp. 1111–1117, Mar. 2013.

[70] N. Dabidian *et al.*, "Electrical Switching of Infrared Light Using Graphene Integration with Plasmonic Fano Resonant Metasurfaces," *ACS Photonics*, vol. 2, no. 2, pp. 216–227, Feb. 2015.

[71] N. K. Emani, T.-F. Chung, A. V. Kildishev, V. M. Shalaev, Y. P. Chen, and A. Boltasseva, "Electrical Modulation of Fano Resonance in Plasmonic Nanostructures Using Graphene," *Nano Lett.*, vol. 14, no. 1, pp. 78–82, Jan. 2014.

[72] Y. Yao *et al.*, "High-Responsivity Mid-Infrared Graphene Detectors with Antenna-Enhanced Photocarrier Generation and Collection," *Nano Lett.*, vol. 14, no. 7, pp. 3749–3754, Jul. 2014.

[73] J. Fang *et al.*, "Enhanced Graphene Photodetector with Fractal Metasurface," *Nano Lett.*, vol. 17, no. 1, pp. 57–62, Jan. 2017.

[74] Y. Liu *et al.*, "Plasmon resonance enhanced multicolour photodetection by graphene," *Nat. Commun.*, vol. 2, p. 579, Dec. 2011.

[75] T. J. Echtermeyer *et al.*, "Surface Plasmon Polariton Graphene Photodetectors," *Nano Lett.*, vol. 16, no. 1, pp. 8–20, Jan. 2016.

[76] M. Freitag, T. Low, W. Zhu, H. Yan, F. Xia, and P. Avouris, "Photocurrent in graphene harnessed by tunable intrinsic plasmons," *Nat. Commun.*, vol. 4, p. 1951, Jun. 2013.

[77] S. Chakraborty, O. P. Marshall, T. G. Folland, Y.-J. Kim, A. N. Grigorenko, and K. S. Novoselov, "Gain modulation by graphene plasmons in aperiodic lattice lasers," *Science*, vol. 351, no. 6270, pp. 246–248, Jan. 2016.

[78] M. S. Jang *et al.*, "Tunable large resonant absorption in a midinfrared graphene Salisbury screen," *Phys. Rev. B*, vol. 90, no. 16, p. 165409, Oct. 2014.

[79] S. Kim, M. S. Jang, V. W. Brar, Y. Tolstova, K. W. Mauser, and H. A. Atwater, "Electronically tunable extraordinary optical transmission in graphene plasmonic ribbons coupled to subwavelength metallic slit arrays," *Nat. Commun.*, vol. 7, p. 12323, Aug. 2016.

[80] P. Colomban, "The Use of Metal Nanoparticles to Produce Yellow, Red and Iridescent Colour, from Bronze Age to Present Times in Lustre Pottery and Glass: Solid State Chemistry, Spectroscopy and Nanostructure," *J. Nano Res.*, vol. 8, pp. 109–132, Sep. 2009.

[81] P. Colomban and C. Truong, "Non-destructive Raman study of the glazing technique in lustre potteries and faience(9–14th centuries): silver ions, nanoclusters, microstructure and

processing," *J. Raman Spectrosc.*, vol. 35, no. 3, pp. 195–207, Mar. 2004.

[82] L. B. Hunt, "Gold based glass and enamel colours," *Endeavour*, vol. 5, no. 2, pp. 61–67, Jan. 1981.

[83] X. Yin, Z. Ye, J. Rho, Y. Wang, and X. Zhang, "Photonic Spin Hall Effect at Metasurfaces," *Science*, vol. 339, no. 6126, pp. 1405–1407, Mar. 2013.

[84] M. W. Knight *et al.*, "Aluminum Plasmonic Nanoantennas," *Nano Lett.*, vol. 12, no. 11, pp. 6000–6004, Nov. 2012.

[85] T. Xu, C. Du, C. Wang, and X. Luo, "Subwavelength imaging by metallic slab lens with nanoslits," *Appl. Phys. Lett.*, vol. 91, no. 20, p. 201501, Nov. 2007.

[86] W. Srituravanich, L. Pan, Y. Wang, C. Sun, D. B. Bogy, and X. Zhang, "Flying plasmonic lens in the near field for high-speed nanolithography," *Nat. Nanotechnol.*, vol. 3, no. 12, pp. 733–737, Dec. 2008.

[87] X. Ni, S. Ishii, A. V Kildishev, and V. M. Shalaev, "Ultra-thin, planar, Babinet-inverted plasmonic metalenses," *Light Sci. Appl.*, vol. 2, no. 4, p. e72, Apr. 2013.

[88] X. Chen *et al.*, "Dual-polarity plasmonic metalens for visible light," *Nat. Commun.*, vol. 3, p. 1198, Nov. 2012.

[89] F. Aieta *et al.*, "Aberration-Free Ultrathin Flat Lenses and Axicons at Telecom Wavelengths Based on Plasmonic Metasurfaces," *Nano Lett.*, vol. 12, no. 9, pp. 4932–4936, Sep. 2012.

[90] Z. Li, E. Palacios, S. Butun, and K. Aydin, "Visible-Frequency Metasurfaces for Broadband Anomalous Reflection and High-Efficiency Spectrum Splitting," *Nano Lett.*, vol. 15, no. 3, pp. 1615–1621, Mar. 2015.

[91] X. Ni, A. V. Kildishev, and V. M. Shalaev, "Metasurface holograms for visible light," *Nat. Commun.*, vol. 4, p. 2807, Nov. 2013.

[92] F. Zhou, Y. Liu, and W. Cai, "Plasmonic holographic imaging with V-shaped nanoantenna array," *Opt. Express*, vol. 21, no. 4, p. 4348, Feb. 2013.

[93] Y. Montelongo, J. O. Tenorio-Pearl, W. I. Milne, and T. D. Wilkinson, "Polarization Switchable Diffraction Based on Subwavelength Plasmonic Nanoantennas," *Nano Lett.*, vol.

14, no. 1, pp. 294–298, Jan. 2014.

[94] L. Huang *et al.*, “Three-dimensional optical holography using a plasmonic metasurface,” *Nat. Commun.*, vol. 4, no. May, p. 2808, Nov. 2013.

[95] G. Zheng, H. Mühlenbernd, M. Kenney, G. Li, T. Zentgraf, and S. Zhang, “Metasurface holograms reaching 80% efficiency,” *Nat. Nanotechnol.*, vol. 10, no. 4, pp. 308–312, Feb. 2015.

[96] D. Wen *et al.*, “Helicity multiplexed broadband metasurface holograms,” *Nat. Commun.*, vol. 6, p. 8241, Sep. 2015.

[97] W. T. Chen *et al.*, “High-Efficiency Broadband Meta-Hologram with Polarization-Controlled Dual Images,” *Nano Lett.*, vol. 14, no. 1, pp. 225–230, Jan. 2014.

[98] W. Ye *et al.*, “Spin and wavelength multiplexed nonlinear metasurface holography,” *Nat. Commun.*, vol. 7, no. 1, p. 11930, Dec. 2016.

[99] Y. Montelongo, J. O. Tenorio-Pearl, C. Williams, S. Zhang, W. I. Milne, and T. D. Wilkinson, “Plasmonic nanoparticle scattering for color holograms,” *Proc. Natl. Acad. Sci.*, vol. 111, no. 35, pp. 12679–12683, Sep. 2014.

[100] Y.-W. W. Huang *et al.*, “Aluminum Plasmonic Multicolor Meta-Hologram,” *Nano Lett.*, vol. 15, no. 5, pp. 3122–3127, May 2015.

[101] X. Li *et al.*, “Multicolor 3D meta-holography by broadband plasmonic modulation,” *Sci. Adv.*, vol. 2, no. 11, pp. e1601102–e1601102, Nov. 2016.

[102] Y. Zhao and A. Alù, “Manipulating light polarization with ultrathin plasmonic metasurfaces,” *Phys. Rev. B*, vol. 84, no. 20, p. 205428, Nov. 2011.

[103] Z. Bomzon, G. Biener, V. Kleiner, and E. Hasman, “Space-variant Pancharatnam–Berry phase optical elements with computer-generated subwavelength gratings,” *Opt. Lett.*, vol. 27, no. 13, p. 1141, Jul. 2002.

[104] N. Yu, F. Aieta, P. Genevet, M. A. Kats, Z. Gaburro, and F. Capasso, “A Broadband, Background-Free Quarter-Wave Plate Based on Plasmonic Metasurfaces,” *Nano Lett.*, vol. 12, no. 12, pp. 6328–6333, Dec. 2012.

[105] E. Karimi, S. A. Schulz, I. De Leon, H. Qassim, J. Upham, and R. W. Boyd, "Generating optical orbital angular momentum at visible wavelengths using a plasmonic metasurface," *Light Sci. Appl.*, vol. 3, no. 5, p. e167, May 2014.

[106] F. Ding, Z. Wang, S. He, V. M. Shalaev, and A. V. Kildishev, "Broadband High-Efficiency Half-Wave Plate: A Supercell-Based Plasmonic Metasurface Approach," *ACS Nano*, vol. 9, no. 4, pp. 4111–4119, Apr. 2015.

[107] A. Pors and S. I. Bozhevolnyi, "Efficient and broadband quarter-wave plates by gap-plasmon resonators," *Opt. Express*, vol. 21, no. 3, p. 2942, Feb. 2013.

[108] F. Yue, D. Wen, J. Xin, B. D. Gerardot, J. Li, and X. Chen, "Vector Vortex Beam Generation with a Single Plasmonic Metasurface," *ACS Photonics*, vol. 3, no. 9, pp. 1558–1563, Sep. 2016.

[109] W. Wang *et al.*, "Ultra-thin optical vortex phase plate based on the metasurface and the angular momentum transformation," *J. Opt.*, vol. 17, no. 4, p. 045102, Apr. 2015.

[110] P. Genevet *et al.*, "Ultra-thin plasmonic optical vortex plate based on phase discontinuities," *Appl. Phys. Lett.*, vol. 100, no. 1, p. 013101, Jan. 2012.

[111] X. Ni, Z. J. Wong, M. Mrejen, Y. Wang, and X. Zhang, "An ultrathin invisibility skin cloak for visible light," *Science*, vol. 349, no. 6254, pp. 1310–1314, Sep. 2015.

[112] J. Kim *et al.*, "Controlling the Polarization State of Light with Plasmonic Metal Oxide Metasurface," *ACS Nano*, vol. 10, no. 10, pp. 9326–9333, Oct. 2016.

[113] S. Ishii, A. V Kildishev, V. M. Shalaev, K.-P. Chen, and V. P. Drachev, "Metal nanoslit lenses with polarization-selective design: erratum.," *Opt. Lett.*, vol. 36, no. 7, p. 1244, 2011.

[114] Y. Yang, W. Wang, P. Moitra, I. I. Kravchenko, D. P. Briggs, and J. Valentine, "Dielectric meta-reflectarray for broadband linear polarization conversion and optical vortex generation," *Nano Lett.*, vol. 14, no. 3, pp. 1394–1399, 2014.

[115] A. Shaltout, J. Liu, A. Kildishev, and V. Shalaev, "Photonic spin Hall effect in gap–plasmon metasurfaces for on-chip chiroptical spectroscopy," *Optica*, vol. 2, no. 10, p. 860, Oct. 2015.

[116] V. S. Asadchy, A. Wickberg, A. Díaz-Rubio, and M. Wegener, "Eliminating Scattering

Loss in Anomalously Reflecting Optical Metasurfaces," *ACS Photonics*, vol. 4, no. 5, pp. 1264–1270, May 2017.

[117] S. Yokogawa, S. P. Burgos, and H. A. Atwater, "Plasmonic Color Filters for CMOS Image Sensor Applications," *Nano Lett.*, vol. 12, no. 8, pp. 4349–4354, Aug. 2012.

[118] J. S. Clausen *et al.*, "Plasmonic Metasurfaces for Coloration of Plastic Consumer Products," *Nano Lett.*, vol. 14, no. 8, pp. 4499–4504, Aug. 2014.

[119] A. S. Roberts, A. Pors, O. Albrektsen, and S. I. Bozhevolnyi, "Subwavelength Plasmonic Color Printing Protected for Ambient Use," *Nano Lett.*, vol. 14, no. 2, pp. 783–787, Feb. 2014.

[120] S. Kruk *et al.*, "Enhanced Magnetic Second-Harmonic Generation from Resonant Metasurfaces," *ACS Photonics*, vol. 2, no. 8, pp. 1007–1012, Aug. 2015.

[121] E. A. Mamonov, I. A. Kolmychek, A. I. Maydykovsky, and T. V. Murzina, "Second harmonic generation in planar chiral nanostructures," *Bull. Russ. Acad. Sci. Phys.*, vol. 77, no. 1, pp. 66–68, Jan. 2013.

[122] R. Chandrasekar *et al.*, "Second harmonic generation with plasmonic metasurfaces: direct comparison of electric and magnetic resonances," *Opt. Mater. Express*, vol. 5, no. 11, p. 2682, Nov. 2015.

[123] J. S. Gomez-Diaz, J. Lee, M. Tymchenko, M. A. Belkin, A. Alù, and A. Alu, "Giant nonlinear processes in plasmonic metasurfaces," in *2015 IEEE International Symposium on Antennas and Propagation & USNC/URSI National Radio Science Meeting*, 2015, vol. 2015-Octob, pp. 1084–1085.

[124] M. Tymchenko, J. S. Gomez-Diaz, J. Lee, N. Nookala, M. A. Belkin, and A. Alù, "Gradient Nonlinear Pancharatnam-Berry Metasurfaces," *Phys. Rev. Lett.*, vol. 115, no. 20, p. 207403, Nov. 2015.

[125] E. Panchenko, J. J. Cadusch, T. D. James, and A. Roberts, "Plasmonic Metasurface-Enabled Differential Photodetectors for Broadband Optical Polarization Characterization," *ACS Photonics*, vol. 3, no. 10, pp. 1833–1839, Oct. 2016.

[126] I. S. Maksymov, “Magneto-plasmonic nanoantennas: Basics and applications,” *Rev. Phys.*, vol. 1, pp. 36–51, Nov. 2016.

[127] T. S. Luk *et al.*, “Directional perfect absorption using deep subwavelength low-permittivity films,” *Phys. Rev. B - Condens. Matter Mater. Phys.*, vol. 90, no. 8, pp. 1–10, 2014.

[128] F. Ding, J. Dai, Y. Chen, J. Zhu, Y. Jin, and S. I. Bozhevolnyi, “Broadband near-infrared metamaterial absorbers utilizing highly lossy metals,” *Sci. Rep.*, vol. 6, no. 1, p. 39445, Dec. 2016.

[129] K. Aydin, V. E. Ferry, R. M. Briggs, and H. A. Atwater, “Broadband polarization-independent resonant light absorption using ultrathin plasmonic super absorbers,” *Nat. Commun.*, vol. 2, p. 517, Nov. 2011.

[130] Z. H. Jiang, S. Yun, F. Toor, D. H. Werner, and T. S. Mayer, “Conformal Dual-Band Near-Perfectly Absorbing Mid-Infrared Metamaterial Coating,” *ACS Nano*, vol. 5, no. 6, pp. 4641–4647, Jun. 2011.

[131] C. Argyropoulos, K. Q. Le, N. Mattiucci, G. D’Aguanno, and A. Alù, “Broadband absorbers and selective emitters based on plasmonic Brewster metasurfaces,” *Phys. Rev. B*, vol. 87, no. 20, p. 205112, May 2013.

[132] G. M. Akselrod *et al.*, “Large-Area Metasurface Perfect Absorbers from Visible to Near-Infrared,” *Adv. Mater.*, vol. 27, no. 48, pp. 8028–8034, Dec. 2015.

[133] C. Ng *et al.*, “Hot Carrier Extraction with Plasmonic Broadband Absorbers,” *ACS Nano*, vol. 10, no. 4, pp. 4704–4711, Apr. 2016.

[134] U. Guler, A. Boltasseva, and V. M. Shalaev, “Refractory Plasmonics,” *Science*, vol. 344, no. 6181, pp. 263–264, Apr. 2014.

[135] J. A. Dionne *et al.*, “Localized fields, global impact: Industrial applications of resonant plasmonic materials,” *MRS Bull.*, vol. 40, no. 12, pp. 1138–1145, Dec. 2015.

[136] G. Albrecht, S. Kaiser, H. Giessen, and M. Hentschel, “Refractory Plasmonics without Refractory Materials,” *Nano Lett.*, vol. 17, no. 10, pp. 6402–6408, Oct. 2017.

[137] G. Albrecht, M. Ubl, S. Kaiser, H. Giessen, and M. Hentschel, “Comprehensive Study of

Plasmonic Materials in the Visible and Near-Infrared: Linear, Refractory, and Nonlinear Optical Properties," *ACS Photonics*, p. acsphotonics.7b01346, Jan. 2018.

[138] P. R. West, S. Ishii, G. V. Naik, N. K. Emani, V. M. Shalaev, and A. Boltasseva, "Searching for better plasmonic materials," *Laser Photonics Rev.*, vol. 4, no. 6, pp. 795–808, Nov. 2010.

[139] P. Genevet, F. Capasso, F. Aieta, M. Khorasaninejad, and R. Devlin, "Recent advances in planar optics: from plasmonic to dielectric metasurfaces," *Optica*, vol. 4, no. 1, p. 139, Jan. 2017.

[140] S. Jahani and Z. Jacob, "All-dielectric metamaterials," *Nat. Nanotechnol.*, vol. 11, no. 1, pp. 23–36, Jan. 2016.

[141] A. I. Kuznetsov, A. E. Miroshnichenko, M. L. Brongersma, Y. S. Kivshar, and B. Luk'yanchuk, "Optically resonant dielectric nanostructures," *Science*, vol. 354, no. 6314, p. aag2472, Nov. 2016.

[142] S. Campione *et al.*, "Broken Symmetry Dielectric Resonators for High Quality Factor Fano Metasurfaces," *ACS Photonics*, vol. 3, no. 12, pp. 2362–2367, Dec. 2016.

[143] Y. Yang, I. I. Kravchenko, D. P. Briggs, and J. Valentine, "All-dielectric metasurface analogue of electromagnetically induced transparency," *Nat. Commun.*, vol. 5, p. 5753, Dec. 2014.

[144] C. W. Hsu, B. Zhen, A. D. Stone, J. D. Joannopoulos, and M. Soljačić, "Bound states in the continuum," *Nat. Rev. Mater.*, vol. 1, no. 9, p. 16048, Jul. 2016.

[145] S. I. Azzam, V. M. Shalaev, A. Boltasseva, and A. V. Kildishev, "Formation of Bound States in the Continuum in Hybrid Plasmonic-Photonic Systems," *Phys. Rev. Lett.*, vol. 121, no. 25, p. 253901, Dec. 2018.

[146] P. Moitra, B. A. Slovick, Z. Gang Yu, S. Krishnamurthy, and J. Valentine, "Experimental demonstration of a broadband all-dielectric metamaterial perfect reflector," *Appl. Phys. Lett.*, vol. 104, no. 17, p. 171102, Apr. 2014.

[147] P. Moitra *et al.*, "Large-Scale All-Dielectric Metamaterial Perfect Reflectors," *ACS Photonics*, vol. 2, no. 6, pp. 692–698, Jun. 2015.

[148] M. Kerker, D.-S. Wang, and C. L. Giles, "Electromagnetic scattering by magnetic spheres," *J. Opt. Soc. Am.*, vol. 73, no. 6, p. 765, Jun. 1983.

[149] M. R. Shcherbakov *et al.*, "Enhanced Third-Harmonic Generation in Silicon Nanoparticles Driven by Magnetic Response," *Nano Lett.*, vol. 14, no. 11, pp. 6488–6492, Nov. 2014.

[150] Y. Yang *et al.*, "Nonlinear Fano-Resonant Dielectric Metasurfaces," *Nano Lett.*, vol. 15, no. 11, pp. 7388–7393, Nov. 2015.

[151] B. J. M. Hausmann, I. Bulu, V. Venkataraman, P. Deotare, and M. Lončar, "Diamond nonlinear photonics," *Nat. Photonics*, vol. 8, no. 5, pp. 369–374, Apr. 2014.

[152] A. Sipahigil *et al.*, "An integrated diamond nanophotonics platform for quantum-optical networks," *Science*, vol. 354, no. 6314, pp. 847–850, Nov. 2016.

[153] J. T. Choy *et al.*, "Enhanced single-photon emission from a diamond–silver aperture," *Nat. Photonics*, vol. 5, no. 12, pp. 738–743, Oct. 2011.

[154] T. M. Babinec *et al.*, "A diamond nanowire single-photon source," *Nat. Nanotechnol.*, vol. 5, no. 3, pp. 195–199, Mar. 2010.

[155] L. Li *et al.*, "Coherent spin control of a nanocavity-enhanced qubit in diamond," *Nat. Commun.*, vol. 6, p. 6173, Jan. 2015.

[156] H. Clevenson, M. E. Trusheim, C. Teale, T. Schröder, D. Braje, and D. Englund, "Broadband magnetometry and temperature sensing with a light-trapping diamond waveguide," *Nat. Phys.*, vol. 11, no. 5, pp. 393–397, Apr. 2015.

[157] E. H. Chen, O. Gaathon, M. E. Trusheim, and D. Englund, "Wide-Field Multispectral Super-Resolution Imaging Using Spin-Dependent Fluorescence in Nanodiamonds," *Nano Lett.*, vol. 13, no. 5, pp. 2073–2077, May 2013.

[158] R. R. Grote *et al.*, "Imaging a Nitrogen-Vacancy Center with a Diamond Immersion Metalens," Nov. 2017.

[159] P. Lalanne, S. Astilean, P. Chavel, E. Cambril, and H. Launois, "Blazed binary subwavelength gratings with efficiencies larger than those of conventional échelette gratings," *Opt. Lett.*, vol. 23, no. 14, p. 1081, Jul. 1998.

[160] P. Lalanne, S. Astilean, P. Chavel, E. Cambril, and H. Launois, "Design and fabrication of blazed binary diffractive elements with sampling periods smaller than the structural cutoff," *J. Opt. Soc. Am. A*, vol. 16, no. 5, p. 1143, May 1999.

[161] P. Lalanne, "Waveguiding in blazed-binary diffractive elements," *J. Opt. Soc. Am. A*, vol. 16, no. 10, p. 2517, Oct. 1999.

[162] M. Decker *et al.*, "High-Efficiency Dielectric Huygens' Surfaces," *Adv. Opt. Mater.*, vol. 3, no. 6, pp. 813–820, Jun. 2015.

[163] Y. F. Yu, A. Y. Zhu, R. Paniagua-Domínguez, Y. H. Fu, B. Luk'yanchuk, and A. I. Kuznetsov, "High-transmission dielectric metasurface with 2π phase control at visible wavelengths," *Laser Photonics Rev.*, vol. 9, no. 4, pp. 412–418, 2015.

[164] M. I. Shalaev, J. Sun, A. Tsukernik, A. Pandey, K. Nikolskiy, and N. M. Litchinitser, "High-Efficiency All-Dielectric Metasurfaces for Ultracompact Beam Manipulation in Transmission Mode," *Nano Lett.*, vol. 15, no. 9, pp. 6261–6266, Sep. 2015.

[165] K. E. Chong *et al.*, "Polarization-Independent Silicon Metadevices for Efficient Optical Wavefront Control," *Nano Lett.*, vol. 15, no. 8, pp. 5369–5374, 2015.

[166] K. E. Chong *et al.*, "Efficient Polarization-Insensitive Complex Wavefront Control Using Huygens' Metasurfaces Based on Dielectric Resonant Meta-atoms," *ACS Photonics*, vol. 3, no. 4, pp. 514–519, Apr. 2016.

[167] M. Khorasaninejad *et al.*, "Polarization-Insensitive Metalenses at Visible Wavelengths," *Nano Lett.*, vol. 16, no. 11, pp. 7229–7234, Nov. 2016.

[168] D. Lin, P. Fan, E. Hasman, and M. L. Brongersma, "Dielectric gradient metasurface optical elements," *Science*, vol. 345, no. 6194, pp. 298–302, Jul. 2014.

[169] M. Khorasaninejad, A. Ambrosio, P. Kanhaiya, and F. Capasso, "Broadband and chiral binary dielectric meta-holograms," *Sci. Adv.*, vol. 2, no. 5, pp. e1501258–e1501258, May 2016.

[170] A. Niv, G. Biener, V. Kleiner, and E. Hasman, "Manipulation of the Pancharatnam phase in vectorial vortices," *Opt. Express*, vol. 14, no. 10, p. 4208, 2006.

[171] M. Khorasaninejad, W. T. Chen, J. Oh, and F. Capasso, “Super-Dispersive Off-Axis Meta-Lenses for Compact High Resolution Spectroscopy,” *Nano Lett.*, vol. 16, no. 6, pp. 3732–3737, Jun. 2016.

[172] Z. Bomzon, V. Kleiner, and E. Hasman, “Pancharatnam–Berry phase in space-variant polarization-state manipulations with subwavelength gratings,” *Opt. Lett.*, vol. 26, no. 18, p. 1424, Sep. 2001.

[173] Z. Huang, J. E. Carey, M. Liu, X. Guo, E. Mazur, and J. C. Campbell, “Microstructured silicon photodetector,” *Appl. Phys. Lett.*, vol. 89, no. 3, 2006.

[174] S. Assefa, F. Xia, and Y. A. Vlasov, “Reinventing germanium avalanche photodetector for nanophotonic on-chip optical interconnects,” *Nature*, vol. 464, no. 7285, pp. 80–84, 2010.

[175] J. B. D. Soole and H. Schumacher, “Ingaas Metal-Semiconductor-Metal Photodetectors for Long Wavelength Optical Communications,” *IEEE J. Quantum Electron.*, vol. 27, no. 3, pp. 737–752, 1991.

[176] E. J. H. Lee, K. Balasubramanian, R. T. Weitz, M. Burghard, and K. Kern, “Contact and edge effects in graphene devices.,” *Nat. Nanotechnol.*, vol. 3, no. 8, pp. 486–90, Aug. 2008.

[177] F. Xia *et al.*, “Photocurrent Imaging and Efficient Photon Detection in a Graphene Transistor,” *Nano Lett.*, vol. 9, no. 3, pp. 1039–1044, Mar. 2009.

[178] T. Mueller, F. Xia, M. Freitag, J. Tsang, and P. Avouris, “Role of contacts in graphene transistors: A scanning photocurrent study,” *Phys. Rev. B*, vol. 79, no. 24, p. 245430, Jun. 2009.

[179] F. Xia, T. Mueller, Y. Lin, A. Valdes-Garcia, and P. Avouris, “Ultrafast graphene photodetector,” *Nat. Nanotechnol.*, vol. 4, no. 12, pp. 839–843, 2009.

[180] T. Mueller, F. Xia, and P. Avouris, “Graphene photodetectors for high-speed optical communications,” *Nat. Photonics*, vol. 4, no. 5, pp. 297–301, 2010.

[181] X. Xu, N. M. Gabor, J. S. Alden, A. M. Van Der Zande, and P. L. McEuen, “Photo-thermoelectric effect at a graphene interface junction,” *Nano Lett.*, vol. 10, no. 2, pp. 562–566, 2010.

[182] J. C. W. Song, M. S. Rudner, C. M. Marcus, and L. S. Levitov, "Hot Carrier Transport and Photocurrent Response in Graphene," *Nano Lett.*, vol. 11, no. 11, pp. 4688–4692, Nov. 2011.

[183] N. M. Gabor *et al.*, "Hot carrier-assisted intrinsic photoresponse in graphene," *Science*, vol. 334, no. 6056, pp. 648–652, 2011.

[184] N. K. Emani *et al.*, "Plasmon resonance in multilayer graphene nanoribbons," *Laser Photon. Rev.*, vol. 9, no. 6, pp. 650–655, Nov. 2015.

[185] D. Wang *et al.*, "Spatial and Temporal Nanoscale Plasmonic Heating Quantified by Thermoreflectance," *Nano Lett.*, vol. 19, no. 6, pp. 3796–3803, Jun. 2019.

[186] K. F. Mak, M. Y. Sfeir, J. a Misewich, and T. F. Heinz, "The evolution of electronic structure in few-layer graphene revealed by optical spectroscopy," *Proc. Natl. Acad. Sci.*, vol. 107, no. 34, pp. 14999–15004, Aug. 2010.

[187] L. A. Falkovsky and A. A. Varlamov, "Space-time dispersion of graphene conductivity," *Eur. Phys. J. B*, vol. 56, no. 4, pp. 281–284, Apr. 2007.

[188] A. R. Wright, J. C. Cao, and C. Zhang, "Enhanced Optical Conductivity of Bilayer Graphene Nanoribbons in the Terahertz Regime," *Phys. Rev. Lett.*, vol. 103, no. 20, p. 207401, Nov. 2009.

[189] H. Yan *et al.*, "Tunable infrared plasmonic devices using graphene/insulator stacks," *Nat. Nanotechnol.*, vol. 7, no. 5, pp. 330–334, Apr. 2012.

[190] T. Chung, T. Shen, and H. Cao, "Synthetic graphene grown by chemical vapor deposition on copper foils," *Int. J. Mod. Phys. B*, vol. 27, no. 10, p. 1341002, 2013.

[191] Q. Yu *et al.*, "Control and characterization of individual grains and grain boundaries in graphene grown by chemical vapour deposition," *Nat. Mater.*, vol. 10, no. 6, pp. 443–449, 2011.

[192] H. Cao *et al.*, "Electronic transport in chemical vapor deposited graphene synthesized on Cu: Quantum Hall effect and weak localization," *Appl. Phys. Lett.*, vol. 96, no. 12, 2010.

[193] N. Petrone *et al.*, "Chemical Vapor Deposition-Derived Graphene with Electrical Performance of Exfoliated Graphene," *Nano Lett.*, vol. 12, no. 6, pp. 2751–2756, Jun. 2012.

[194] K. Kim *et al.*, "Raman spectroscopy study of rotated double-layer graphene: Misorientation-angle dependence of electronic structure," *Phys. Rev. Lett.*, vol. 108, no. 24, 2012.

[195] A. C. Ferrari and D. M. Basko, "Raman spectroscopy as a versatile tool for studying the properties of graphene," *Nat. Nanotechnol.*, vol. 8, no. 4, pp. 235–246, 2013.

[196] R. W. Havener, H. Zhuang, L. Brown, R. G. Hennig, and J. Park, "Angle-resolved raman imaging of interlayer rotations and interactions in twisted bilayer graphene," *Nano Lett.*, vol. 12, no. 6, pp. 3162–3167, 2012.

[197] X. Zhu *et al.*, "Plasmon-phonon coupling in large-area graphene dot and antidot arrays fabricated by nanosphere lithography," *Nano Lett.*, vol. 14, no. 5, pp. 2907–2913, 2014.

[198] P. Drude, "Ueber Oberflächenschichten. II. Theil," *Ann. Phys.*, vol. 272, no. 4, pp. 865–897, 1889.

[199] M. Y. Han, B. Özyilmaz, Y. Zhang, and P. Kim, "Energy band-gap engineering of graphene nanoribbons," *Phys. Rev. Lett.*, vol. 98, no. MAY, pp. 1–4, 2007.

[200] D. Rodrigo, A. Tittl, O. Limaj, F. J. García de Abajo, V. Pruneri, and H. Altug, "Double-layer graphene for enhanced tunable infrared plasmonics," *Light Sci. Appl.*, vol. 6, no. 6, p. e16277, Jun. 2017.

[201] R. R. Nair *et al.*, "Fine structure constant defines visual transparency of graphene.," *Science*, vol. 320, no. 5881, p. 1308, 2008.

[202] Z. Q. Li *et al.*, "Dirac charge dynamics in graphene by infrared spectroscopy," *Nat. Phys.*, vol. 4, no. 7, pp. 532–535, 2008.

[203] K. J. Tielrooij *et al.*, "Electrical control of optical emitter relaxation pathways enabled by graphene," *Nat. Phys.*, vol. 11, no. 3, pp. 281–287, 2015.

[204] G.-H. Lee *et al.*, "Flexible and Transparent MoS 2 Field-Effect Transistors on Hexagonal Boron Nitride-Graphene Heterostructures," *ACS Nano*, vol. 7, no. 9, pp. 7931–7936, Sep. 2013.

[205] C.-H. Lee *et al.*, "Atomically thin p–n junctions with van der Waals heterointerfaces," *Nat. Nanotechnol.*, vol. 9, no. 9, pp. 676–681, Sep. 2014.

[206] X. Gan *et al.*, "Chip-integrated ultrafast graphene photodetector with high responsivity," *Nat. Photonics*, vol. 7, no. 11, pp. 883–887, 2013.

[207] M. C. Lemme *et al.*, "Gate-Activated Photoresponse in a Graphene p–n Junction," *Nano Lett.*, vol. 11, no. 10, pp. 4134–4137, Oct. 2011.

[208] F. Ghahari, H.-Y. Xie, T. Taniguchi, K. Watanabe, M. S. Foster, and P. Kim, "Enhanced Thermoelectric Power in Graphene: Violation of the Mott Relation by Inelastic Scattering," *Phys. Rev. Lett.*, vol. 116, no. 13, p. 136802, Mar. 2016.

[209] M. Freitag, T. Low, F. N. Xia, and P. Avouris, "Photoconductivity of biased graphene," *Nat. Photonics*, vol. 7, no. 1, pp. 53–59, 2013.

[210] C.-H. Liu, Y.-C. Chang, T. B. Norris, and Z. Zhong, "Graphene photodetectors with ultra-broadband and high responsivity at room temperature.," *Nat. Nanotechnol.*, vol. 9, no. 4, pp. 273–8, Apr. 2014.

[211] G. Konstantatos *et al.*, "Hybrid graphene–quantum dot phototransistors with ultrahigh gain," *Nat. Nanotechnol.*, vol. 7, no. 6, pp. 363–368, 2012.

[212] Z. Fang *et al.*, "Plasmon-induced doping of graphene.," *ACS Nano*, vol. 6, no. 11, pp. 10222–8, 2012.

[213] D. Spirito *et al.*, "High performance bilayer-graphene Terahertz detectors," *Appl. Phys. Lett.*, vol. 104, no. 6, p. 061111, 2014.

[214] F. H. L. Koppens, T. Mueller, P. Avouris, A. C. Ferrari, M. S. Vitiello, and M. Polini, "Photodetectors based on graphene, other two-dimensional materials and hybrid systems," *Nat. Nanotechnol.*, vol. 9, no. 10, pp. 780–793, Oct. 2014.

[215] T. J. Echtermeyer *et al.*, "Photothermoelectric and Photoelectric Contributions to Light Detection in Metal − Graphene − Metal Photodetectors," *Nano Lett.*, vol. 14, no. 7, pp. 3733–3742, 2014.

[216] A. Brenneis *et al.*, "Ultrafast electronic readout of diamond nitrogen–vacancy centres coupled to graphene," *Nat. Nanotechnol.*, vol. 10, no. 2, pp. 135–139, Dec. 2014.

[217] K. J. Tielrooij *et al.*, "Generation of photovoltage in graphene on a femtosecond timescale

through efficient carrier heating,” *Nat. Nanotechnol.*, vol. 10, no. 5, pp. 437–443, Apr. 2015.

[218] K. J. Tielrooij *et al.*, “Hot-carrier photocurrent effects at graphene-metal interfaces.,” *J. Phys. Condens. Matter*, vol. 27, no. 16, p. 164207, 2015.

[219] R. J. Shiue *et al.*, “High-Responsivity Graphene-Boron Nitride Photodetector and Autocorrelator in a Silicon Photonic Integrated Circuit,” *Nano Lett.*, vol. 15, no. 11, pp. 7288–7293, 2015.

[220] V. M. Shalaev, *Nonlinear Optics of Random Media*, vol. 158. Berlin, Heidelberg: Springer Berlin Heidelberg, 2000.

[221] S. Gottheim, H. Zhang, A. O. Govorov, and N. J. Halas, “Fractal nanoparticle plasmonics: The cayley tree,” *ACS Nano*, vol. 9, no. 3, pp. 3284–3292, 2015.

[222] F. Afshinmanesh, A. G. Curto, K. M. Milaninia, N. F. Van Hulst, and M. L. Brongersma, “Transparent metallic fractal electrodes for semiconductor devices,” *Nano Lett.*, vol. 14, no. 9, pp. 5068–5074, 2014.

[223] Y. Lin and Z. Zhang, “Influence of trap location on the efficiency of trapping in dendrimers and regular hyperbranched polymers,” *J. Chem. Phys.*, vol. 138, no. 9, 2013.

[224] M. Bader, *Space-Filling Curves: An Introduction with Applications in Scientific Computing*, vol. 9. Berlin, Heidelberg: Springer Berlin Heidelberg, 2013.

[225] H. Sagan, *Space-Filling Curves*. New York, NY: Springer New York, 1994.

[226] A. Taflove and S. C. Hagness, *Computational Electrodynamics: The Finite-Difference Time-Domain Method, Third Edition*. Norwood, MA: Artech House, 2005.

[227] L. J. Prokopeva, J. D. Borneman, and A. V. Kildishev, “Optical dispersion models for time-domain modeling of metal-dielectric nanostructures,” in *IEEE Transactions on Magnetics*, 2011, vol. 47, no. 5, pp. 1150–1153.

[228] X. Ni, Z. Liu, and A. V. Kildishev, “PhotonicsDB: Optical Constants,” 2008. [Online]. Available: https://nanohub.org/resources/3692/?rev=68.

[229] B. Hecht, H. Bielefeldt, Y. Inouye, D. W. Pohl, and L. Novotny, “Facts and artifacts in near-field optical microscopy,” *J. Appl. Phys.*, vol. 81, no. 6, pp. 2492–2498, 1997.

[230] R. Bakker *et al.*, "Near-field excitation of nanoantenna resonance," *Opt. Express*, vol. 15, no. 21, pp. 13682–13688, 2007.

[231] M. W. Graham, S.-F. Shi, D. C. Ralph, J. Park, and P. L. McEuen, "Photocurrent measurements of supercollision cooling in graphene," *Nat. Phys.*, vol. 9, no. 2, pp. 103–108, 2013.

[232] M. Massicotte *et al.*, "Picosecond photoresponse in van der Waals heterostructures.," *Nat. Nanotechnol.*, vol. 11, pp. 42–46, 2016.

[233] S. Lei *et al.*, "An Atomically Layered InSe Avalanche Photodetector," *Nano Lett.*, vol. 15, no. 5, pp. 3048–3055, May 2015.

[234] W. Wang, A. Klots, D. Prasai, Y. Yang, K. I. Bolotin, and J. Valentine, "Hot Electron-Based Near-Infrared Photodetection Using Bilayer MoS 2," *Nano Lett.*, vol. 15, no. 11, pp. 7440–7444, 2015.

[235] M. Buscema, D. J. Groenendijk, S. I. Blanter, G. A. Steele, H. S. J. Van Der Zant, and A. Castellanos-Gomez, "Fast and broadband photoresponse of few-layer black phosphorus field-effect transistors," *Nano Lett.*, vol. 14, no. 6, pp. 3347–3352, 2014.

[236] M. W. Knight, H. Sobhani, P. Nordlander, and N. J. Halas, "Photodetection with Active Optical Antennas," *Science*, vol. 332, no. 6030, pp. 702–704, May 2011.

[237] M. Henstridge *et al.*, "Synchrotron radiation from an accelerating light pulse," *Science*, vol. 362, no. 6413, pp. 439–442, Oct. 2018.

[238] N. I. Zheludev and Y. S. Kivshar, "From metamaterials to metadevices," *Nat. Mater.*, vol. 11, no. 11, pp. 917–924, Nov. 2012.

[239] M. I. Stockman *et al.*, "Roadmap on plasmonics," *J. Opt.*, vol. 20, no. 4, p. 043001, Apr. 2018.

[240] G. Baffou, R. Quidant, and F. J. García de Abajo, "Nanoscale Control of Optical Heating in Complex Plasmonic Systems," *ACS Nano*, vol. 4, no. 2, pp. 709–716, Feb. 2010.

[241] S. Lal, S. E. Clare, and N. J. Halas, "Nanoshell-Enabled Photothermal Cancer Therapy: Impending Clinical Impact," *Acc. Chem. Res.*, vol. 41, no. 12, pp. 1842–1851, Dec. 2008.

[242] L. R. Hirsch *et al.*, "Nanoshell-mediated near-infrared thermal therapy of tumors under magnetic resonance guidance," *Proc. Natl. Acad. Sci.*, vol. 100, no. 23, pp. 13549–13554, Nov. 2003.

[243] V. E. Ferry, M. A. Verschuuren, H. B. T. Li, R. E. I. Schropp, H. A. Atwater, and A. Polman, "Improved red-response in thin film a-Si:H solar cells with soft-imprinted plasmonic back reflectors," *Appl. Phys. Lett.*, vol. 95, no. 18, p. 183503, Nov. 2009.

[244] R. A. Pala, J. White, E. Barnard, J. Liu, and M. L. Brongersma, "Design of Plasmonic Thin-Film Solar Cells with Broadband Absorption Enhancements," *Adv. Mater.*, vol. 21, no. 34, pp. 3504–3509, Sep. 2009.

[245] S. Linic, P. Christopher, and D. B. Ingram, "Plasmonic-metal nanostructures for efficient conversion of solar to chemical energy," *Nat. Mater.*, vol. 10, no. 12, pp. 911–921, Dec. 2011.

[246] L. Zhou *et al.*, "Quantifying hot carrier and thermal contributions in plasmonic photocatalysis," *Science*, vol. 362, no. 6410, pp. 69–72, Oct. 2018.

[247] B. J. Roxworthy and K. C. Toussaint, "Plasmonic nanotweezers: strong influence of adhesion layer and nanostructure orientation on trapping performance," *Opt. Express*, vol. 20, no. 9, p. 9591, Apr. 2012.

[248] M. L. Juan, M. Righini, and R. Quidant, "Plasmon nano-optical tweezers," *Nat. Photonics*, vol. 5, no. 6, pp. 349–356, Jun. 2011.

[249] W. Li and J. G. Valentine, "Harvesting the loss: surface plasmon-based hot electron photodetection," *Nanophotonics*, vol. 6, no. 1, pp. 177–191, Jan. 2017.

[250] U. Guler *et al.*, "Local Heating with Lithographically Fabricated Plasmonic Titanium Nitride Nanoparticles," *Nano Lett.*, vol. 13, no. 12, pp. 6078–6083, Dec. 2013.

[251] Z. J. Coppens, W. Li, D. G. Walker, and J. G. Valentine, "Probing and controlling photothermal heat generation in plasmonic nanostructures," *Nano Lett.*, vol. 13, no. 3, pp. 1023–1028, 2013.

[252] M. T. Carlson, A. Khan, and H. H. Richardson, "Local Temperature Determination of

Optically Excited Nanoparticles and Nanodots," *Nano Lett.*, vol. 11, no. 3, pp. 1061–1069, Mar. 2011.

[253] G. Kucsko *et al.*, "Nanometre-scale thermometry in a living cell," *Nature*, vol. 500, no. 7460, pp. 54–58, Aug. 2013.

[254] G. Baffou *et al.*, "Thermal Imaging of Nanostructures by Quantitative Optical Phase Analysis," *ACS Nano*, vol. 6, no. 3, pp. 2452–2458, Mar. 2012.

[255] J. Huang, W. Wang, C. J. Murphy, and D. G. Cahill, "Resonant secondary light emission from plasmonic Au nanostructures at high electron temperatures created by pulsed-laser excitation," *Proc. Natl. Acad. Sci.*, vol. 111, no. 3, pp. 906–911, Jan. 2014.

[256] X. Xie and D. G. Cahill, "Thermometry of plasmonic nanostructures by anti-Stokes electronic Raman scattering," *Appl. Phys. Lett.*, vol. 109, no. 18, p. 183104, Oct. 2016.

[257] K. Kim *et al.*, "Radiative heat transfer in the extreme near field," *Nature*, vol. 528, no. 7582, pp. 387–391, 2015.

[258] L. Cui *et al.*, "Study of radiative heat transfer in Ångström- and nanometre-sized gaps," *Nat. Commun.*, vol. 8, Feb. 2017.

[259] H. Harutyunyan *et al.*, "Anomalous ultrafast dynamics of hot plasmonic electrons in nanostructures with hot spots," *Nat. Nanotechnol.*, vol. 10, no. 9, pp. 770–774, Sep. 2015.

[260] M. E. Sykes *et al.*, "Enhanced generation and anisotropic Coulomb scattering of hot electrons in an ultra-broadband plasmonic nanopatch metasurface," *Nat. Commun.*, vol. 8, no. 1, p. 986, Dec. 2017.

[261] O. Lozan *et al.*, "Increased rise time of electron temperature during adiabatic plasmon focusing," *Nat. Commun.*, vol. 8, no. 1, p. 1656, Dec. 2017.

[262] A. Pors, O. Albrektsen, I. P. Radko, and S. I. Bozhevolnyi, "Gap plasmon-based metasurfaces for total control of reflected light," *Sci. Rep.*, vol. 3, no. 1, p. 2155, Dec. 2013.

[263] F. Ding, Y. Yang, R. A. Deshpande, and S. I. Bozhevolnyi, "A review of gap-surface plasmon metasurfaces: fundamentals and applications," *Nanophotonics*, vol. 7, no. 6, pp. 1129–1156, Jun. 2018.

[264] H.-H. Hsiao, C. H. Chu, and D. P. Tsai, “Fundamentals and Applications of Metasurfaces,” *Small Methods*, vol. 1, no. 4, p. 1600064, Apr. 2017.

[265] K. Maize, A. Ziabari, W. D. French, P. Lindorfer, B. OConnell, and A. Shakouri, “Thermoreflectance CCD Imaging of Self-Heating in Power MOSFET Arrays,” *IEEE Trans. Electron Devices*, vol. 61, no. 9, pp. 3047–3053, Sep. 2014.

[266] M. Farzaneh *et al.*, “CCD-based thermoreflectance microscopy: principles and applications,” *J. Phys. D. Appl. Phys.*, vol. 42, no. 14, p. 143001, Jul. 2009.

[267] V. Moreau *et al.*, “Transient thermoreflectance imaging of active photonic crystals,” *Appl. Phys. Lett.*, vol. 96, no. 9, p. 091103, Mar. 2010.

[268] K. Yazawa, J. A. Leon Gil, K. Maze, D. Kendig, and A. Shakouri, “Optical Pump-Probe Thermoreflectance Imaging for Anisotropic Heat Diffusion,” in *2018 17th IEEE Intersociety Conference on Thermal and Thermomechanical Phenomena in Electronic Systems (ITherm)*, 2018, pp. 59–66.

[269] W. M. Abbott *et al.*, “Solid state dewetting of thin plasmonic films under focused cw-laser irradiation,” *Acta Mater.*, vol. 145, pp. 210–219, Feb. 2018.

[270] K. Maize, E. Heller, D. Dorsey, and A. Shakouri, “Fast transient thermoreflectance CCD imaging of pulsed self heating in AlGaN/GaN power transistors,” in *2013 IEEE International Reliability Physics Symposium (IRPS)*, 2013, p. CD.2.1-CD.2.3.

[271] Y. R. Koh *et al.*, “Quasi-ballistic thermal transport in Al 0.1 Ga 0.9 N thin film semiconductors,” *Appl. Phys. Lett.*, vol. 109, no. 24, p. 243107, Dec. 2016.

[272] M. N. Luckyanova *et al.*, “Anisotropy of the Thermal Conductivity in GaAs/AlAs Superlattices,” *Nano Lett.*, vol. 13, no. 9, pp. 3973–3977, Sep. 2013.

[273] J. A. Tomko *et al.*, “Tunable thermal transport and reversible thermal conductivity switching in topologically networked bio-inspired materials,” *Nat. Nanotechnol.*, 2018.

[274] W. S. Capinski and H. J. Maris, “Improved apparatus for picosecond pump-and-probe optical measurements,” *Rev. Sci. Instrum.*, vol. 67, no. 8, pp. 2720–2726, Aug. 1996.

[275] R. M. Costescu, M. A. Wall, and D. G. Cahill, “Thermal conductance of epitaxial interfaces,”

Phys. Rev. B, vol. 67, no. 5, p. 054302, Feb. 2003.

[276] A. J. Schmidt, X. Chen, and G. Chen, "Pulse accumulation, radial heat conduction, and anisotropic thermal conductivity in pump-probe transient thermoreflectance," *Rev. Sci. Instrum.*, vol. 79, no. 11, p. 114902, Nov. 2008.

[277] D. G. Cahill, "Analysis of heat flow in layered structures for time-domain thermoreflectance," *Rev. Sci. Instrum.*, vol. 75, no. 12, pp. 5119–5122, Dec. 2004.

[278] Y. Hu, L. Zeng, A. J. Minnich, M. S. Dresselhaus, and G. Chen, "Spectral mapping of thermal conductivity through nanoscale ballistic transport," *Nat. Nanotechnol.*, vol. 10, no. 8, pp. 701–706, Aug. 2015.

[279] X. Chen *et al.*, "Ordered Au nanocrystals on a substrate formed by light-induced rapid annealing," *Nanoscale*, vol. 6, no. 3, pp. 1756–1762, 2014.

[280] A. H. Castro Neto, F. Guinea, N. M. R. Peres, K. S. Novoselov, and A. K. Geim, "The electronic properties of graphene," *Rev. Mod. Phys.*, vol. 81, no. 1, pp. 109–162, Jan. 2009.

[281] L. A. Falkovsky, "Optical properties of graphene," *J. Phys. Conf. Ser.*, vol. 129, no. 3, p. 012004, Oct. 2008.

[282] K. I. Bolotin *et al.*, "Ultrahigh electron mobility in suspended graphene," *Solid State Commun.*, vol. 146, no. 9–10, pp. 351–355, Jun. 2008.

[283] D. Sun *et al.*, "Ultrafast hot-carrier-dominated photocurrent in graphene," *Nat. Nanotechnol.*, vol. 7, no. 2, pp. 114–118, Feb. 2012.

[284] J. D. Cox and F. J. García de Abajo, "Single-Plasmon Thermo-Optical Switching in Graphene," *Nano Lett.*, vol. 19, no. 6, pp. 3743–3750, Jun. 2019.

[285] S. Castilla *et al.*, "Fast and Sensitive Terahertz Detection Using an Antenna-Integrated Graphene pn Junction," *Nano Lett.*, vol. 19, no. 5, pp. 2765–2773, May 2019.

[286] S. Goossens *et al.*, "Broadband image sensor array based on graphene–CMOS integration," *Nat. Photonics*, vol. 11, no. 6, pp. 366–371, May 2017.

[287] S. Schuler *et al.*, "Controlled Generation of a p–n Junction in a Waveguide Integrated Graphene Photodetector," *Nano Lett.*, vol. 16, no. 11, pp. 7107–7112, Nov. 2016.

[288] M. Henstridge *et al.*, “Accelerating light with metasurfaces,” *Optica*, vol. 5, no. 6, p. 678, Jun. 2018.

[289] U. Guler *et al.*, “Local Heating with Lithographically Fabricated Plasmonic Titanium Nitride Nanoparticles,” *Nano Lett.*, vol. 13, no. 12, pp. 6078–6083, Dec. 2013.

[290] J. C. Ndukaife, V. M. Shalaev, and A. Boltasseva, “Plasmonics--turning loss into gain,” *Science*, vol. 351, no. 6271, pp. 334–335, Jan. 2016.

[291] G. Giovannetti, P. Khomyakov, G. Brocks, V. Karpan, J. van den Brink, and P. Kelly, “Doping Graphene with Metal Contacts,” *Phys. Rev. Lett.*, vol. 101, no. 2, p. 026803, Jul. 2008.

[292] A. Brenneis *et al.*, “THz-circuits driven by photo-thermoelectric, gate-tunable graphene-junctions,” *Sci. Rep.*, vol. 6, no. 1, p. 35654, Dec. 2016.

[293] D. Reinsel, J. Gantz, and J. Rydning, *White Paper: The Digitization of the World - From Edge to Core*. Seagate, 2018.

[294] *White Paper: Optical Disc Data Archiving*. Osaka, Japan: Panasonic Corporation Connected Solutions Company, Storage Business Development Center, 2017.

[295] R. E. Fontana and G. M. Decad, “Moore’s law realities for recording systems and memory storage components: HDD, tape, NAND, and optical,” *AIP Adv.*, vol. 8, no. 5, p. 056506, May 2018.

[296] *White Paper: Archival Disc Technology*. Sony & Panasonic, 2018.

[297] W. T. Chen *et al.*, “Manipulation of multidimensional plasmonic spectra for information storage,” *Appl. Phys. Lett.*, vol. 98, no. 17, p. 171106, Apr. 2011.

[298] M. Mansuripur *et al.*, “Plasmonic nano-structures for optical data storage,” *Opt. Express*, vol. 17, no. 16, p. 14001, Aug. 2009.

[299] J. Li, S. Kamin, G. Zheng, F. Neubrech, S. Zhang, and N. Liu, “Addressable metasurfaces for dynamic holography and optical information encryption,” *Sci. Adv.*, vol. 4, no. 6, p. eaar6768, Jun. 2018.

[300] M. Gu, X. Li, and Y. Cao, “Optical storage arrays: a perspective for future big data storage,”

Light Sci. Appl., vol. 3, no. 5, pp. e177–e177, May 2014.

[301] S. Wu *et al.*, "Enhanced Rotation of the Polarization of a Light Beam Transmitted through a Silver Film with an Array of Perforated S-Shaped Holes," *Phys. Rev. Lett.*, vol. 110, no. 20, p. 207401, May 2013.

[302] L. Duempelmann, A. Luu-Dinh, B. Gallinet, and L. Novotny, "Four-Fold Color Filter Based on Plasmonic Phase Retarder," *ACS Photonics*, vol. 3, no. 2, pp. 190–196, Feb. 2016.

[303] T. Ellenbogen, K. Seo, and K. B. Crozier, "Chromatic Plasmonic Polarizers for Active Visible Color Filtering and Polarimetry," *Nano Lett.*, vol. 12, no. 2, pp. 1026–1031, Feb. 2012.

[304] Z. Li, A. W. Clark, and J. M. Cooper, "Dual Color Plasmonic Pixels Create a Polarization Controlled Nano Color Palette," *ACS Nano*, vol. 10, no. 1, pp. 492–498, Jan. 2016.

[305] E. Heydari *et al.*, "Plasmonic Color Filters as Dual-State Nanopixels for High-Density Microimage Encoding," *Adv. Funct. Mater.*, vol. 27, no. 35, p. 1701866, Sep. 2017.

[306] X. Zang *et al.*, "Polarization Encoded Color Image Embedded in a Dielectric Metasurface," *Adv. Mater.*, vol. 30, no. 21, p. 1707499, May 2018.

[307] M. Miyata, H. Hatada, and J. Takahara, "Full-Color Subwavelength Printing with Gap-Plasmonic Optical Antennas," *Nano Lett.*, vol. 16, no. 5, pp. 3166–3172, May 2016.

[308] T. D. James, P. Mulvaney, and A. Roberts, "The Plasmonic Pixel: Large Area, Wide Gamut Color Reproduction Using Aluminum Nanostructures," *Nano Lett.*, vol. 16, no. 6, pp. 3817–3823, Jun. 2016.

[309] M. Song, Z. A. Kudyshev, H. Yu, A. Boltasseva, V. M. Shalaev, and A. V. Kildishev, "Achieving full-color generation with polarization-tunable perfect light absorption," *Opt. Mater. Express*, vol. 9, no. 2, p. 779, Feb. 2019.

[310] X. Luo, D. Tsai, M. Gu, and M. Hong, "Subwavelength interference of light on structured surfaces," *Adv. Opt. Photonics*, vol. 10, no. 4, p. 757, Dec. 2018.

[311] X. Luo, D. Tsai, M. Gu, and M. Hong, "Extraordinary optical fields in nanostructures: from sub-diffraction-limited optics to sensing and energy conversion," *Chem. Soc. Rev.*, vol. 48,

no. 8, pp. 2458–2494, 2019.

[312] M. Song *et al.*, "Color display and encryption with a plasmonic polarizing metamirror," *Nanophotonics*, vol. 7, no. 1, pp. 323–331, Jan. 2018.

[313] X. M. Goh, R. J. H. Ng, S. Wang, S. J. Tan, and J. K. W. Yang, "Comparative Study of Plasmonic Colors from All-Metal Structures of Posts and Pits," *ACS Photonics*, vol. 3, no. 6, pp. 1000–1009, Jun. 2016.

[314] L. J. Guo, "Nanoimprint Lithography: Methods and Material Requirements," *Adv. Mater.*, vol. 19, no. 4, pp. 495–513, Feb. 2007.

[315] T. Li *et al.*, "Manipulating optical rotation in extraordinary transmission by hybrid plasmonic excitations," *Appl. Phys. Lett.*, vol. 93, no. 2, p. 021110, Jul. 2008.

[316] X. Zhu, C. Vannahme, E. Højlund-Nielsen, N. A. Mortensen, and A. Kristensen, "Plasmonic colour laser printing," *Nat. Nanotechnol.*, vol. 11, no. 4, pp. 325–329, Apr. 2016.

[317] Y. Chen *et al.*, "Dynamic Color Displays Using Stepwise Cavity Resonators," *Nano Lett.*, vol. 17, no. 9, pp. 5555–5560, Sep. 2017.

[318] S. Sun *et al.*, "All-Dielectric Full-Color Printing with TiO2 Metasurfaces," *ACS Nano*, vol. 11, no. 5, pp. 4445–4452, May 2017.

[319] J. Proust, F. Bedu, B. Gallas, I. Ozerov, and N. Bonod, "All-Dielectric Colored Metasurfaces with Silicon Mie Resonators," *ACS Nano*, vol. 10, no. 8, pp. 7761–7767, Aug. 2016.

[320] H. Kim *et al.*, "Structural colour printing using a magnetically tunable and lithographically fixable photonic crystal," *Nat. Photonics*, vol. 3, p. 534, Aug. 2009.

[321] Y. Horie *et al.*, "Visible Wavelength Color Filters Using Dielectric Subwavelength Gratings for Backside-Illuminated CMOS Image Sensor Technologies," *Nano Lett.*, vol. 17, no. 5, pp. 3159–3164, May 2017.

[322] D. Franklin, R. Frank, S.-T. Wu, and D. Chanda, "Actively addressed single pixel full-colour plasmonic display," *Nat. Commun.*, vol. 8, p. 15209, May 2017.

[323] K. Xiong *et al.*, "Plasmonic Metasurfaces with Conjugated Polymers for Flexible Electronic

Paper in Color," *Adv. Mater.*, vol. 28, no. 45, pp. 9956–9960, Dec. 2016.

[324] *White Paper Blu-ray Disc ™ Format*, 9th ed. Blu-ray Disc ™, 2015.

[325] A. B. Taylor, P. Michaux, A. S. M. Mohsin, and J. W. M. Chon, "Electron-beam lithography of plasmonic nanorod arrays for multilayered optical storage," *Opt. Express*, vol. 22, no. 11, p. 13234, Jun. 2014.

[326] P. Zijlstra, J. W. M. Chon, and M. Gu, "Supplementary: Five-dimensional optical recording mediated by surface plasmons in gold nanorods," *Nature*, vol. 459, no. 7245, pp. 410–413, May 2009.

[327] K. Kumar, H. Duan, R. S. Hegde, S. C. W. Koh, J. N. Wei, and J. K. W. Yang, "Printing colour at the optical diffraction limit," *Nat. Nanotechnol.*, vol. 7, no. 9, pp. 557–561, Sep. 2012.

[328] X. M. Goh *et al.*, "Three-dimensional plasmonic stereoscopic prints in full colour," *Nat. Commun.*, vol. 5, p. 5361, Nov. 2014.

VITA

Di Wang received his bachelor's degree from Chongqing University in China in 2011. He got his Master of Science degree from Columbia University in 2012, from the group of Prof. Chee Wei Wong. He is currently a PhD student in the groups of Prof. Vladimir M. Shalaev, Prof. Alexandra Boltasseva, and Prof. Alexander V. Kildishev, in the School of Electrical and Computer Engineering, Purdue University. His research mainly focuses on metasurfaces and graphene photodetectors. The research topics include developing graphene plasmonic resonators, graphene photodetectors with plasmonic enhancements, thermoplasmonic systems, metasurfaces for light propagation control, and advanced optical data storage with plasmonic colors.

PUBLICATIONS

1. Di Wang, Andres E. Llacsahuanga Allcca, Ting-Fung Chung, Alexander V. Kildishev, Yong P. Chen, Alexandra Boltasseva, Vladimir M. Shalaev, "Enhancing graphene photocurrent using surface plasmons and p-n junction", to be submitted
2. Maowen Song*, Di Wang*, Zhaxylyk A. Kudyshev, Yi Xuan, Zhuoxian Wang, Honglin Yu, Alexandra Boltasseva, Vladimir M. Shalaev, Alexander V. Kildishev, "Enabling optical steganography, data storage, and encryption with plasmonic colours", under review by *Nature Communications* (* Equal contribution)
3. Maowen Song, Di Wang, Samuel Peana, Sajid Choudhury, Piotr Nyga, Zhaxylyk A. Kudyshev, Honglin Yu, Alexandra Boltasseva, Vladimir M. Shalaev, Alexander V. Kildishev, "Colors with Plasmonic Nanostructures: A Full-Spectrum Review", forthcoming in *Applied Physics Reviews*
4. Huan Jiang, Sajid Choudhury, Zhaxylyk A. Kudyshev, Di Wang, Ludmila J. Prokopeva, Peng Xiao, Yongyuan Jiang, Alexander V. Kildishev, "Enhancing sensitivity to ambient refractive index with tunable few-layer graphene/hBN nanoribbons", *Photonics Research*, 7 (7), 815-822 (2019)
5. Huan Jiang, Harsha Reddy, Deesha Shah, Zhaxylyk A. Kudyshev, Sajid Choudhury, Di Wang, Yongyuan Jiang, Alexander V. Kildishev, "Modulating Phase by Metasurfaces with Gated Ultra-thin TiN Films", *Nanoscale*, 11, 11167-11172 (2019)
6. Di Wang, Yee Rui Koh, Zhaxylyk A. Kudyshev, Kerry Maize, Alexander V. Kildishev, Alexandra Boltasseva, Vladimir M. Shalaev, Ali Shakouri, "Spatial and Temporal Nanoscale Plasmonic Heating Quantified by Thermoreflectance", *Nano Letters*, 19 (6), 3796-3803 (2019)
7. Meredith Henstridge, Carl Pfeiffer, Di Wang, Alexandra Boltasseva, Vladimir M. Shalaev, Anthony Grbic, Roberto Merlin, "Synchrotron radiation from an accelerating light pulse", *Science*, 362 (6413), 439-442 (2018)
8. Sajid M. Choudhury, Di Wang, Krishnakali Chaudhuri, Clayton DeVault, Alexander V. Kildishev, Alexandra Boltasseva, Vladimir M. Shalaev, *Nanophotonics*, 7 (6), 959-987 (2018)

9. Meredith Henstridge, Carl Pfeiffer, Di Wang, Alexandra Boltasseva, Vladimir M. Shalaev, Anthony Grbic, Roberto Merlin, "Accelerating light with metasurfaces", *Optica*, 5 (6), 678-681 (2018)
10. Jieran Fang*, Di Wang*, Clayton T. DeVault, Ting-Fung Chung, Yong P. Chen, Alexandra Boltasseva, Vladimir M. Shalaev, Alexander V. Kildishev, "Enhanced graphene photodetector with fractal metasurface", *Nano Letters*, 17 (1), 57-62 (2017). (* Equal contribution)
11. Naresh Kumar Emani, Di Wang, Ting-Fung Chung, Ludmila J. Prokopeva, Alexander V. Kildishev, Vladimir M. Shalaev, Yong P Chen, Alexandra Boltasseva, "Plasmon resonance in multilayer graphene nanoribbons", *Laser & Photonics Reviews*, 9 (6), 650-655 (2015).
12. Xingsheng Luan, Yongjun Huang, Ying Li, James F. McMillan, Jiangjun Zheng, Shu-Wei Huang, Pin-Chun Hsieh, Tingyi Gu, Di Wang, Archita Hati, David A. Howe, Guangjun Wen, Mingbin Yu, Guoqiang Lo, Dim-Lee Kwong, Chee Wei Wong, "An integrated low phase noise radiation-pressure-driven optomechanical oscillator chipset", *Scientific Reports*, 4 (1), 6842 (2015).